FINAL REPORT

DEVELOPMENT OF ENHANCED SULFUR REJECTION PROCESSES

Principal Investigators:

R.-H. Yoon, G.H. Luttrell, G.T. Adel and P.E. Richardson

Center for Coal and Minerals Processing
Virginia Polytechnic Institute and State University
Blacksburg, Virginia 24061-0258

Contract No.: DE-AC22-92PC92246

Prepared for:

U.S. Department of Energy
Pittsburgh Energy Technology Center
P.O. Box 10940
Pittsburgh, PA 15236-0940

March, 1996

Contracting Officer's Representative: Richard Read

ABSTRACT

Research at Virginia Tech led to the development of two complementary concepts for improving the removal of inorganic sulfur from many eastern U.S. coals. These concepts are referred to as Electrochemically Enhanced Sulfur Rejection (EESR) and Polymer Enhanced Sulfur Rejection (PESR) processes. The EESR process uses electrochemical techniques to suppress the formation of hydrophobic oxidation products believed to be responsible for the floatability of coal pyrite. The PESR process uses polymeric reagents that react with pyrite and convert floatable middlings, i.e., composite particles composed of pyrite with coal inclusions, into hydrophilic particles. These new pyritic-sulfur rejection processes do not require significant modifications to existing coal preparation facilities, thereby enhancing their adoptability by the coal industry. It is believed that these processes can be used simultaneously to maximize the rejection of both well-liberated pyrite and composite coal-pyrite particles.

The project was initiated on October 1, 1992 and all technical work has been completed. This report is based on the research carried out under Tasks 2-7 described in the project proposal. These tasks include Characterization (Task 2), Electrochemical Studies (Task 3), In Situ Monitoring of Reagent Adsorption on Pyrite (Task 4), Bench Scale Testing of the EESR Process (Task 5), Bench Scale Testing of the PESR Process (Task 6), and Modeling and Simulation (Task 7).

The SEM characterization of several eastern coal samples has shown that for the minus 28 mesh size fraction, the Pittsburgh No. 8 coal sample contains the least amount of finely disseminated pyrite, the Upper Freeport sample the greatest, and the Illinois No. 6 sample is intermediate. At the minus 28 mesh size, the Illinois No. 6 sample contains the most free or nearly free pyrite and the Pittsburgh the least. When the size is reduced to minus 100 mesh, the free or nearly free pyrite in the Pittsburgh No. 8 sample increased to 70%, more than the Upper Freeport sample (60%) and the

Illinois No. 6 sample (57%). It is concluded that the minus 100 mesh Pittsburgh No. 8 sample has the greatest potential for demonstrating improvement of pyrite rejection by the EESR and PESR processes. Release analysis and image analysis "washability" data indicate that, in terms of pyrite rejection, the Illinois No. 6 coal should respond better to froth flotation than the Pittsburgh No. 8 coal. The Pittsburgh No. 8 sample, on the other hand, should respond better to gravity separation.

Extensive electrochemical studies have been performed using freshly fractured electrodes and rotating ring-disc electrodes, which provided a better understanding of oxidation and reduction processes on the surface of pyrite. The most significant finding from this work is the establishment that fresh surfaces of pyrite begin to oxidize at potentials that are several hundred millivolts more negative than reported in the literature. The incipient oxidation at these potentials is responsible for the collectorless flotation of pyrite observed in the absence of conventional sulfide collectors. Flotation tests conducted under controlled potentials indicate that the floatability of pyrite can be minimized under moderately reducing conditions, which prevent the mineral from oxidizing and/or remove preexisting oxidation products from the surface. It has been demonstrated that galvanic coupling between pyrite and reactive metals can be used to create a reducing environment sufficient to prevent pyrite oxidation. The application of this technique to flotation of Pittsburgh No. 8 coal showed that the EESR process can produce a significant improvement in pyritic sulfur rejection.

Several polymeric depressants containing hydroxylic and sulfide specific functional groups were tested with different samples of coal and pyrite. Results have shown that polymer S7261 can considerably depress pyrite with only marginal effects on the floatability of coal. It was speculated that the polymer adsorbed on pyrite and masked coal inclusions in middlings. The hydrophilic chains of the polymer thus reduced the floatability of middlings. FTIR and contact angle measurements showed that the potential of pyrite impacts the adsorption of polymer S7261. Higher adsorption density of the

polymer was observed at negative potentials than at positive ones. Promising results for improved sulfur rejection by the PESR process have been obtained with polymer S7261 for Pittsburgh No. 8 coal. Enhanced pyrite rejection in Illinois No. 6 coal flotation has also been observed when the polymer was used together with reactive metal powders.

TABLE OF CONTENTS

LIST OF FIGURES

LIST OF TABLES

INTRODUCTION

The primary objectives of the physical cleaning of coal for utility and steam markets traditionally are ash reduction and energy enrichment; however, increasing public concern with environmental pollution by acid rain are broadening the scope of coal beneficiation to include sulfur reduction. Studies by the U.S. Department of Energy (DOE) and others suggested that the physical cleaning of coal to remove pyritic sulfur can be more cost-effective than alternative post-combustion technologies such as flue gas scrubbing. Most recently, Schimmoller and Hucko (1994) have shown that removal of some pyritic sulfur often provides compliance coals that meet even Phase II emission standards mandated by the Clean Air Act Amendments (CAAA) of 1990.

Although physical cleaning methods appear to be more economically attractive, they suffer from low separation efficiency for removing pyrite from coal. Froth flotation is generally recognized as the most effective physical cleaning technique for coal fines that is commercially available. It is, however, very difficult to remove more than 50% of the pyrite from a minus 65 mesh coal, which is the typical size treated by flotation in coal preparation plants. Recent work at Virginia Tech's Center for Coal and Minerals Processing (CCMP) identified two major reasons why even the most advanced coal cleaning technologies (without fine grinding) fail to meet what is normally a standard flotation separation for most mineral systems, i.e., a 90-95% rejection of a gangue component (pyrite in coal) at a 90-95% recovery of a valuable component (combustible in coal). They are:

i) ***superficial oxidation*** of pyrite by an inadvertent corrosion-type process occurring during mining and processing, and

ii) ***incomplete liberation*** of pyrite from coal causing a large fraction of the pyrite to remain associated or locked with the coal as middlings.

The ***superficial oxidation*** produces a surface layer on pyrite composed of excess sulfur (or polysulfides), which is inherently hydrophobic. Thus, even fully-liberated pyrite, when superficially oxidized, can show a flotation response similar to that of coal, making the separation difficult. The ***incomplete liberation*** of pyrite from coal creates coal-pyrite composites which behave more like coal during flotation. It has been shown (Zitterbart et al., 1985) that many of the major U.S. coal seams will have to be pulverized to micron sizes to achieve sufficient liberation. Because of the strong hydrophobicity of coal, even small inclusions of coal in pyrite particles can render the composite particles floatable.

Superficial oxidation of pyrite presents a serious problem in removing pyritic sulfur from coal using any surface-based separation process. In the initial stages of oxidation, the sulfur on the surface becomes oxidized to polysulfide(s) which is inherently hydrophobic (Luttrell and Yoon, 1984; Chander and Bricero, 1987; Yoon et al., 1991; Zhu et al., 1991). Its hydrophobicity may not be as strong as that of coal, but in the presence of oily collectors and frothing agents that are commonly used in flotation, the hydrophobicity is dramatically enhanced (Yoon et al., 1991). Thus, it is necessary to prevent pyrite from oxidizing, which may be accomplished by adding various reducing agents. A problem with this approach is that the reagent consumption is generally high, as coal adsorbs most of the reagents.

The solution to the second problem may seem obvious: comminution of coal to a size at which the pyrite is fully liberated. This often requires coal to be micronized or submicronized. However, most conventional coal cleaning technologies now available are not effective for micronized samples. In addition, fine grinding is energy-intensive and micronized coal products entail tremendously high dewatering costs. It is, therefore, important to develop processes that can remove pyrite at a relatively

coarse size. The most cost-effective approach would be to control the wetting characteristics of the composite particles so that they do not report to the clean coal product.

Research at CCMP suggests two solutions to the above problems of pyrite recovery in coal flotation, i.e., ***Electrochemically-Enhanced Sulfur Rejection*** (EESR) and ***Polymer-Enhanced Sulfur Rejection*** (PESR) processes. The EESR concept is a novel technique that prevents the superficial oxidation of pyrite without using traditional reducing reagents. It uses a sacrificial anode reaction to prevent the oxidation of pyrite and, hence, minimizes the formation of hydrophobic oxidation products. This technique is flexible enough to be implemented during the process of grinding, conditioning or flotation. The PESR process is based on synthesizing polymeric organic reagents whose functional groups react with pyrite while the hydrophilic polymer chains are stretched over the coal inclusions, rendering the pyrite-coal composite particles nonfloatable. The EESR and PESR processes are complementary since the former suppresses the flotation of well-liberated pyrite, while the latter suppresses the flotation of middlings.

OBJECTIVE

The overall objective of this research is to develop these processes into technologies for improving the rejection of pyritic sulfur from eastern U.S. coals. If successful, a high degree of pyritic sulfur rejection could be achieved without having to micronize coal.

APPROACH

To achieve this objective, the two major problems, superficial oxidation and incomplete liberation of pyrite, were addressed by applying the two new approaches. One was to control the flotation behavior of liberated pyrite using the EESR technique, and the other was to control the floatability of the coal-pyrite composite particles using the PESR technique. The behavior of free and locked particles was monitored using an automated image analyzer.

EXPERIMENTAL

Release Analysis

Release analysis of coal samples was accomplished in two stages using a standard Denver laboratory flotation cell. The first stage was carried out to separate the non-floatable material from the floatable material by repeated cleaning and recleaning of the froth products to remove entrained matter. The second stage was used to classify the floatable material into different fractions based on the floatability. The first flotation in this stage was performed at an extremely low aeration rate and impeller speed to obtain the most floatable fraction. The aeration rate and impeller speed were incrementally increased in subsequent flotation tests to recover progressively less floatable material.

SEM-IPS Analysis

SEM-IPS (scanning electron microscope-image processing system) analysis of coal was carried out using a Cambridge Stereoscan 120 Scanning Electron Microscope coupled to a Kontron SEM-IPS Image Analysis System. The sample briquettes used for this analysis were sputter-coated with gold. The beam voltage was set at 30 KV. Different magnifications for different particle sizes were selected to make sure that about 40 particles could be identified in each field. A total of 1500-2000 particles were covered in a number of evenly distributed fields for each analysis.

Rotating Ring-Disc Electrodes (RRDE)

The rotating ring-disc electrode (RRDE) is schematically illustrated in Figure 1. It was constructed using core drilled discs of pyrite (0.7 cm diameter) and pure gold rings. The disc was separated from the ring by a small gap of nonconductive epoxy resin. The disc was contacted with a copper electrical lead. After mounting the ring-disc assembly, the surface was abraded and polished with successively finer grades of silicon carbide paper from 240 to 600 grit. The electrode was then cleaned with acetone and hydrochloric acid followed by a thorough rinse with distilled water. A Pine

RDE-4 double potentiostat was used to control the potential and a Pine rotating ring-disc assembly was used to rotate the electrode. The electrode rotation speed was generally set at 2000 rpm and voltammograms were recorded on the second cycle, unless otherwise specified. Voltammetry curves and ring currents were recorded on a Linseis LY 18100 recorder. The collection efficiencies (N) of the ring-disc electrode were determined using freshly prepared 1.0 x 10^{-3} *M* $CuCl_2$ in 0.5 *M* KCl solution (Albery and Hitchman, 1971). The pyrite electrode was held at 0.1 V (SHE) at which no significant current arises from reactions of pyrite itself and Cu^{2+} reduction is under diffusion control. The values of N for the mineral-, Pittsburgh No. 8 coal-, and Chinese coal-pyrite RRDE were found to be 0.38, 0.28 and 0.36, respectively.

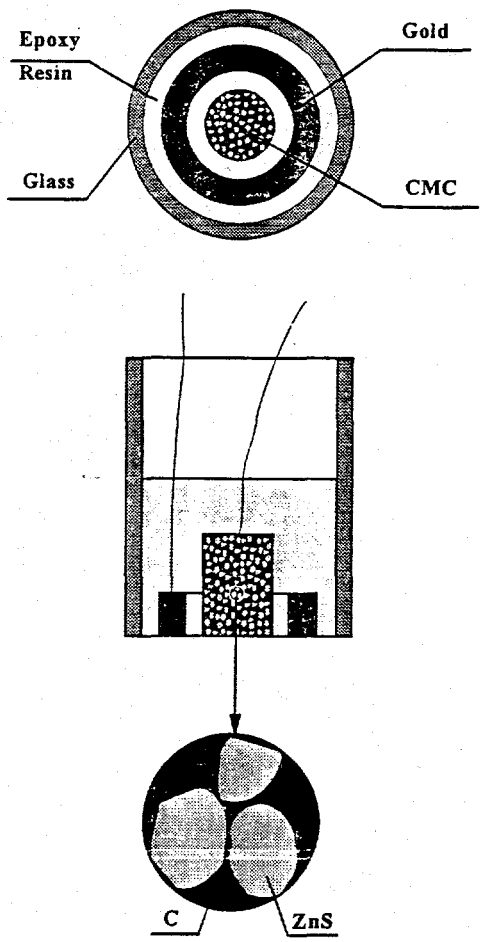

Figure 1. Schematic illustration of the rotating ring-disc electrode.

In situ Fractured Electrodes

The mineral pyrite samples for in situ fractured electrodes had dimensions of approximately 3 x 2 x 10 mm. A copper lead-wire was connected to one of the 3 x 2 mm faces using a conducting silver epoxy. The assembly was then mounted at the end of a 7 mm diameter glass tube with non-conducting epoxy (Torr Seal, Varian), encapsulating about one-half of the electrode. The other half of the electrode was exposed, with the desired fracture plane carefully delineated with epoxy. After the electrode was inserted into the electrochemical cell through an O-ring seal, the projecting portion was subjected to a sharp blow through a glass rod that was inserted through another cell port, resulting in a freshly fractured surface which was usually flush with the epoxy. Each electrode was carefully inspected after experiments to ensure that only the fresh surface was exposed to the electrolyte before the results were accepted.

XPS Study of the Surface Oxidation of Pyrite

The XPS studies were conducted on slabs (10 x 10 x 2 mm) cut from Pittsburgh No. 8 coal-pyrite samples. The measurements were made using a Perkin Elmer Phi 5400 XPS spectrometer equipped with a monochromatized Al Kα X-ray source and a specially-designed drying and cooling chamber. The analyzing chamber of the spectrometer was modified to maintain the sample temperature near 130 K. Maintaining the temperatures at this value prevented the loss of volatile elemental sulfur (if present) from the sample surface.

FTIR Study of Reagent Adsorption on Pyrite

Spectra were recorded using a Bio-Rad FTS 60A Rapid Scan FTIR spectrometer equipped with a liquid nitrogen-cooled mercury cadmium telluride wide-band detector. For each measurement, 256 spectra were recorded, co-added and signal-averaged. The spectral resolution was 4 cm^{-1}. A variable angle reflectance accessory (Spectra Tech) was used with an angle of incidence of 45°. A wire

grid polarizer (Harrick Scientific Corporation) was used to polarize the incident beam parallel to the plane of reflection (p-polarized).

Flotation

Pure Pyrite

Flotation tests of nearly pure pyrite were conducted both in a Partridge and Smith-type microflotation cell (Partridge and Smith, 1971) with a volume of 150 ml and in a specially designed electrochemical-microflotation cell with a volume of 50 ml. Pyrite samples were hand selected and freshly ground to the required size fraction prior to each experiment in order to minimize oxidation.

In the Partridge and Smith cell, the potential of pyrite was adjusted by the addition of oxidizing agents (potassium permanganate) and reducing agents (hydrazine or sodium sulfide). Each flotation test was done with a 0.8 g sample of 100 x 200 mesh particles. The sample was conditioned for 3 minutes at designated potentials before flotation was initiated. Methylisobutylcarbinol (MIBC) was used as frother at a concentration of 30 ppm, unless otherwise specified.

Figure 2 illustrates the electrochemical-microflotation cell in which a compacted pyrite bed is used as the working electrode. A coiled platinum wire lead, entering at (F) and resting on the ground glass frit (E), served as the electrical connection to the mineral bed. A platinum wire, housed in a fine porosity fritted tube (H), served as the counter electrode, and the tube itself served as a plunger to compact the particles to ensure physical and electrical contact throughout the bed. The fine porosity frit prevented diffusion of solutions between the counter and working electrode compartments. Potentials were measured against a saturated Calomel electrode using a Luggin capillary connection through port B. Ports A and C served as the inlet and the outlet for electrolyte circulation respectively. For flotation tests, the counter electrode plunger was raised until the fritted tube was above the center tube but still making electrical contact with the electrolyte. Nitrogen, entering through port D, was

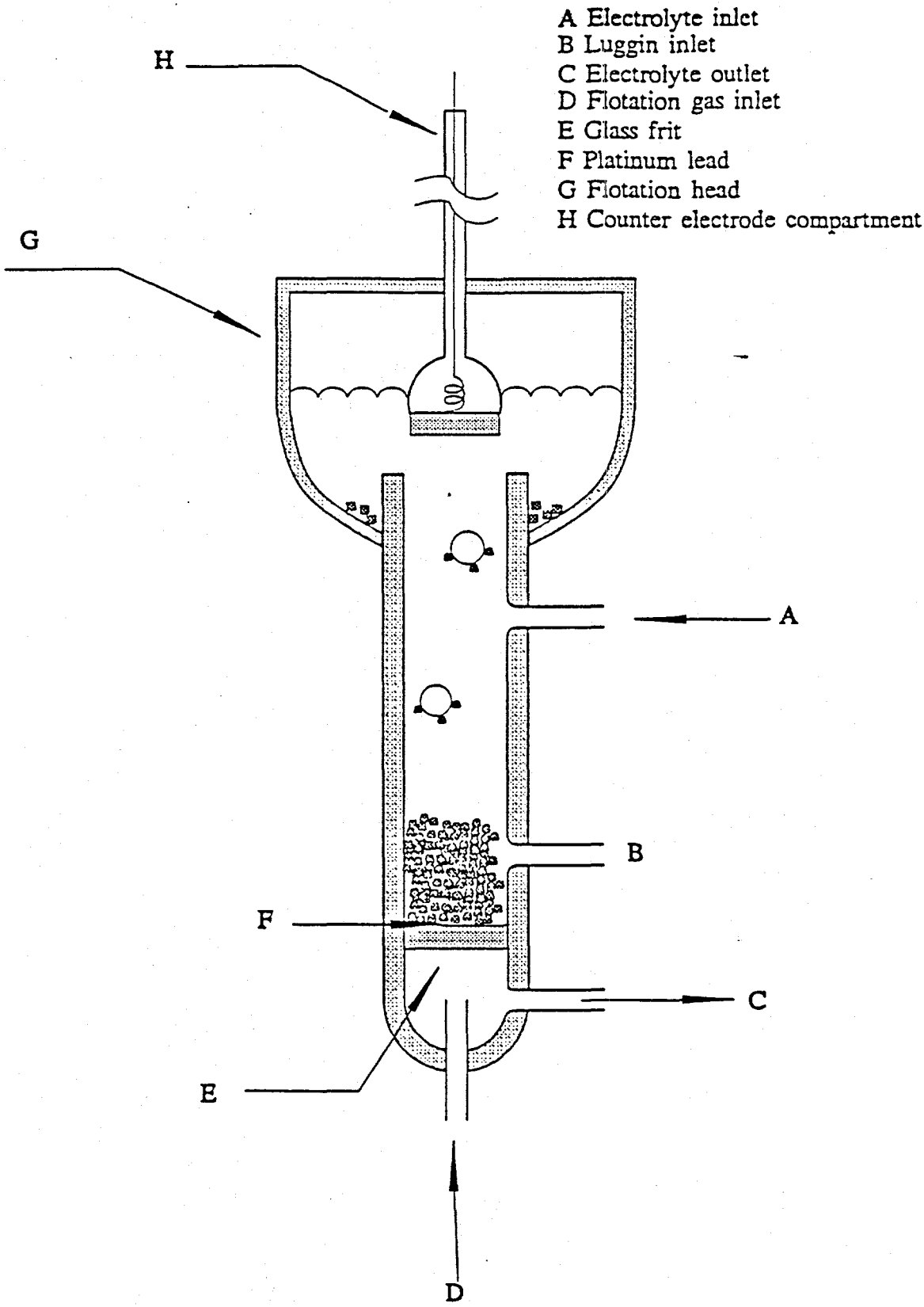

Figure 2. Schematic illustration of the electrochemical-microflotation cell.

bubbled through the frit and mineral bed. Particles levitated by bubbles were deflected by the counter electrode compartment and deposited around the outside of the center tube.

In order to remove possible surface products on pyrite formed during dry grinding, samples were subjected to electrochemical cleaning at -0.5 V in acidic solutions for 5 minutes. The solution was then pumped out and replaced by freshly deoxygenated solution at the required pH.

The main advantage of using the particulate mineral bed instead of a single specimen as the working electrode is that electrochemical studies and flotation tests can be done in the same system under conditions close to the actual flotation environment. In addition, the solution can be continuously circulated between the cell and UV spectrophotometer so that the solution phase can be monitored. The bed used in the present study consisted of a 15 g sample of pyrite particles. The bed potential was controlled with a PAR 273 potentiostat and voltammograms were recorded on a Linseis LY 18100 recorder.

Coal

Coal flotation tests were conducted in a 3/4" diameter microbubble flotation column. The flotation column has been described in detail elsewhere (Yoon et al., 1989). The operating conditions were as follows: aeration rate of 200 ml/min, wash water flow rate 150 ml/min, feed flow rate 70 ml/min, frother dosage of 0.45 kg/ton, froth height of 15 cm, and feed solids content of 5%.

Galvanic Coupling

Galvanic interaction between pyrite and active metals as sacrificial anodes was studied in the electrochemical cell illustrated in Figure 3. The system essentially consists of two independent electrochemical cells connected by a salt bridge. Galvanic coupling between pyrite and metal electrodes was accomplished by connecting them with a copper wire. The effect of galvanic coupling

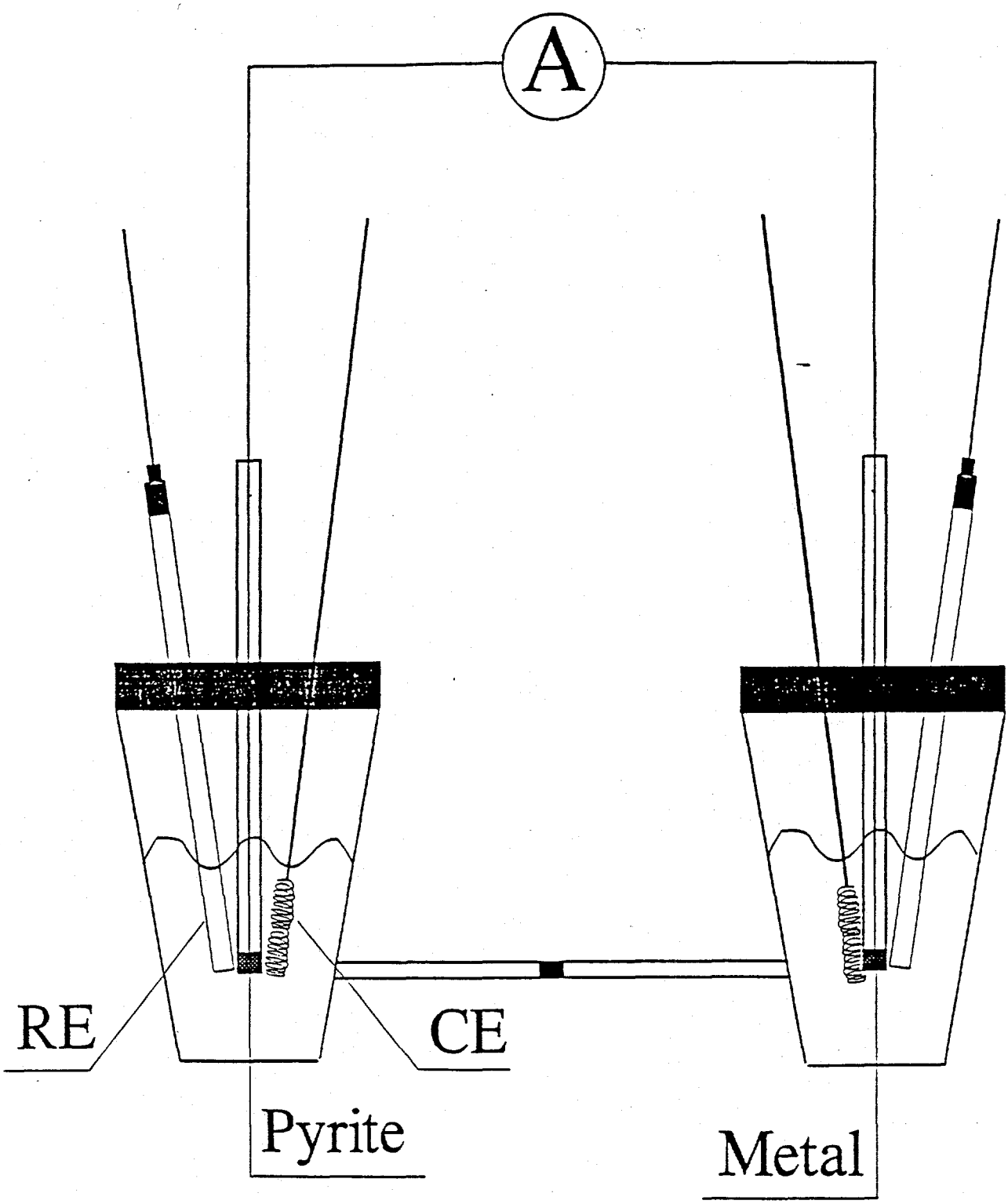

Figure 3. Schematic illustration of the electrochemical cell for galvanic coupling experiments.

on pyrite was investigated by carrying out voltammetry on pyrite after galvanic coupling and after disconnecting two electrodes.

Materials

Large specimens of mineral pyrite, originating from Huanzala, Peru, were obtained through Ward's Scientific Co. The Pittsburgh No. 8 coal-pyrite was originally a chunk of 2.5" x 2.3" x 2" pyrite found in a run-of-mine coal sample. This pyrite sample contained approximately 3% coal on the surface. The coal pyrite specimen from Sichuan, China contained no visible specks of coal and had the appearance of mineral pyrite.

The as-received coal samples were immediately crushed to minus 6 mm using a laboratory jaw crusher and split into representative lots of approximately 1.5 kg each. The samples were stored in a freezer at -20° C to minimize oxidation. Prior to flotation, they were dry pulverized in a laboratory hammermill to minus 100 mesh. Samples of run-of-mine coal from the Illinois No. 6 and Pittsburgh No. 8 coal seams were used in the coal flotation tests using a 3/4"-diameter column for testing of PESR and EESR processes.

Reagents

Buffer solutions used in all electrochemical tests were prepared in double-distilled water using reagent grade chemicals with the following compositions:

pH 4.6; 0.5 *M* CH_3COOH and 0.5 *M* CH_3COONa

pH 6.8; 0.05 *M* KH_2PO_4 and 0.0224 *M* NaOH

pH 9.2; 0.05 *M* $Na_2B_4O_7$

Fresh iron (II) solutions were prepared by dissolving $FeCl_2$ in deoxygenated distilled water and HS^- solutions by dissolving Na_2S. Both $FeCl_2$ and Na_2S were reagent grade.

RESULTS AND DISCUSSION

Task 2 - Characterization

Subtask 2.1: Coal Samples and Characterization

The purpose of this subtask was (i) to obtain three coal samples for use in evaluating the enhanced pyritic sulfur rejection technologies developed in this project, and (ii) to provide a complete characterization of these samples as a baseline for this evaluation. The work was initiated by obtaining one 200-liter container each of run-of-mine Pittsburgh No. 8, Illinois No. 6 and Upper Freeport coal. The Pittsburgh No. 8 sample was obtained from northern West Virginia, the Illinois No. 6 sample from southern Illinois, and the Upper Freeport sample was provided by personnel from Kaiser Engineers working at the OCTAD facility in Ohio. Upon arrival, the samples were spread out and allowed to dry at ambient temperature to remove excess surface moisture. The dried samples were then crushed in a laboratory jaw crusher followed by a roll crusher to produce a muns 6 mm product for storage. Representative samples of minus 6 mm material were collected for each of the three coals and subjected to analyses for ash, volatile matter, fixed carbon, total sulfur, pyritic sulfur and calorific value. The results of these analyses are shown in Table 1.

Table 1. Analysis of the R-O-M feed coals (Dry Basis).

	Pittsburgh No. 8	Illinois No. 6	Upper Freeport
Ash (%)	13.59	48.49	21.25
Total Sulfur (%)	3.60	4.23	5.06
Pyritic Sulfur (%)	1.85	3.26	2.49
Volatile Matter (%)	34.43	22.00	31.24
Fixed Carbon (%)	51.98	29.51	47.51
Calorific Value (Btu/lb)	11,783	6,634	11,196

The minus 6 mm material was further reduced in size to produce the three size fractions (minus 28 mesh, minus 100 mesh and minus 400 mesh) required for this project. The minus 28 mesh fraction was produced by using a roll crusher in closed-circuit with a 28-mesh screen. The closed circuit arrangement was used to minimize the production of fines. Similarly, the minus 100 mesh fraction was prepared by using a laboratory hammer mill containing a 100-mesh screen. Finally, the minus 400 mesh fraction was prepared from the minus 100 mesh material by wet grinding in a laboratory batch ball mill. The mill was operated in locked-cycle with a 400-mesh screen to prevent overgrinding and ensure the 400-mesh top size of the final product. The final size distributions for each of the three size fractions, as determined by wet screening, are shown in Tables 2-4. As shown, all samples are in the range of 90-95% passing the stated size as specified in the Project Work Plan.

Table 2. Size distributions for minus 28 mesh coal samples.

Size Class (Mesh)	Pittsburgh No. 8		Illinois No. 6		Upper Freeport	
	Wt. % in Class	Wt. % Passing	Wt. % in Class	Wt. % Passing	Wt. % in Class	Wt. % Passing
28 x 35	28.06	100.00	27.40	100.00	24.11	100.00
35 x 48	19.17	71.94	18.27	72.60	18.72	75.89
48 x 65	14.33	52.77	11.53	54.33	19.12	57.17
65 x 100	9.91	38.44	11.21	42.80	3.88	38.05
100 x 150	9.09	28.53	5.85	31.59	7.07	34.17
150 x 200	5.25	19.44	5.97	25.74	5.08	27.10
200 x 270	3.85	14.19	3.71	19.77	3.69	22.02
270 x 400	2.71	10.34	2.26	16.06	3.19	18.33
-400	7.63	7.63	13.80	13.80	15.14	15.14

Table 3. Size distributions for minus 100 mesh coal samples.

Size Class (Mesh)	Pittsburgh No. 8		Illinois No. 6		Upper Freeport	
	Wt. % in Class	Wt. % Passing	Wt. % in Class	Wt. % Passing	Wt. % in Class	Wt. % Passing
+100	4.20	100.00	9.28	100.00	6.52	100.00
100 x 150	8.98	95.80	16.88	90.72	15.62	93.48
150 x 200	13.86	86.82	13.99	73.84	15.55	77.86
200 x 270	15.52	72.96	12.20	59.85	12.41	62.31
270 x 400	13.18	57.44	9.98	47.65	10.75	49.90
-400	44.26	44.26	37.67	37.67	39.15	39.15

Table 4. Size distributions for minus 400 mesh coal samples.

Size Class (Mesh)	Pittsburgh No. 8		Illinois No. 6		Upper Freeport	
	Wt. % in Class	Wt. % Passing	Wt. % in Class	Wt. % Passing	Wt. % in Class	Wt. % Passing
+400	5.59	100.00	6.48	100.00	12.45	100.00
-400	94.41	94.41	93.52	93.52	87.55	87.55

Release analysis tests were conducted on all three size fractions for each coal using a Denver Model D-25 laboratory flotation cell and BETZ M-150 as the frother. No hydrocarbon collector was used in this exercise. The results of these tests are shown in Figures 4-9 and the raw data are provided in Tables 5-13.

As shown in Figures 4 and 5, the release analysis results for the Pittsburgh No. 8 sample indicate no improvement in ash rejection when the sample size is reduced from minus 28 to minus 100 mesh, and only a small improvement when the size is reduced further to minus 400 mesh. Furthermore, the pyrite rejection curve stays essentially the same for all size distributions. This tends to

indicate that the pyrite in the Pittsburgh No. 8 coal is either locked with hydrophobic carbonaceous material or is recovered by flotation due to its own hydrophobicity.

A similar result is observed for the Illinois No. 6 sample (Figures 6 and 7); however, in this case, there is no change in either ash rejection or pyrite rejection as a function of feed size. Since most mineral matter is not hydrophobic, it is expected that the insensitivity to feed size is largely a result of locking problems. In other words, the mineral matter and pyrite are so finely disseminated that they are not sufficiently liberated even at minus 400 mesh. Of course, this conclusion can only be verified by image analysis data, which are discussed under Subtask 2.2.

Finally, the Upper Freeport sample (Figures 8 and 9), appears to show a similar trend to the other two samples in terms of liberation, although the ash rejection does seem to improve when the feed size is reduced from minus 28 to minus 100 mesh. On the other hand, the pyrite rejection shows little improvement over this same size range. It should be noted that the minus 400 mesh data are included for completeness; however, the sample was heavily oxidized by the time this final test was conducted and the results are clearly suspect.

In general, the release analysis results tend to indicate that there is little hope of improving pyrite rejection from the three coals studied here simply by grinding to a finer size. This may be due to the fact that pyrite is floatable or it may be due to the presence of carbonaceous material locked with pyrite. Only the image analysis results to be presented under Subtask 2.2 can discern the actual cause. In any case, the pyrite rejection schemes studied in this investigation are capable of addressing either problem.

Table 5. Release analysis results for minus 28 mesh Pittsburgh No. 8 coal.

Sample Type	Individual				Cumulative				Recovery	Rejection		
	Weight (%)	Ash (%)	Sulfur (%)	Pyritic Sulfur (%)	Weight (%)	Ash (%)	Sulfur (%)	Pyritic Sulfur (%)	Combustible (%)	Ash (%)	Sulfur (%)	Pyritic Sulfur (%)
F1	41.31	4.06	2.49	0.68	41.31	4.06	2.49	0.68	45.09	86.13	70.72	84.52
F2	26.59	6.22	2.88	1.17	67.90	4.91	2.64	0.87	73.45	72.45	48.92	67.37
F3	19.59	10.30	4.19	2.24	87.49	6.11	2.99	1.18	93.44	55.76	25.56	43.19
F4	4.32	23.99	8.07	6.29	91.81	6.95	3.23	1.42	97.18	47.19	15.64	28.21
Tail	8.19	69.68	6.71	6.25	100.0	12.09	3.51	1.81	100.00	0.00	0.00	0.00

Table 6. Release analysis results for minus 100 mesh Pittsburgh No. 8 coal.

Sample Type	Individual				Cumulative				Recovery	Rejection		
	Weight (%)	Ash (%)	Sulfur (%)	Pyritic Sulfur (%)	Weight (%)	Ash (%)	Sulfur (%)	Pyritic Sulfur (%)	Combustible (%)	Ash (%)	Sulfur (%)	Pyritic Sulfur (%)
F1	19.82	3.91	2.21	0.56	19.82	3.91	2.21	0.56	21.73	93.75	86.79	93.99
F2	43.90	5.36	2.62	0.94	63.72	4.91	2.49	0.82	69.16	74.75	52.10	71.66
F3	24.16	9.41	3.52	2.04	87.88	6.15	2.77	1.16	94.14	56.41	26.45	45.02
F4	4.74	25.40	8.67	7.19	92.62	7.13	3.08	1.46	98.18	46.69	14.05	26.57
Tail	7.38	78.38	6.31	6.65	100.0	12.39	3.32	1.85	100.00	0.00	0.00	0.00

Table 7. Release analysis results for minus 400 mesh Pittsburgh No. 8 coal.

Sample Type	Individual				Cumulative				Recovery	Rejection		
	Weight (%)	Ash (%)	Sulfur (%)	Pyritic Sulfur (%)	Weight (%)	Ash (%)	Sulfur (%)	Pyritic Sulfur (%)	Combustible (%)	Ash (%)	Sulfur (%)	Pyritic Sulfur (%)
F1	18.57	3.28	2.08	0.52	18.57	3.28	2.08	0.52	20.21	94.53	88.01	94.47
F2	22.43	3.80	2.14	0.64	41.00	3.56	2.11	0.59	44.50	86.87	73.11	86.26
F3	43.02	6.56	2.66	1.25	84.02	5.10	2.39	0.93	89.72	61.52	37.60	55.49
F4	9.36	16.26	8.72	7.11	93.38	6.22	3.03	1.55	98.54	47.84	12.26	17.39
Tail	6.62	80.43	5.97	4.59	100.0	11.13	3.22	1.75	100.00	0.00	0.00	0.00

Table 8. Release analysis results for minus 28 mesh Illinois No. 6 coal.

Sample Type	Individual				Cumulative				Recovery	Rejection		
	Weight (%)	Ash (%)	Sulfur (%)	Pyritic Sulfur (%)	Weight (%)	Ash (%)	Sulfur (%)	Pyritic Sulfur (%)	Combustible (%)	Ash (%)	Sulfur (%)	Pyritic Sulfur (%)
F1	14.17	4.29	2.70	0.72	14.17	4.29	2.70	0.72	26.73	98.77	91.34	96.98
F2	21.98	10.45	3.73	1.89	36.15	8.03	3.33	1.43	65.52	94.10	72.79	84.69
F3	8.10	19.78	4.92	3.04	44.25	10.18	3.62	1.73	78.33	90.85	63.77	77.40
F4	11.17	50.49	7.94	6.93	55.42	18.31	4.49	2.77	89.23	79.40	43.69	54.49
Tail	44.58	87.74	4.33	4.13	100.0	49.26	4.42	3.38	100.00	0.00	0.00	0.00

Table 9. Release analysis results for minus 100 mesh Illinois No. 6 coal.

Sample Type	Individual				Cumulative				Recovery	Rejection		
	Weight (%)	Ash (%)	Sulfur (%)	Pyritic Sulfur (%)	Weight (%)	Ash (%)	Sulfur (%)	Pyritic Sulfur (%)	Combustible (%)	Ash (%)	Sulfur (%)	Pyritic Sulfur (%)
F1	12.53	5.06	2.82	0.99	12.53	5.06	2.82	0.99	21.29	98.56	91.79	96.01
F2	39.08	12.47	3.93	2.19	51.61	10.67	3.66	1.90	82.55	87.53	56.09	68.50
F3	4.15	37.74	6.59	5.57	55.76	12.69	3.88	2.17	87.18	83.98	49.73	61.06
F4	4.37	59.05	9.64	8.25	60.13	16.06	4.30	2.61	90.38	78.13	39.94	49.48
Tail	39.87	86.53	4.31	3.86	100.0	44.15	4.30	3.11	100.00	0.00	0.00	0.00

Table 10. Release analysis results for minus 400 mesh Illinois No. 6 coal.

Sample Type	Individual				Cumulative				Recovery	Rejection		
	Weight (%)	Ash (%)	Sulfur (%)	Pyritic Sulfur (%)	Weight (%)	Ash (%)	Sulfur (%)	Pyritic Sulfur (%)	Combustible (%)	Ash (%)	Sulfur (%)	Pyritic Sulfur (%)
F1	11.24	7.94	2.76	1.04	11.24	7.94	2.76	1.04	19.16	98.06	93.11	96.37
F2	30.68	10.98	3.36	1.56	41.92	10.16	3.20	1.42	69.73	90.74	70.20	81.51
F3	9.49	19.30	4.98	3.11	51.41	11.85	3.53	1.73	83.91	86.76	59.70	72.35
F4	6.23	42.86	8.45	6.53	57.64	15.20	4.06	2.25	90.50	80.95	48.01	59.72
Tail	42.36	87.89	5.10	4.54	100.0	46.00	4.50	3.22	100.00	0.00	0.00	0.00

Table 11. Release analysis results for minus 28 mesh Upper Freeport coal.

Sample Type	Individual				Cumulative				Recovery	Rejection		
	Weight (%)	Ash (%)	Sulfur (%)	Pyritic Sulfur (%)	Weight (%)	Ash (%)	Sulfur (%)	Pyritic Sulfur (%)	Combustible (%)	Ash (%)	Sulfur (%)	Pyritic Sulfur (%)
F1	53.76	9.07	3.10	1.46	53.76	9.07	3.10	1.46	58.27	69.73	61.42	68.48
F2	23.99	17.81	4.32	2.44	77.75	11.77	3.48	1.76	81.77	43.20	37.37	45.04
F3	4.19	24.57	10.10	8.72	81.94	12.42	3.82	2.12	85.54	36.83	27.54	30.24
Tail	18.06	32.82	6.59	4.18	100.0	16.11	4.32	2.49	100.00	0.00	0.00	0.00

Table 12. Release analysis results for minus 100 mesh Upper Freeport coal.

Sample Type	Individual				Cumulative				Recovery	Rejection		
	Weight (%)	Ash (%)	Sulfur (%)	Pyritic Sulfur (%)	Weight (%)	Ash (%)	Sulfur (%)	Pyritic Sulfur (%)	Combustible (%)	Ash (%)	Sulfur (%)	Pyritic Sulfur (%)
F1	5.10	8.15	2.86	1.27	5.10	8.15	2.86	1.27	5.98	98.08	97.50	97.85
F2	81.33	15.56	4.39	2.75	86.43	15.12	4.30	2.66	93.67	39.72	36.25	23.62
F3	2.20	46.80	12.90	10.50	88.63	15.91	4.51	2.85	95.16	34.96	31.44	16.08
Tail	11.37	66.64	16.08	6.23	100.0	21.68	5.83	3.01	100.00	0.00	0.00	0.00

Table 13. Release analysis results for minus 400 mesh Upper Freeport coal.

Sample Type	Individual				Cumulative				Recovery	Rejection		
	Weight (%)	Ash (%)	Sulfur (%)	Pyritic Sulfur (%)	Weight (%)	Ash (%)	Sulfur (%)	Pyritic Sulfur (%)	Combustible (%)	Ash (%)	Sulfur (%)	Pyritic Sulfur (%)
F1	3.78	13.19	3.14	1.49	3.78	13.19	3.14	1.49	4.16	97.64	97.44	97.73
F2	59.43	15.18	3.76	2.05	63.21	15.06	3.72	2.02	68.06	54.91	49.21	48.51
F3	12.94	17.09	4.38	2.52	76.15	15.41	3.83	2.10	81.65	44.41	37.01	35.52
Tail	23.85	39.32	7.16	3.67	100.0	21.11	4.63	2.48	100.00	0.00	0.00	0.00

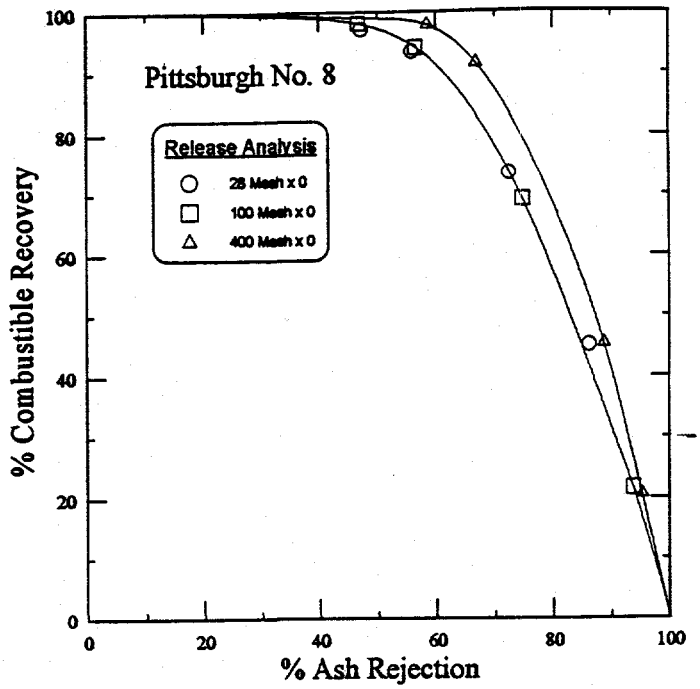

Figure 4. Release analysis on ash for three size fractions of Pittsburgh No. 8 coal.

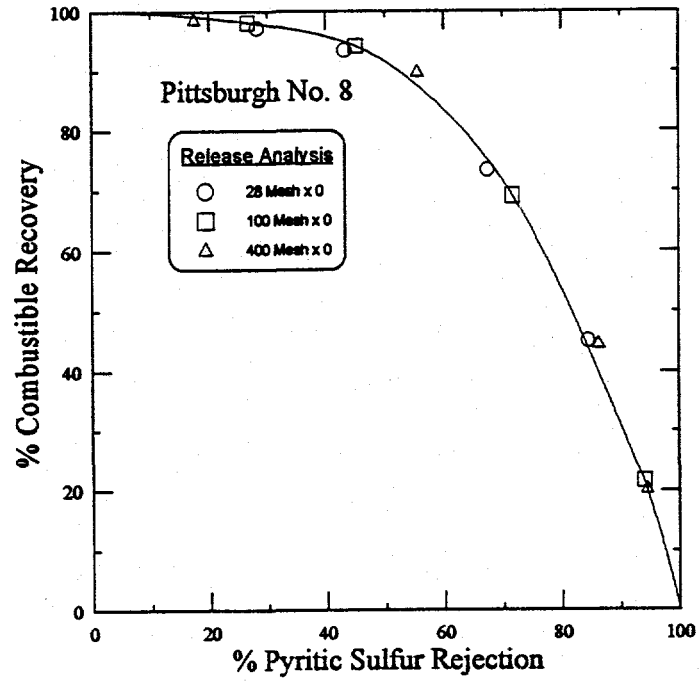

Figure 5. Release analysis on pyritic sulfur for three size fractions of Pittsburgh No. 8 coal.

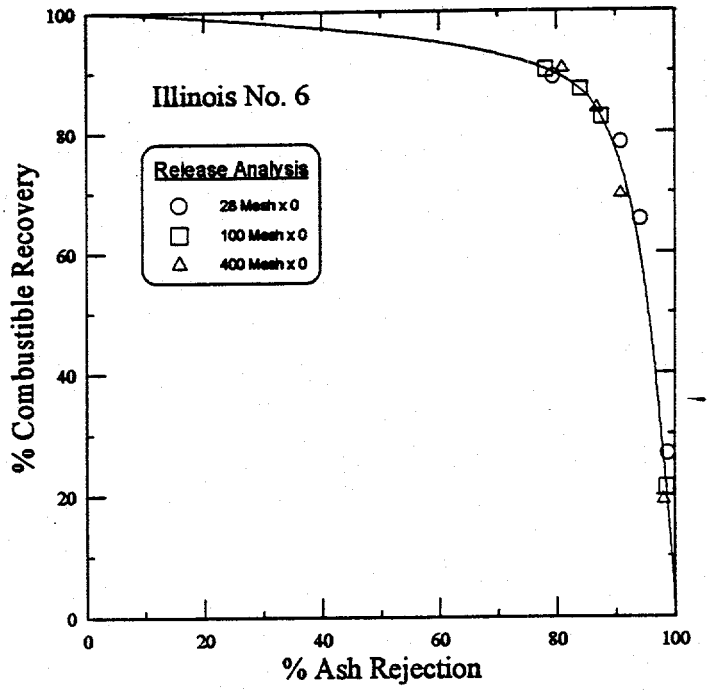

Figure 6. Release analysis on ash for three size fractions of Illinois No. 6 coal.

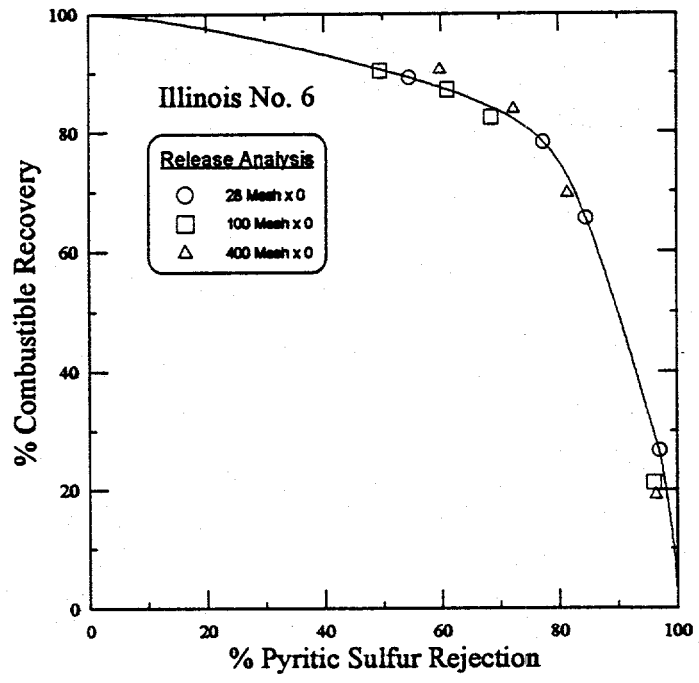

Figure 7. Release analysis on pyritic sulfur for three size fractions of Illinois No. 6 coal.

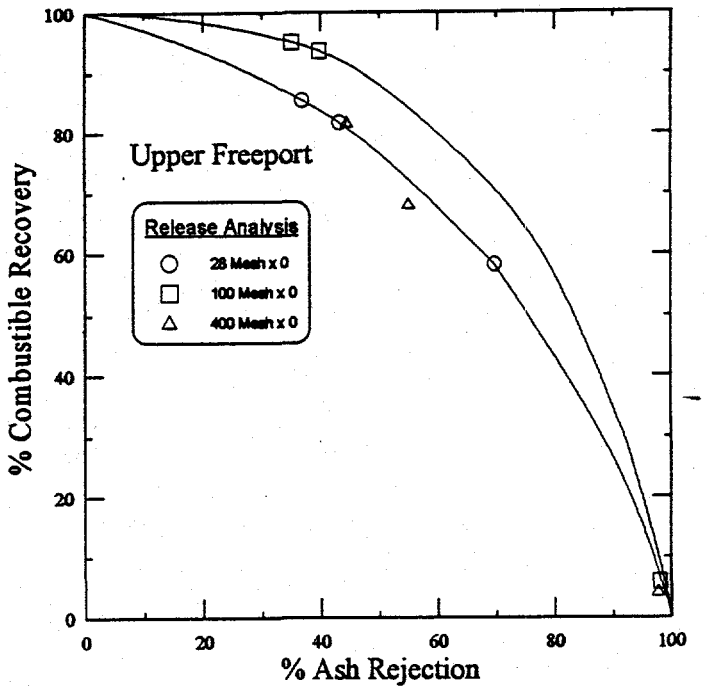

Figure 8. Release analysis on ash for three size fractions of Upper Freeport coal.

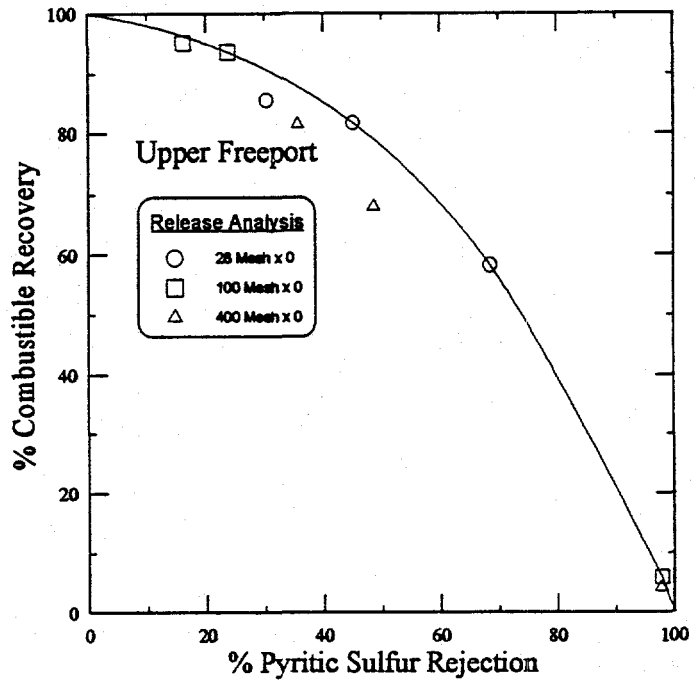

Figure 9. Release analysis on pyritic sulfur for three size fractions of Upper Freeport coal.

In addition to release analysis tests, float-sink tests were originally scheduled to be carried out on all three size fractions of each coal sample. Unfortunately, after numerous attempts to obtain accurate centrifugal float-sink data, the results proved to be unreliable. In many cases, the centrifugal float-sink results were found to deteriorate as particle size was reduced, and in some cases, the separation curve obtained by centrifugal float-sink analysis was worse than the release analysis result.

Tables 14 and 15 and Figures 10-13 show the results obtained using centrifugal float-sink analysis to characterize all three size fractions of the Pittsburgh No. 8 and Illinois No. 6 samples. These results are compared to the release analysis results. For the Pittsburgh No. 8 sample (Figures 10 and 11), the float-sink separation is slightly better than release analysis in terms of total sulfur rejection, but it generally falls below release analysis in terms of ash rejection. Furthermore, the float-sink analysis produces a separation which deteriorates as particle size decreases. In the case of the Illinois No. 6 sample (Figures 12 and 13), the float-sink result is generally inferior to release analysis in terms of both ash and sulfur rejection. Furthermore, the separation once again deteriorates as particle size is reduced. Clearly, these findings are contrary to common sense.

Table 14. Centrifugal float-sink results for Pittsburgh No. 8 coal.

S.G.	28 x 0			100 x 0			400 x 0		
	Ash Rej.	Sulfur Rej.	Comb. Rec.	Ash Rej.	Sulfur Rej.	Comb. Rec.	Ash Rej.	Sulfur Rej.	Comb. Rec.
1.31	89.76	73.60	41.97	94.96	89.31	20.77	100.00	100.00	1.30
1.35	77.62	64.26	64.06	86.11	75.14	48.71	93.14	89.88	16.72
1.41	68.70	49.31	86.15	82.68	70.26	59.51	81.66	72.41	48.80
1.60	61.59	0.00	89.16	61.23	50.27	75.79	50.10	45.88	75.61
1.80	49.81	0.00	94.71	49.07	41.22	87.43	35.49	32.93	86.92
2.00	40.36	0.00	95.95	39.73	33.58	91.40	25.18	24.40	89.04

Table 15. Centrifugal float-sink results for Illinois No. 6 coal.

S.G.	28 x 0			100 x 0			400 x 0		
	Ash Rej.	Sulfur Rej.	Comb. Rec.	Ash Rej.	Sulfur Rej.	Comb. Rec.	Ash Rej.	Sulfur Rej.	Comb. Rec.
1.31	99.26	100.00	18.73	94.83	100.00	14.11	100.00	100.00	2.68
1.35	98.21	100.00	31.64	98.66	100.00	20.73	100.00	100.00	3.30
1.41	96.58	81.79	51.87	98.30	92.60	24.95	100.00	100.00	3.56
1.60	91.68	75.52	67.48	92.05	78.32	59.71	94.51	91.68	21.14
1.80	84.92	69.67	74.63	73.38	57.24	77.29	76.78	68.02	57.80
2.00	76.21	33.33	80.98	76.03	62.14	81.94		44.26	72.18

Several experimental procedures were tested in order to obtain logical results, but none of these approaches appeared to have any effect. For example, the general procedure was to use an hourglass-shaped vial as the separating vessel and to allow eight of these vessels to rotate in a centrifuge at 5000 rpm for a period of approximately 1 hour. After the float and sink portions were separated, a stopper was carefully inserted into the neck of the vial and the float fraction was removed. This procedure was repeated using a higher specific gravity organic liquid until the necessary specific gravity range had been covered. Because this procedure can lead to several sources of error including particles caught on the stopper, incomplete separation as evidenced by a "murky" fluid between the separated components, and entrapment or entrainment of particles in the float or sink phases, all of these possible sources of error were examined. In fact, Figure 12 shows several points obtained using a form of float-sink "tree" analysis on the 28 mesh x 0 Illinois No. 6 sample. In this case, each float and sink product was repeatedly centrifuged to eliminate any possible entrainment. Unfortunately, no misplaced material was evident after the original separation.

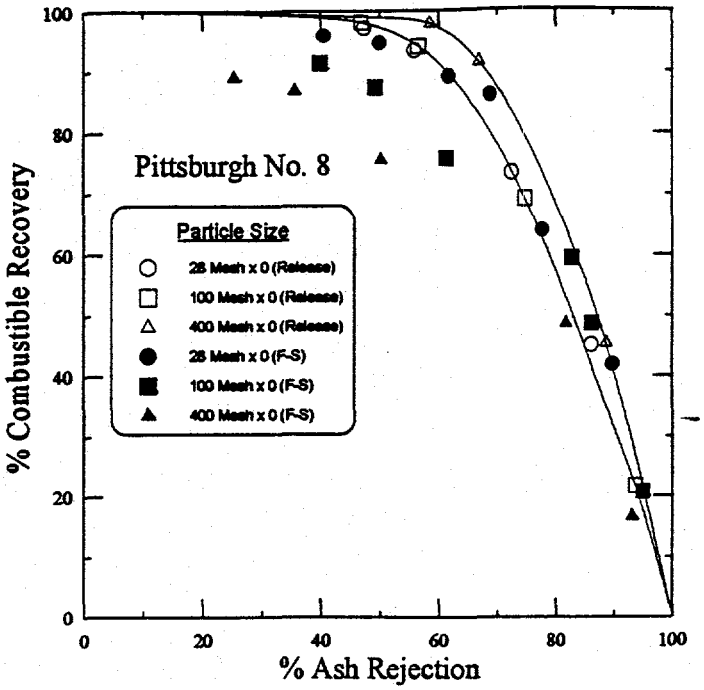

Figure 10. Centrifugal float-sink analysis of Pittsburgh No. 8 sample (ash rejection).

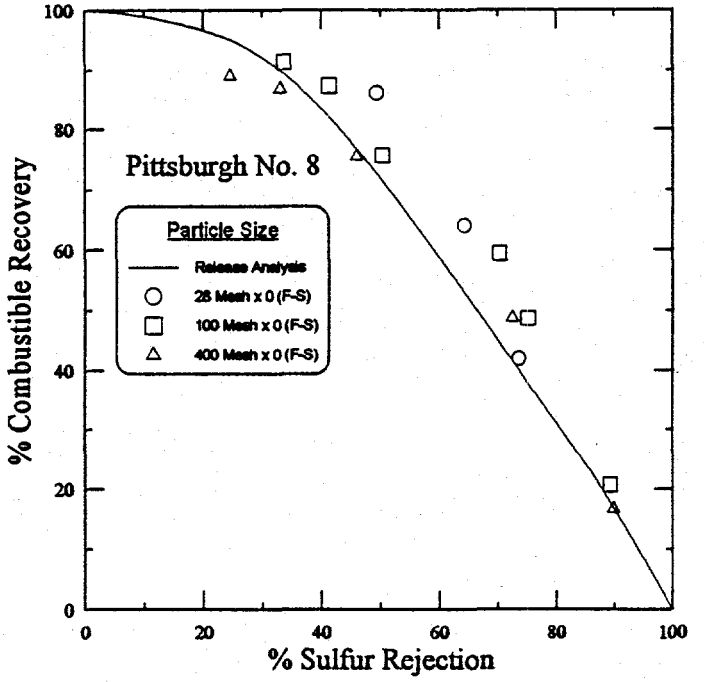

Figure 11. Centrifugal float-sink analysis of Pittsburgh No. 8 sample (sulfur rejection).

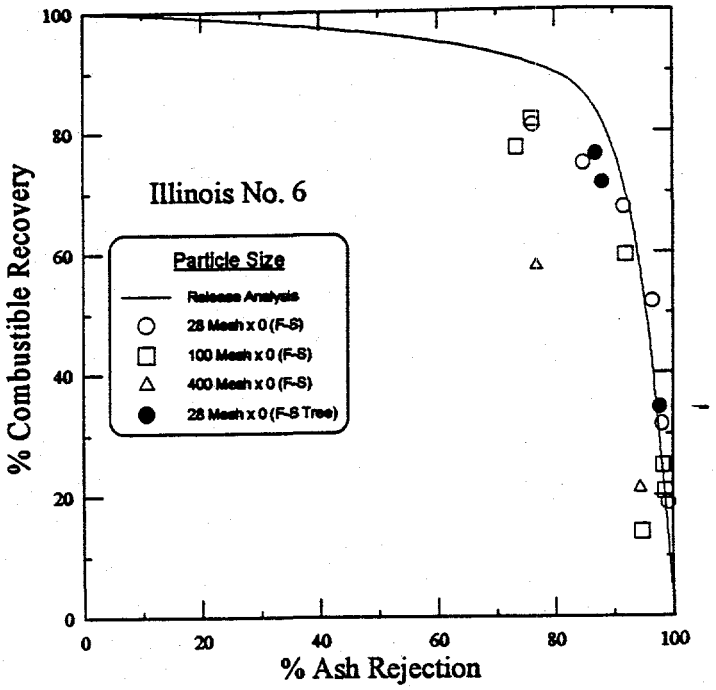

Figure 12. Centrifugal float-sink analysis of Illinois No. 6 sample (ash rejection).

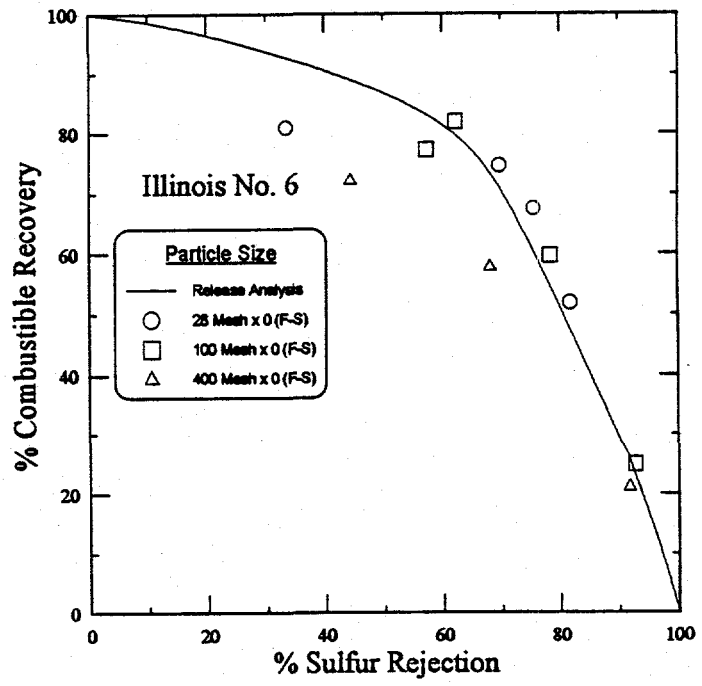

Figure 13. Centrifugal float-sink analysis of Illinois No. 6 sample (sulfur rejection).

After consulting with several experts in the field, including the group at Southern Illinois University currently doing centrifugal maceral separation, the only apparent flaw in the procedure appeared to be the relatively low RPM used. Several individuals indicated the need to use a much higher g-force to obtain proper centrifugal float-sink data. Since a higher-RPM centrifuge was unavailable, and since funds were not budgeted to subcontract this work, it was decided to use the theoretical float-sink results generated from image analysis as an alternative to the centrifugal float-sink testing. In previous work, theoretical float-sink data generated using the image analysis procedure were compared to centrifugal float-sink data generated by Tradet, Inc. using their continuous high-g centrifuge. The results from these two techniques were found to agree quite well (Adel, Wang and Yoon, 1991). Therefore, in the present study, image analysis float-sink data have been used to represent the gravity separation properties of the three coals.

The separation curves constructed from the image analysis data are shown in Figures 14-25 along with the release analysis curves for comparison. The image analysis procedures used to obtain these results are described under Subtask 2.2 - SEM-IPS Analysis of Feed Samples. In essence, the image analysis separation curves represent the expected result from an ideal gravity separation process. The curves are constructed based on the amount of material found in each composition class assuming that particles consisting of 100% carbonaceous material are recovered first, followed by those containing 90%, 80%, etc.

There are several general comments that can be made about the data shown in Figures 14-25. First of all, the image analysis separation curve is almost always better than that obtained using release analysis. This is primarily due to the fact that flotation is a surface-based process. A particle of pyrite which is covered with a thin layer of carbonaceous material can be easily recovered by flotation. On the other hand, this same particle, viewed in cross-section under an SEM, appears to be nearly 100%

pyrite and is classified with the sink material. Thus, the image analysis separation curve is based on bulk properties just as is the curve resulting from traditional float-sink analysis. Secondly, the separation curves (release analysis and image analysis) for a coal sample containing a large amount of extraneous rock, as in the case of the Illinois No. 6 sample, are much closer together than those samples where much of the mineral matter is locked with the carbonaceous material. In other words, if one takes a coal sample and simply adds free rock to the sample, the apparent rejection of mineral matter, by either flotation or gravity separation, will be increased dramatically.

With these general comments in mind, it can be seen in Figures 14-25 that there is very little change in either the image analysis or release analysis curve in going from the minus 28 mesh to the minus 100 mesh sample. It appears that in some cases, e.g., the Pittsburgh No. 8 and Upper Freeport samples, there is a slight improvement in the ash rejection shown by release analysis as the top size is decreased, but the pyrite rejection curves remain essentially unchanged. In terms of the ideal gravity separation curves, i.e., image analysis, the performance is already quite good at minus 28 mesh. Thus, there is no great improvement in going to minus 100 mesh. Overall, it can be seen that the Pittsburgh No. 8 sample should give the best result in terms of gravity separation, followed by the Illinois No. 6 and Upper Freeport samples. On the other hand, the Illinois No. 6 sample should respond better to flotation than either the Pittsburgh No. 8 or Upper Freeport samples. These findings will be discussed in greater detail in light of the liberation spectra described in Subtask 2.2.

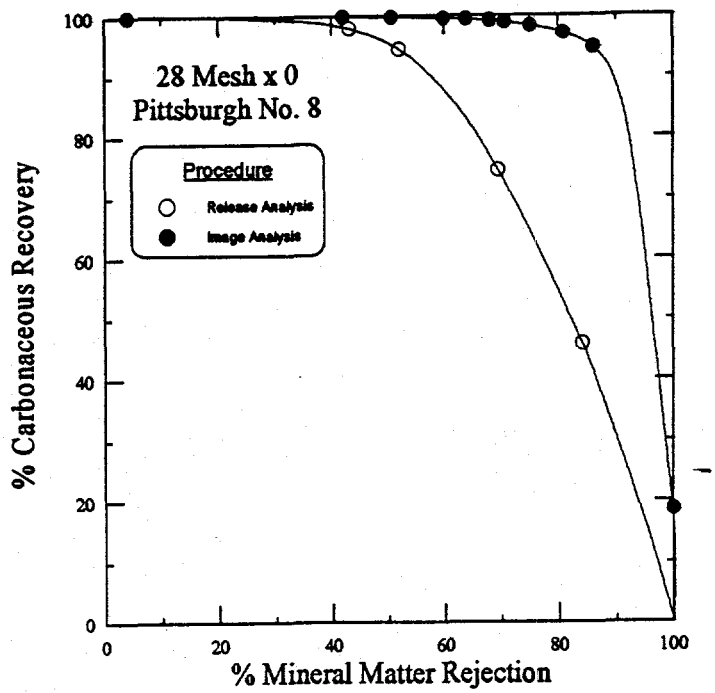

Figure 14. Comparison of release analysis and image analysis separation curves for mineral matter obtained on minus 28 mesh Pittsburgh No. 8 coal.

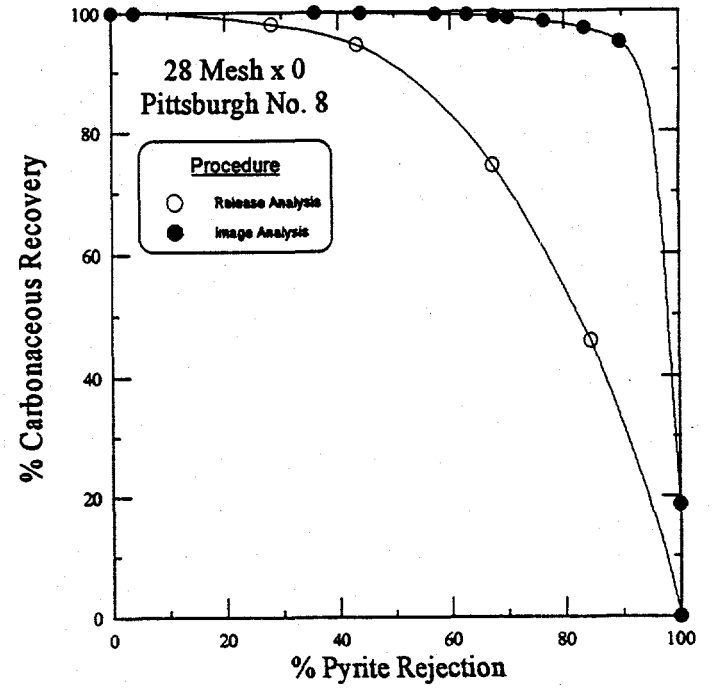

Figure 15. Comparison of release analysis and image analysis separation curves for pyrite obtained on minus 28 mesh Pittsburgh No. 8 coal.

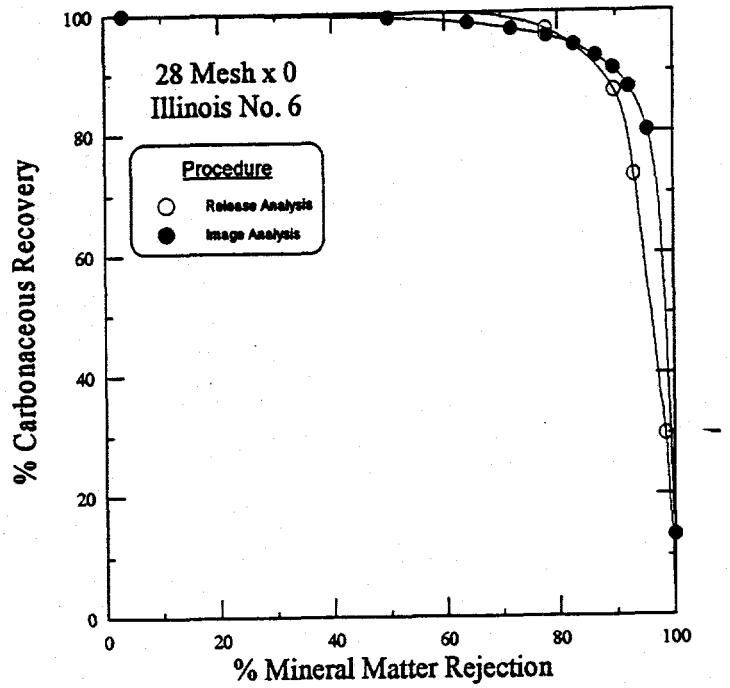

Figure 16. Comparison of release analysis and image analysis separation curves for mineral matter obtained on minus 28 mesh Illinois No. 6 coal.

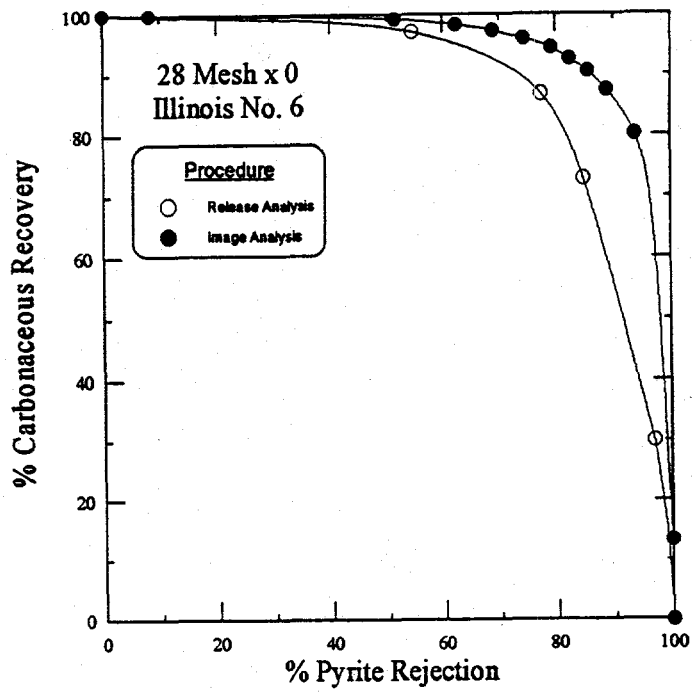

Figure 17. Comparison of release analysis and image analysis separation curves for pyrite obtained on minus 28 mesh Illinois No. 6 coal.

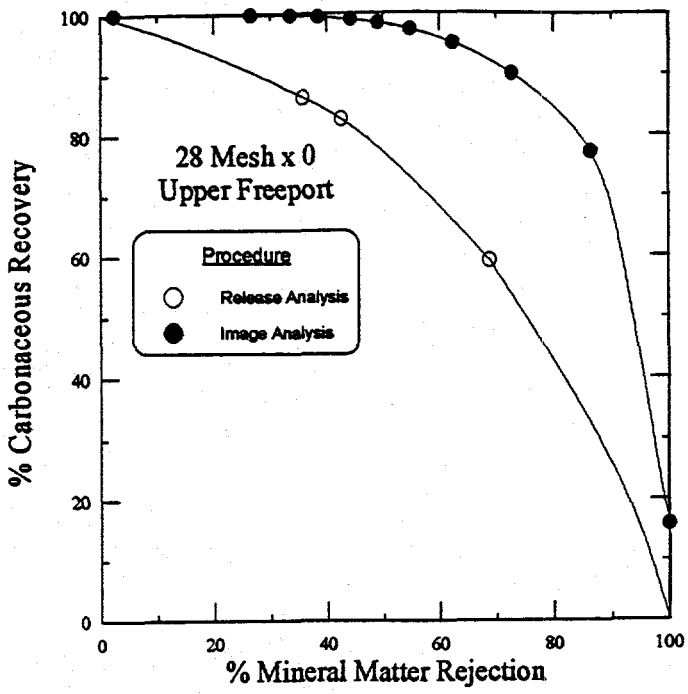

Figure 18. Comparison of release analysis and image analysis separation curves for mineral matter obtained on minus 28 mesh Upper Freeport coal.

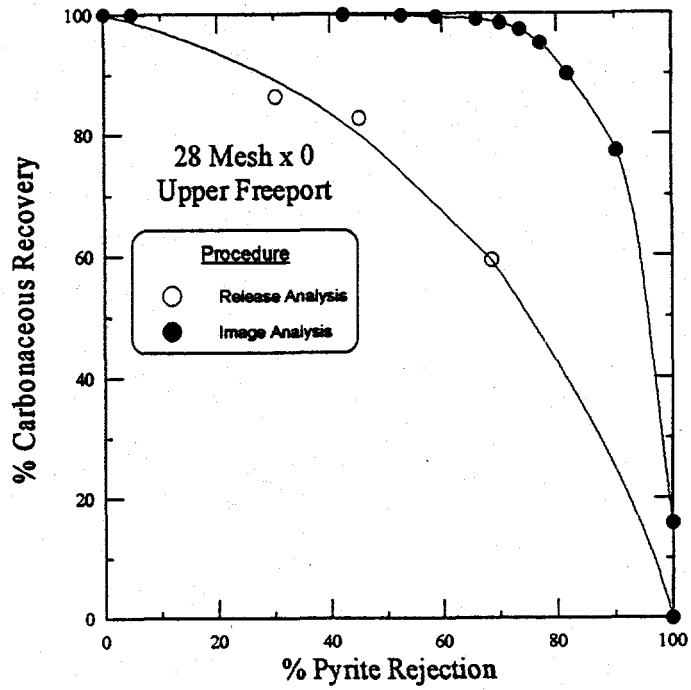

Figure 19. Comparison of release analysis and image analysis separation curves for pyrite obtained on minus 28 mesh Upper Freeport coal.

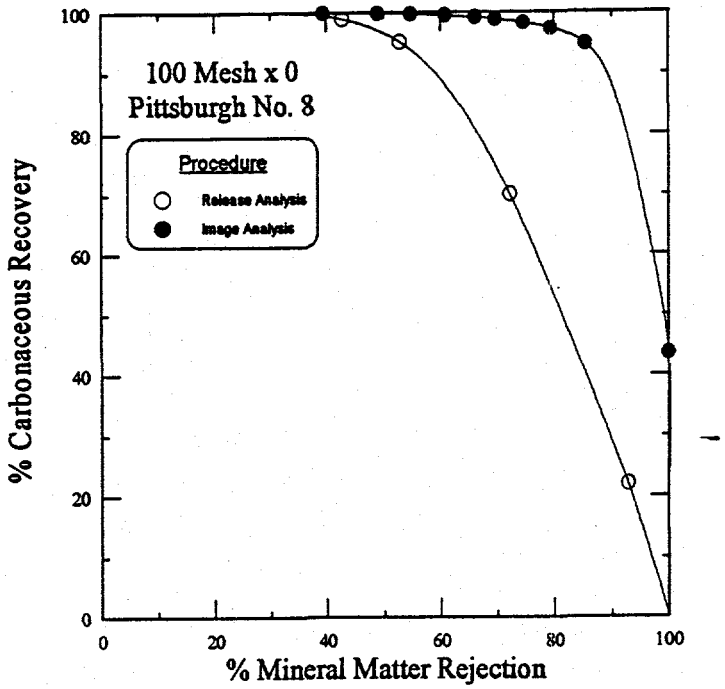

Figure 20. Comparison of release analysis and image analysis separation curves for mineral matter obtained on minus 100 mesh Pittsburgh No. 8 coal.

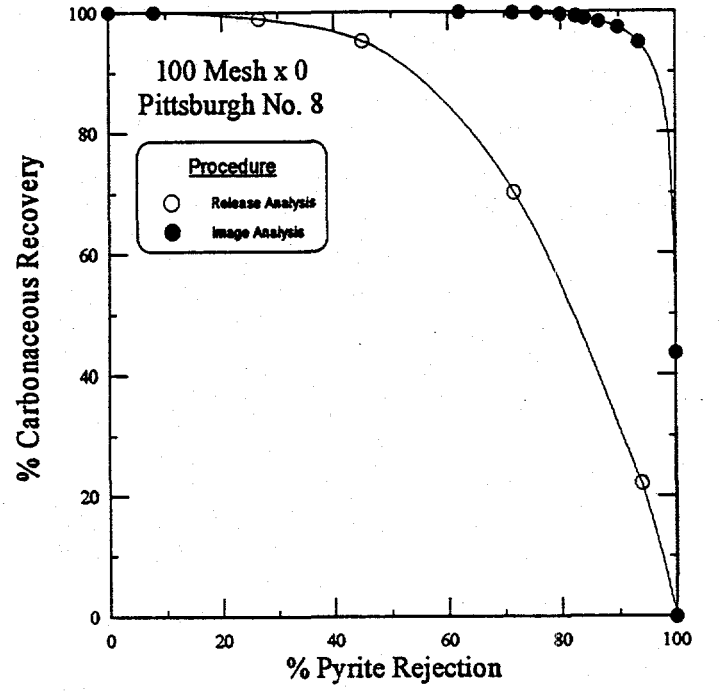

Figure 21. Comparison of release analysis and image analysis separation curves for pyrite obtained on minus 100 mesh Pittsburgh No. 8 coal.

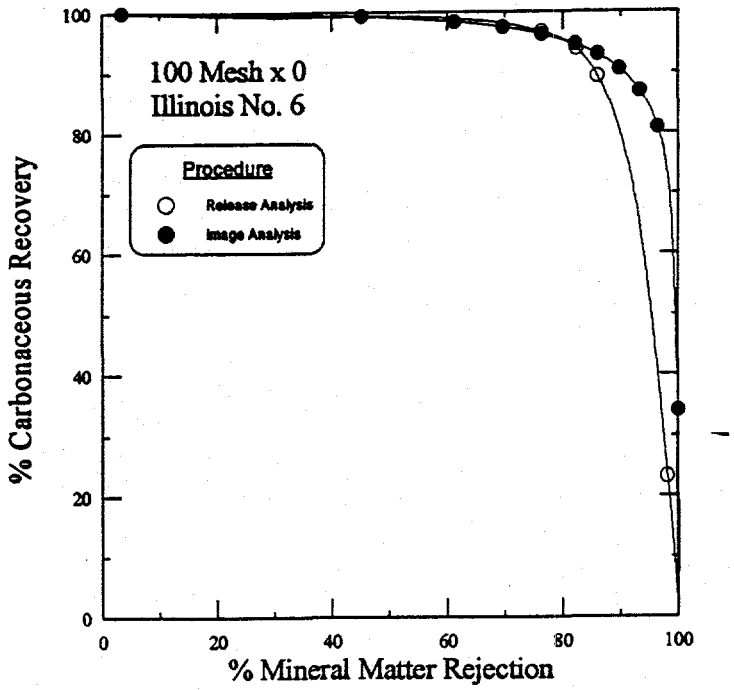

Figure 22. Comparison of release analysis and image analysis separation curves for mineral matter obtained on minus 100 mesh Illinois No. 6 coal.

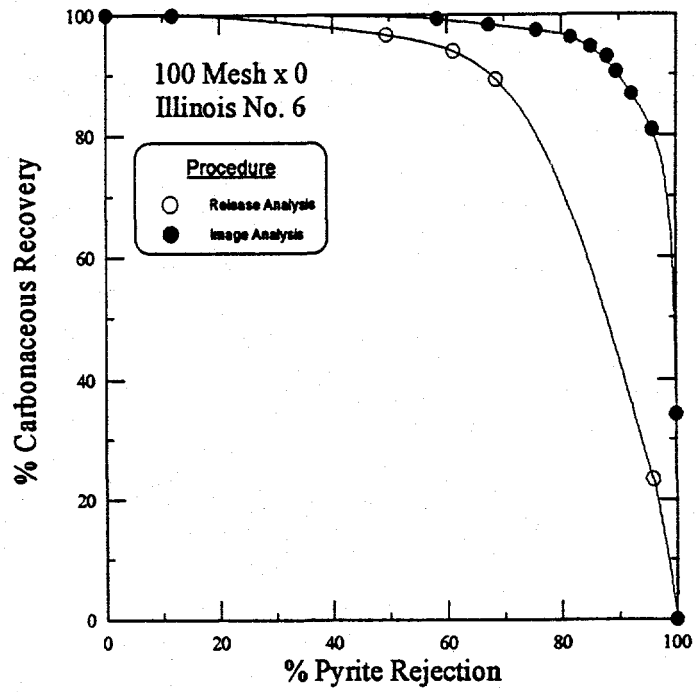

Figure 23. Comparison of release analysis and image analysis separation curves for pyrite obtained on minus 100 mesh Illinois No. 6 coal.

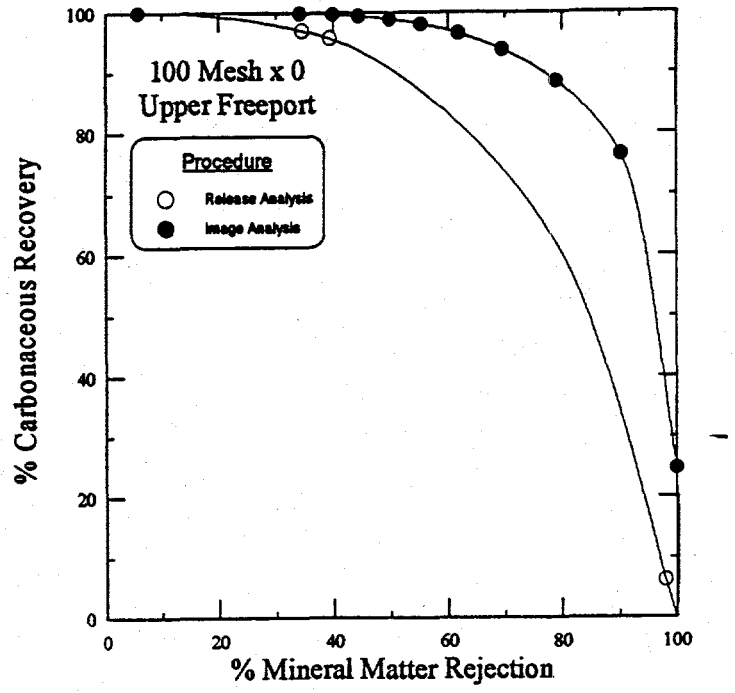

Figure 24. Comparison of release analysis and image analysis separation curves for mineral matter obtained on minus 100 mesh Upper Freeport coal.

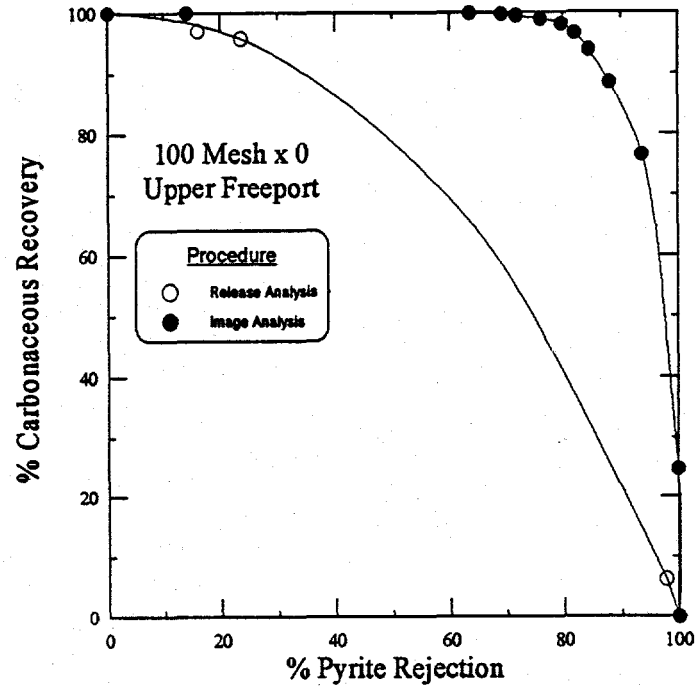

Figure 25. Comparison of release analysis and image analysis separation curves for pyrite obtained on minus 100 mesh Upper Freeport coal.

Subtask 2.2: SEM-IPS Analysis of Feed Samples

The purpose of this subtask was to provide detailed information on the distribution and morphology of the pyrite contained in each of the three coal samples. This information was to be used to assess the potential improvement in pyrite rejection that could be expected from the various enhanced pyrite rejection schemes.

The work was initiated by preparing narrow size fractions from the minus 28 mesh and minus 100 mesh samples produced in Subtask 2.1. These size fractions were to be subjected to analysis under the scanning electron microscope (SEM). In the case of the minus 28 mesh samples, nine (9) different size fractions (28 x 35, 35 x 48, 48 x 65, 65 x 100, 100 x 150, 150 x 200, 200 x 270, 270 x 400, minus 400 mesh) were prepared while in the case of the minus 100 mesh samples, five (5) size fractions (100 x 150, 150 x 200, 200 x 270, 270 x 400, minus 400 mesh) were used. Samples of material from each size fraction were mounted in briquettes consisting of a 1:1 mixture of polyethylene and carnauba wax. This mounting mixture has been found to provide a good separation of the relative gray levels of pyrite, mineral matter, carbonaceous matter and mounting media when viewed under an SEM in the back-scattered electron mode. The briquettes were then polished and analyzed using a Cambridge Stereoscan 120 SEM coupled with a Kontron SEM-IPS image analysis system in order to quantify the various amounts of carbonaceous material, pyrite and other mineral matter present in each particle. Complete details of the sample preparation scheme and analysis procedure are described elsewhere (Adel, Wang and Yoon, 1991; Wang, Adel and Yoon, 1993).

The accuracy of the image analysis procedure is illustrated in Tables 16-21 which show the size-by-size proximate analysis for each sample. Also included in these tables is a comparison of the percent mineral matter as calculated from the Parr formula and as determined directly by image analysis. As shown, the mineral matter content determined by the image analysis technique is

remarkably close to that calculated from the Parr formula. The greatest difference in the two values appears to be in the minus 400 mesh size class which is generally the most difficult to analyze accurately by image analysis. Considering the striking differences in these two techniques for determining mineral matter content, the agreement is quite good.

The same result can be illustrated when the size-by-size proximate analyses are combined to give the overall proximate analysis for each of the minus 28, minus 100 and minus 400 mesh samples. These analyses are compared with the original R-O-M analysis in Tables 22-24. Once again, the agreement between the mineral matter content determined from the Parr formula and that measured directly by image analysis is quite good for the minus 28 mesh sample, and becomes worse as the amount of minus 400 mesh material increases.

Table 16. Size-by-size proximate analysis (dry basis) of minus 28 mesh Pittsburgh No. 8 coal.

Size Class (mesh)	% Ash	% Sulfur	% Volatile Matter	% Fixed Carbon	% MM (Parr)	% MM (I.A.)
28 x 35	14.45	3.84	36.85	48.70	17.72	15.78
35 x 48	12.56	3.90	37.28	50.16	15.71	17.32
48 x 65	11.98	4.00	37.66	50.36	15.14	15.11
65 x 100	11.97	4.09	37.50	50.53	15.18	14.13
100 x 150	11.48	4.36	37.63	50.89	14.80	14.12
150 x 200	8.57	3.55	39.12	52.31	11.21	11.90
200 x 270	13.27	4.83	36.80	49.93	16.99	14.89
270 x 400	11.90	4.18	36.90	51.20	15.15	15.55
-400	20.80	3.88	31.39	47.81	24.60	18.49

Table 17. Size-by-size proximate analysis (dry basis) of minus 28 mesh Illinois No. 6 coal.

Size Class (mesh)	% Ash	% Sulfur	% Volatile Matter	% Fixed Carbon	% MM (Parr)	% MM (I.A.)
28 x 35	37.26	4.97	26.86	35.88	42.97	46.20
35 x 48	39.53	5.26	26.17	34.30	45.59	45.06
48 x 65	37.62	5.42	26.69	35.69	43.61	44.30
65 x 100	40.71	5.63	25.81	33.48	47.06	48.08
100 x 150	37.87	5.77	26.88	35.25	44.07	45.58
150 x 200	38.21	6.00	26.43	35.36	44.57	42.21
200 x 270	45.17	5.95	23.74	31.09	52.06	47.60
270 x 400	38.94	6.02	25.63	35.43	45.37	46.01
-400	71.33	3.69	14.63	14.04	79.07	51.23

Table 18. Size-by-size proximate analysis (dry basis) of minus 28 mesh Upper Freeport coal.

Size Class (mesh)	% Ash	% Sulfur	% Volatile Matter	% Fixed Carbon	% MM (Parr)	% MM (I.A.)
28 x 35	19.15	4.89	34.06	46.79	23.37	26.56
35 x 48	18.83	4.67	34.05	47.12	22.90	20.49
48 x 65	18.62	4.78	33.94	47.44	22.74	21.85
65 x 100	19.35	4.49	33.49	47.16	23.37	27.31
100 x 150	20.09	4.66	33.41	46.50	24.26	23.48
150 x 200	19.99	4.83	32.49	47.52	24.25	20.69
200 x 270	21.28	5.36	32.10	46.62	25.93	30.21
270 x 400	22.16	5.86	30.16	47.68	27.16	27.52
-400	35.53	4.06	24.15	40.32	40.61	34.08

Table 19. Size-by-size proximate analysis (dry basis) of minus 100 mesh Pittsburgh No. 8 coal.

Size Class (mesh)	% Ash	% Sulfur	% Volatile Matter	% Fixed Carbon	% MM (Parr)	% MM (I.A.)
65 x 100	11.38	3.28	37.06	51.56	14.09	14.78
100 x 150	10.07	3.56	37.66	52.27	12.83	10.68
150 x 200	9.63	3.82	38.16	52.21	12.50	10.71
200 x 270	9.62	3.95	38.71	51.67	12.56	11.63
270 x 400	9.46	3.91	38.23	52.31	12.37	13.34
-400	15.64	3.58	33.06	51.30	18.86	14.23

Table 20. Size-by-size proximate analysis (dry basis) of minus 100 mesh Illinois No. 6 coal.

Size Class (mesh)	% Ash	% Sulfur	% Volatile Matter	% Fixed Carbon	% MM (Parr)	% MM (I.A.)
65 x 100	44.67	5.04	25.02	30.31	51.02	48.07
100 x 150	35.85	5.46	27.81	36.34	41.72	45.51
150 x 200	34.31	5.41	28.03	37.66	40.03	39.02
200 x 270	33.82	5.94	28.22	37.96	39.79	39.24
270 x 400	35.92	6.12	27.11	36.97	42.16	37.75
-400	57.56	3.91	19.29	23.15	64.32	42.80

Table 21. Size-by-size proximate analysis (dry basis) of minus 100 mesh Upper Freeport coal.

Size Class (mesh)	% Ash	% Sulfur	% Volatile Matter	% Fixed Carbon	% MM (Parr)	% MM (I.A.)
65 x 100	27.83	3.90	32.22	39.95	32.20	25.03
100 x 150	21.57	4.09	33.29	45.14	25.55	26.68
150 x 200	19.07	4.62	33.82	47.11	23.14	33.08
200 x 270	17.90	5.00	33.68	48.42	22.08	23.99
270 x 400	17.64	5.49	32.93	49.43	22.07	27.68
-400	24.61	4.90	28.71	46.68	29.27	28.56

Table 22. Overall proximate analysis (dry basis) of Pittsburgh No. 8 coal.

Sample	% Ash	% Sulfur	% Volatile Matter	% Fixed Carbon	% MM (Parr)	% MM (I.A.)
ROM	13.59	3.60	34.43	51.98	16.66	—
28 mesh x 0	13.28	3.98	36.89	49.83	16.53	15.63
100 mesh x 0	12.38	3.70	35.91	51.71	15.41	12.93
400 mesh x 0	13.04	3.45	34.68	52.28	15.98	—

Table 23. Overall proximate analysis (dry basis) of Illinois No. 6 coal.

Sample	% Ash	% Sulfur	% Volatile Matter	% Fixed Carbon	% MM (Parr)	% MM (I.A.)
ROM	48.49	4.23	22.00	29.51	54.70	—
28 mesh x 0	43.23	5.14	24.74	32.03	49.52	46.45
100 mesh x 0	44.39	4.95	24.35	31.26	50.66	42.28
400 mesh x 0	45.67	4.94	23.62	30.71	52.04	—

Table 24. Overall proximate analysis (dry basis) of Upper Freeport coal.

Sample	% Ash	% Sulfur	% Volatile Matter	% Fixed Carbon	% MM (Parr)	% MM (I.A.)
ROM	21.25	5.06	31.24	47.51	25.73	—
28 mesh x 0	21.76	4.72	32.19	46.05	26.10	25.34
100 mesh x 0	21.90	4.74	31.52	46.58	26.26	28.08
400 mesh x 0	21.11	4.63	31.02	47.87	25.35	—

Based on the data collected from the image analysis procedure, liberation spectra were plotted for the minus 28 mesh and minus 100 mesh samples of each coal type. The liberation spectra represent the weight percent material present in a given composition class and are shown in Figures 26-31. As shown, the Pittsburgh No. 8 sample, which has the lowest ash content, contains the highest percentage of free or nearly free carbonaceous material. For the minus 28 mesh Pittsburgh No. 8 sample (Figure 26), the percentage of particles containing greater than 90% carbonaceous material is approximately 80%. This number increases slightly to 85% for the minus 100 mesh sample (Figure 27). The Illinois No. 6 sample, on the other hand, contains the highest percentage of free or nearly free mineral matter. As a result, the percentage of particles containing greater than 90% carbonaceous material is reduced to approximately 45% for the minus 28 mesh sample (Figure 28) and 50% for the minus 100 mesh sample (Figure 29). The Upper Freeport sample, which has an ash content intermediate to the Illinois No. 6 and Pittsburgh No. 8 samples, appears to contain a higher percentage of middlings, especially in the 60% to 90% carbonaceous-material range, than either of the other two coals. At the same time, the amount of free or nearly free carbonaceous material is intermediate to the other two coals at approximately 60% for both the minus 28 and minus 100 mesh samples (Figures 30 and 31).

In order to relate the liberation spectra to coal cleaning, it is important to understand the implications of these spectra. For example, it is expected that it should be relatively easy to reject mineral matter in the Pittsburgh No. 8 coal since this sample contains a large percentage of free or nearly free carbonaceous material. As shown in Figures 14 and 20, this is clearly the case since the image analysis separation curves show a pronounced "elbow" in the upper right corner of these plots. On the other hand, the Illinois No. 6 sample, which has the lowest percentage of free carbonaceous material, has the highest percentage of free mineral matter, i.e., rock. Since "rock" can be easily rejected without affecting the recovery of carbonaceous material, it is expected that the image analysis

separation curve for the Illinois No. 6 sample should be similar to that for the Pittsburgh No. 8, although mineral matter rejection should be slightly worse since the Illinois No. 6 sample contains a slightly higher percentage of middlings. This is also the case as shown in Figures 16 and 22. Finally, the Upper Freeport sample should give the poorest separation curve since nearly all of the mineral matter in this sample is associated with middlings particles. This result can be seen by examining the image analysis separation curves shown in Figures 18 and 24. Thus, a careful examination of the liberation spectra can provide useful information related to the cleanability of a given coal sample.

In a similar manner, it is possible to present the liberation data in terms of pyrite rejection. Figures 32-37 show the pyrite liberation spectra for each of the three coal samples studied in this work. As shown, the Pittsburgh No. 8 and Upper Freeport samples exhibit relatively little pyrite liberation at the minus 28 mesh size (Figures 32 and 36); however, the degree of liberation increases significantly as these coals are reduced to minus 100 mesh (Figures 33 and 37). On the other hand, the Illinois No. 6 sample appears to exhibit some pyrite liberation even at the minus 28 mesh size, as illustrated by the U-shaped curve (Figure 34). The degree of liberation increases slightly for the minus 100 mesh sample (Figure 35), but the increase is not as great as that observed for the Pittsburgh No. 8 and Upper Freeport samples. These results tend to indicate that the Pittsburgh No. 8 and Upper Freeport coals contain fine pyrite which can be substantially liberated by reducing the top size of the material to 100 mesh. The Illinois No. 6 coal, on the other hand, appears to contain a bimodal distribution of pyrite. The coarse pyrite is already partially liberated at a top size of 28 mesh, while the fine pyrite remains substantially locked even at a top size of 100 mesh.

In relating the pyrite liberation spectra to the image analysis separation curves (Figures 15, 17, 19, 21, 23 and 25), it is important to understand the behavior of those particles containing finely disseminated pyrite (e.g., particles containing less than 20 area % pyrite), since it is these particles that

cause the drop off in carbonaceous recovery at high values of pyrite rejection. Figures 32, 34 and 36 show that for the minus 28 mesh size, the amount of finely disseminated pyrite is greatest for the Upper Freeport sample, followed by the Illinois No. 6 sample and the Pittsburgh No. 8 sample. Based on these data, it is expected that the Pittsburgh No. 8 coal should exhibit the best pyrite rejection curve, followed by the Illinois No. 6 and Upper Freeport coals. This is exactly the trend shown in Figures 15, 17 and 19. At the minus 100 mesh size, the Illinois No. 6 and Upper Freeport coals reverse order since the Upper Freeport coal becomes more liberated while the Illinois No. 6 coal contains a greater amount of finely disseminated pyrite (see Figures 21, 23 and 25).

Perhaps of most importance in the present work is the pyrite which is free or nearly free since it is this material which must be depressed by electrochemical or polymeric means. In order to get a better handle on this portion of the liberation spectrum, the size of the carbonaceous inclusions contained in each pyrite particle was measured, and the amount of pyrite present with a maximum carbonaceous inclusion less than some stated size was plotted in cumulative form as shown in Figures 38 - 43. If it is assumed that a hydrophilic polymeric chain can be used to cover a 10 micron carbonaceous inclusion, then it is possible to read the y-axis at this inclusion size and determine how much pyrite could potentially be rejected by the polymeric depressant, assuming all of this pyrite floats in the absence of the depressant. Likewise, if the amount of free or nearly free pyrite present in the sample is desired, one simply reads the intersection of the y-axis at an inclusion size of 1 micron.

As shown in Figures 38, 40 and 42, none of the coal samples contain a large amount of free or nearly free pyrite at the minus 28 mesh size. The Illinois No. 6 sample appears to contain the most of this material with 35% of the pyrite contained in particles having carbonaceous inclusions of 10 microns or less. On the other hand, the amount of free or nearly free pyrite increases substantially when the top size is reduced to 100 mesh. Figures 39, 41 and 43 show that the Pittsburgh No. 8

sample increases from about 18% pyrite with carbonaceous inclusions smaller than 10 microns at minus 28 mesh to approximately 70% at minus 100 mesh. Similarly, the Illinois No. 6 sample increases from 35% to 57%, while the Upper Freeport sample increases from 23% to 60%. Based on this result, it is expected that the 100 mesh x 0 Pittsburgh No. 8 sample should have the greatest potential for responding to a polymeric depressant.

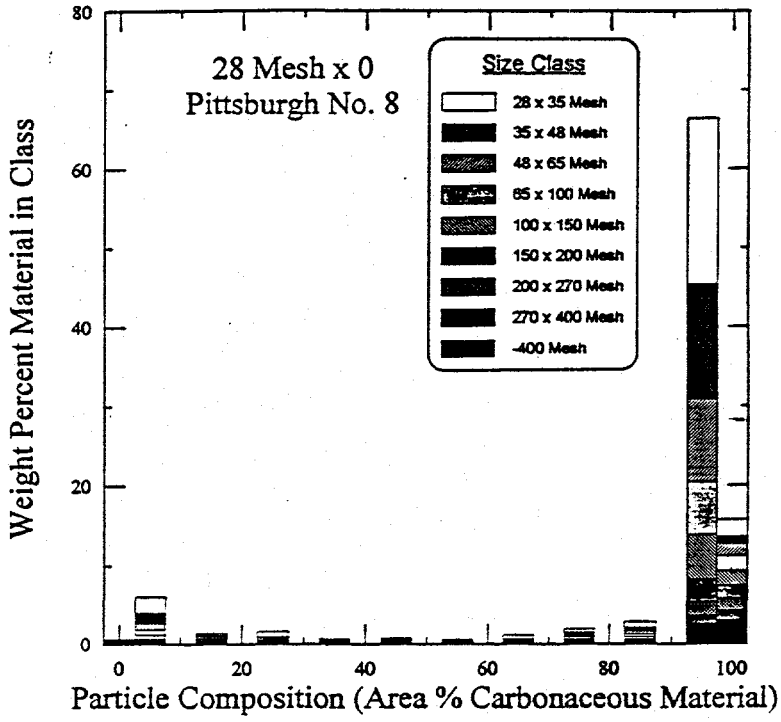

Figure 26. Liberation spectrum for minus 28 mesh Pittsburgh No. 8 coal.

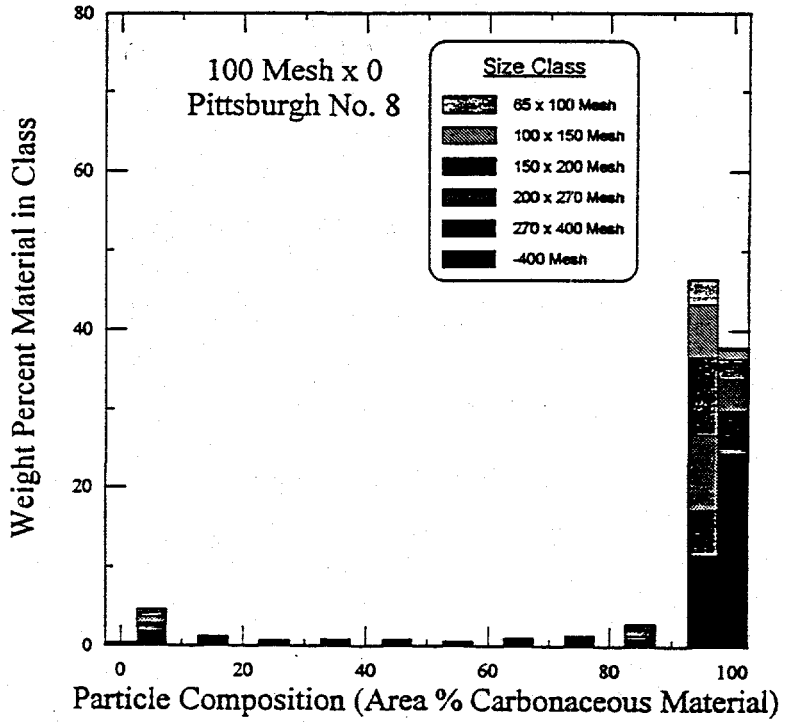

Figure 27. Liberation spectrum for minus 100 mesh Pittsburgh No. 8 coal.

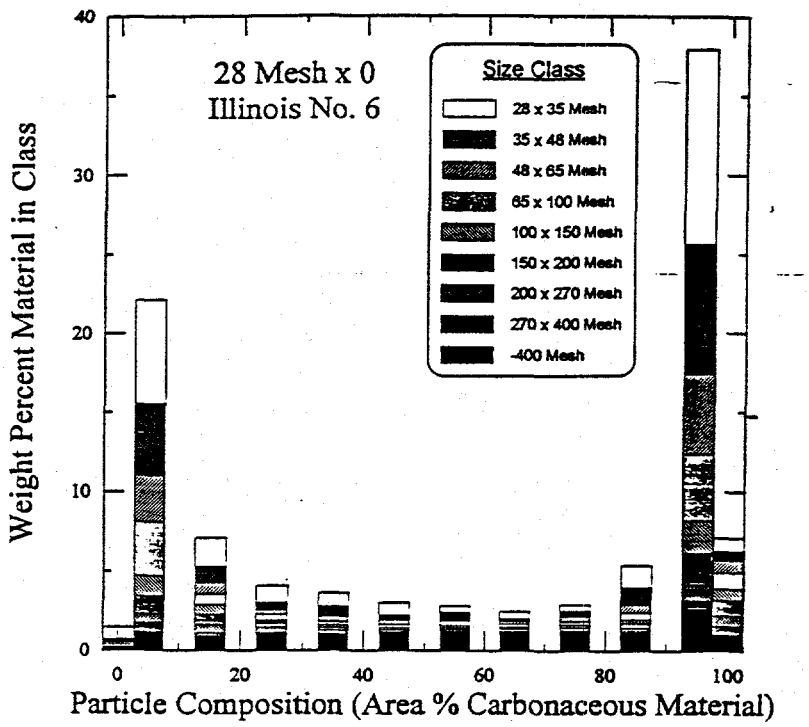

Figure 28. Liberation spectrum for minus 28 mesh Illinois No. 6 coal.

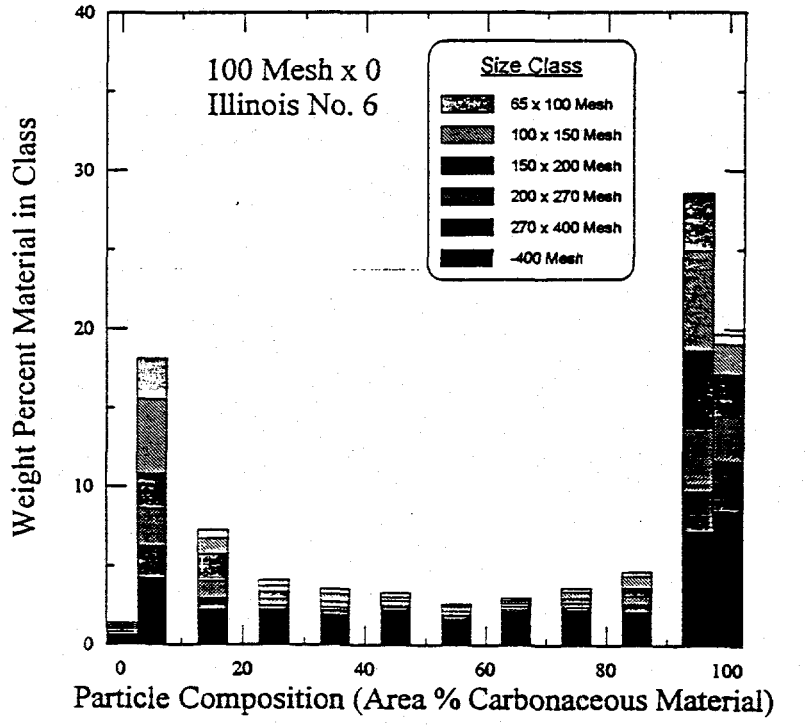

Figure 29. Liberation spectrum for minus 100 mesh Illinois No. 6 coal.

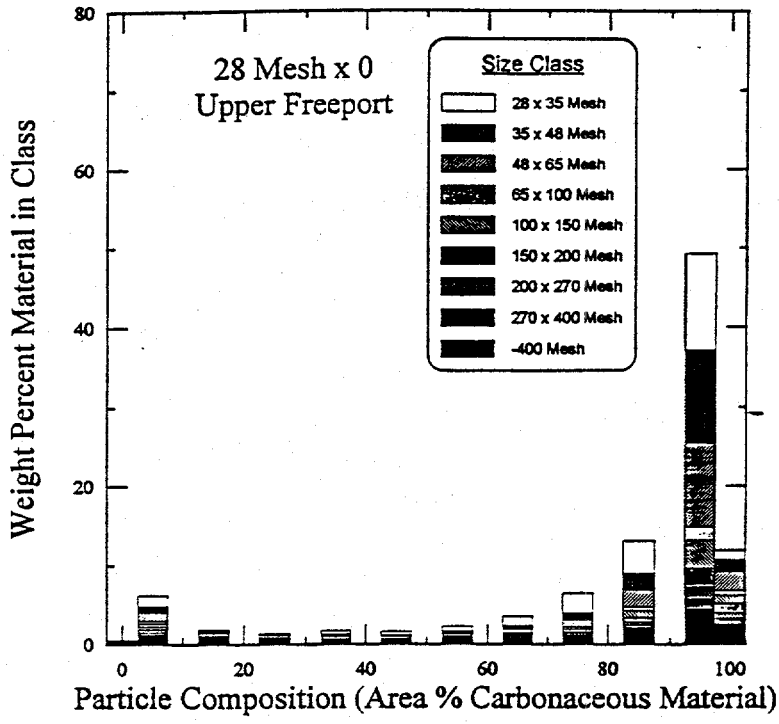

Figure 30. Liberation spectrum for minus 28 mesh Upper Freeport coal.

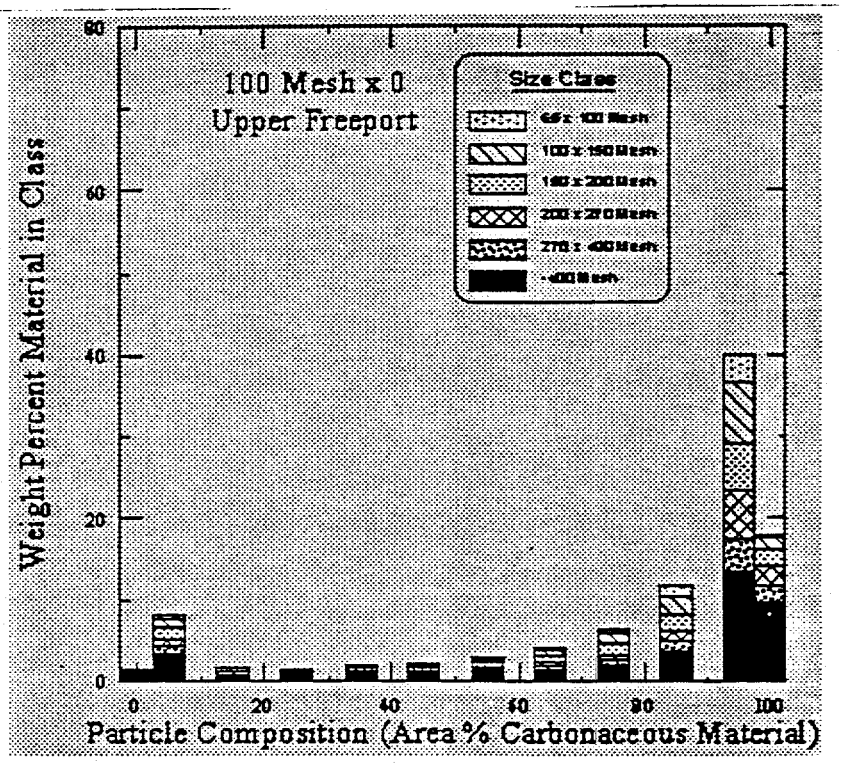

Figure 31. Liberation spectrum for minus 100 mesh Upper Freeport coal.

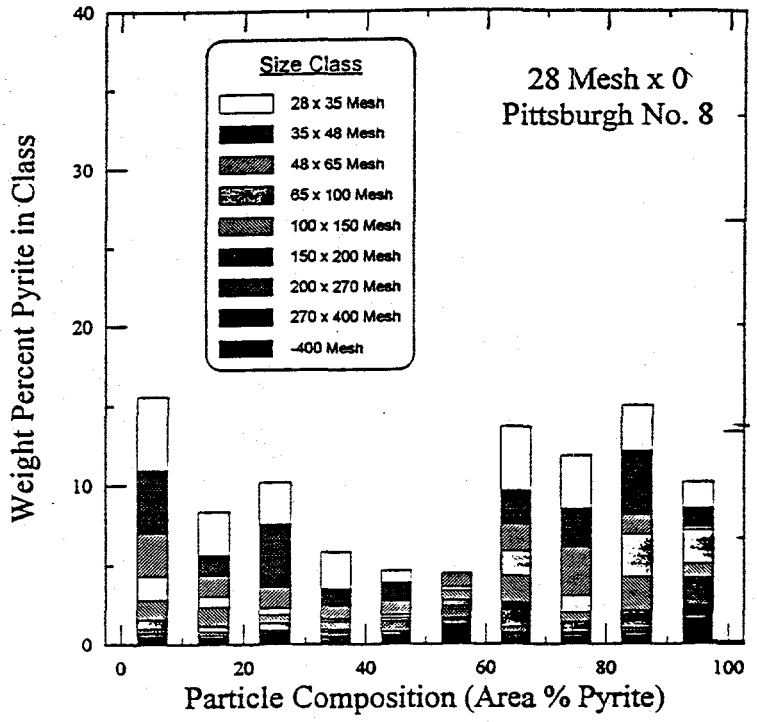

Figure 32. Pyrite liberation spectrum for minus 28 mesh Pittsburgh No. 8 coal.

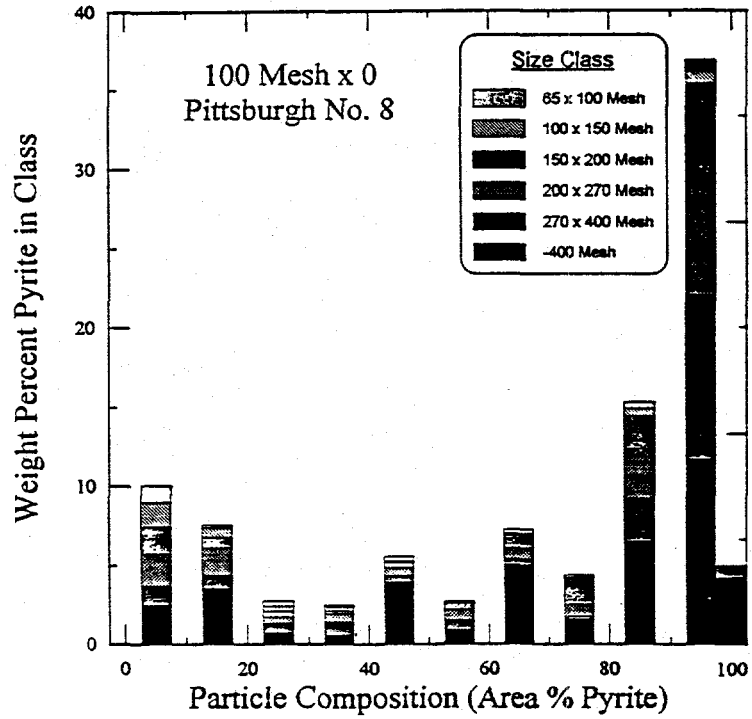

Figure 33. Pyrite liberation spectrum for minus 100 mesh Pittsburgh No. 8 coal.

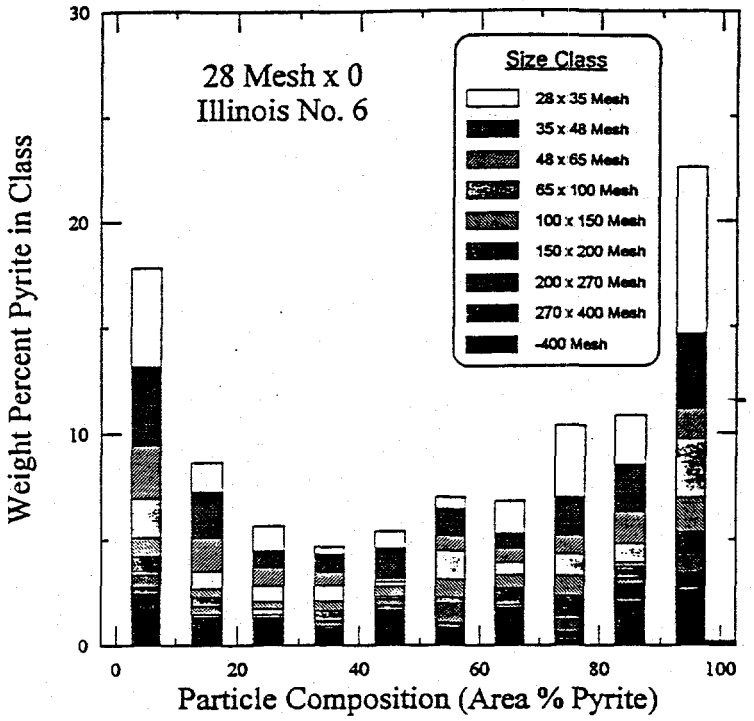

Figure 34. Pyrite liberation spectrum for minus 28 mesh Illinois No. 6 coal.

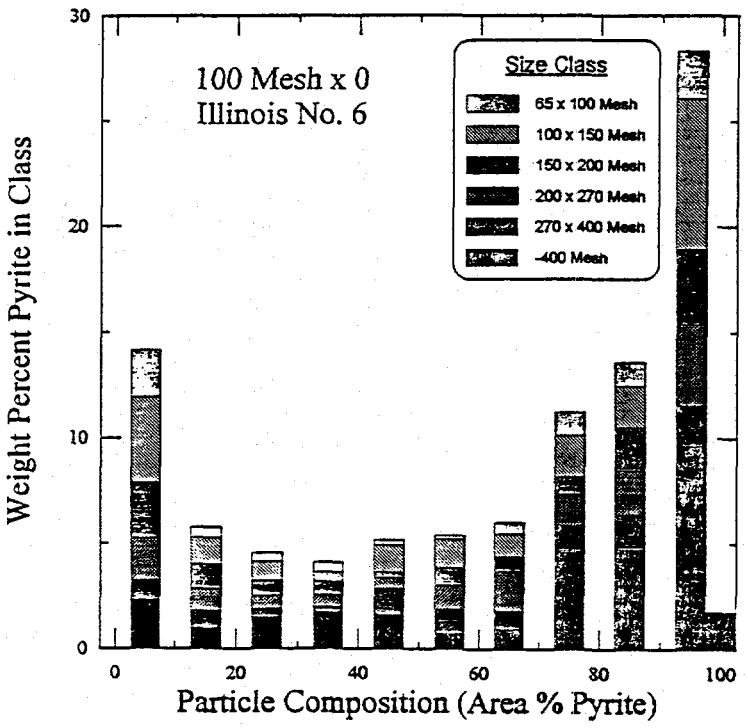

Figure 35. Pyrite liberation spectrum for minus 100 mesh Illinois No. 6 coal.

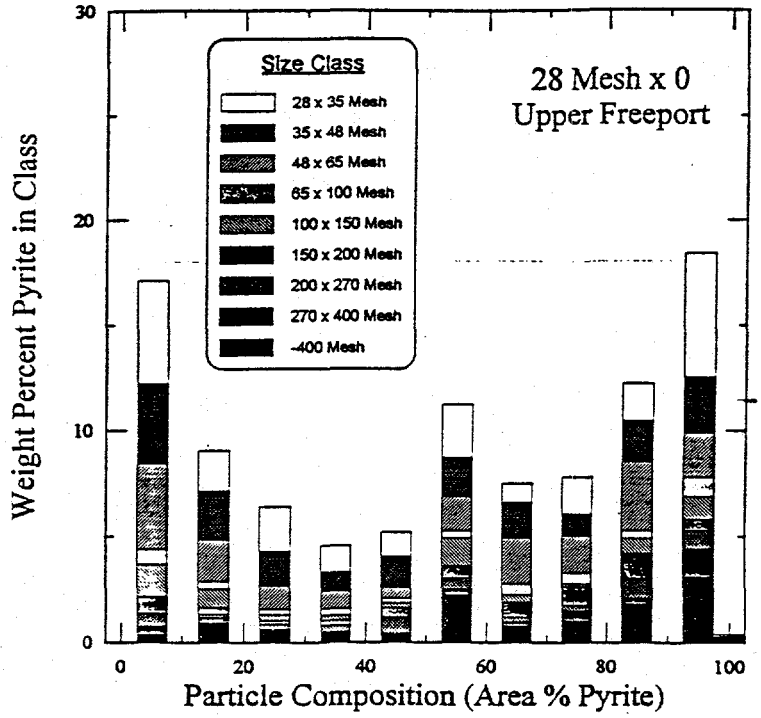

Figure 36. Pyrite liberation spectrum for minus 28 mesh Upper Freeport coal.

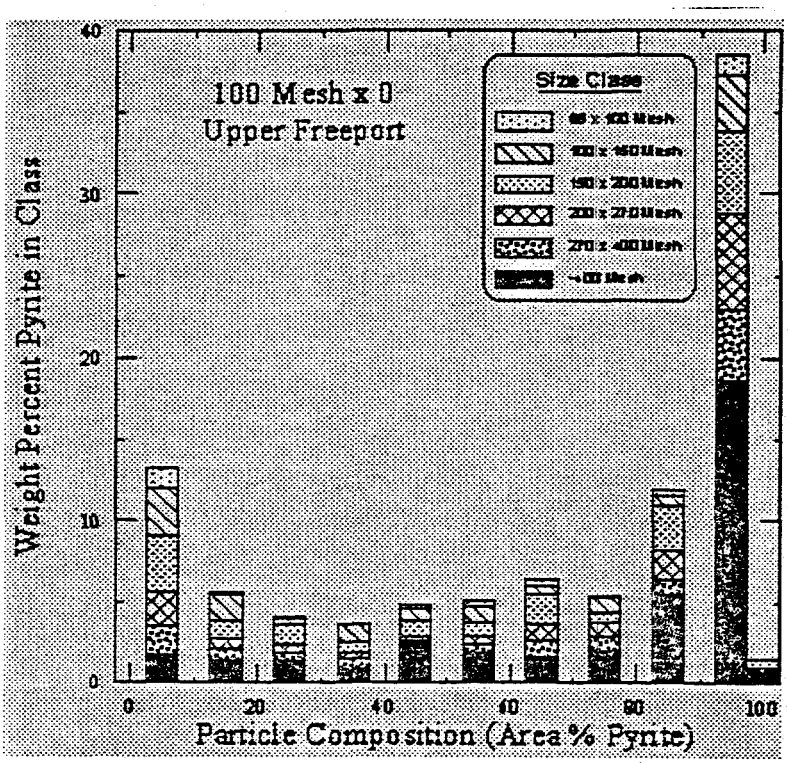

Figure 37. Pyrite liberation spectrum for minus 100 mesh Upper Freeport coal.

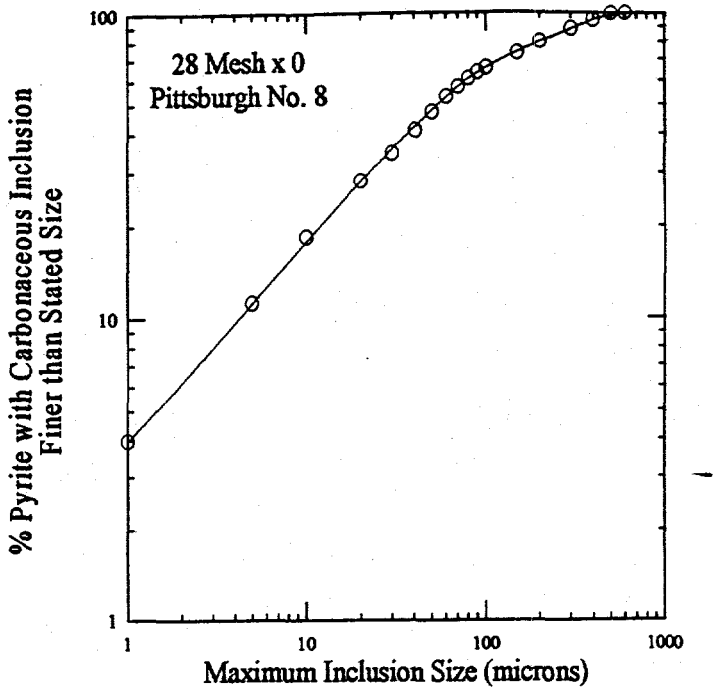

Figure 38. Weight percent pyrite containing carbonaceous inclusions finer than a given size for minus 28 mesh Pittsburgh No. 8 coal.

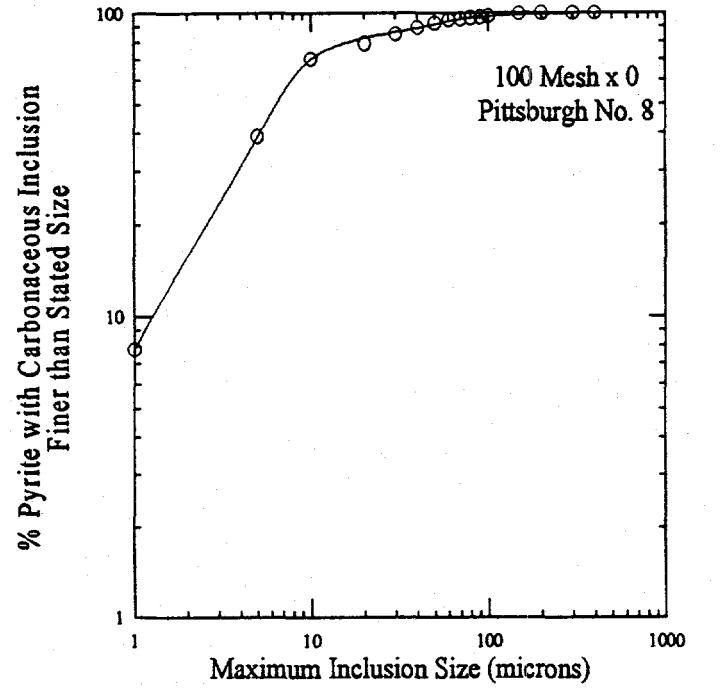

Figure 39. Weight percent pyrite containing carbonaceous inclusions finer than a given size for minus 100 mesh Pittsburgh No. 8 coal.

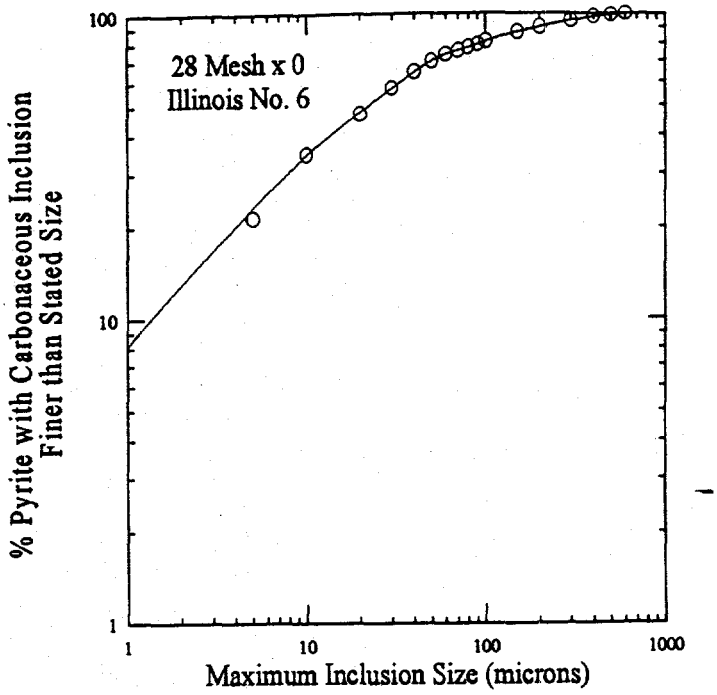

Figure 40. Weight percent pyrite containing carbonaceous inclusions finer than a given size for minus 28 mesh Illinois No. 6 coal.

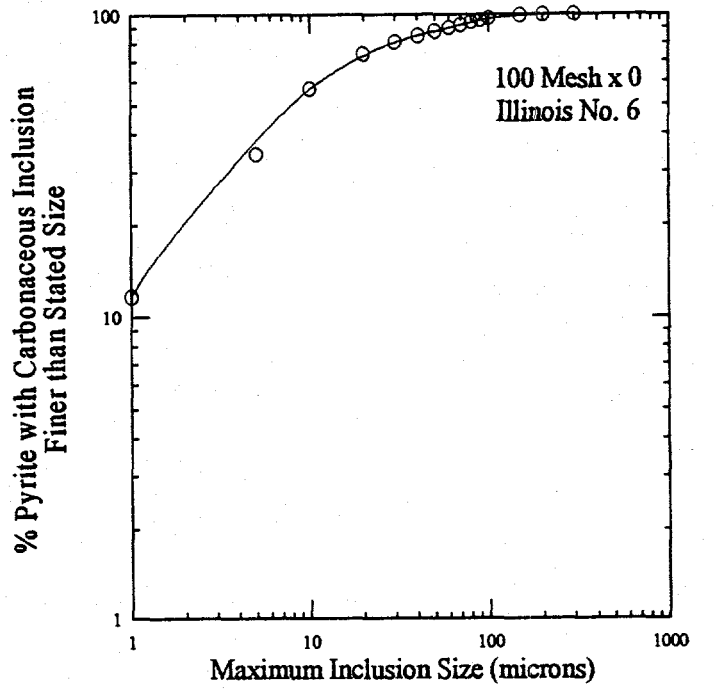

Figure 41. Weight percent pyrite containing carbonaceous inclusions finer than a given size for minus 100 mesh Illinois No. 6 coal.

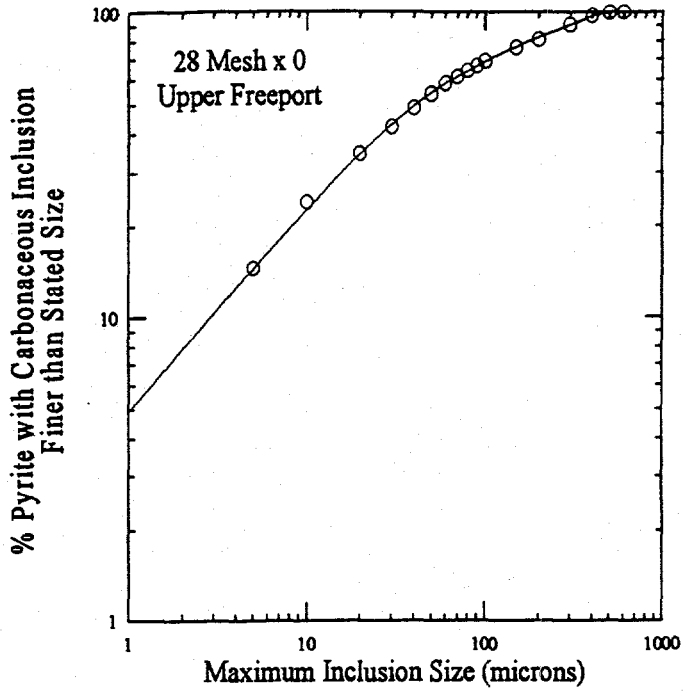

Figure 42. Weight percent pyrite containing carbonaceous inclusions finer than a given size for minus 28 mesh Upper Freeport coal.

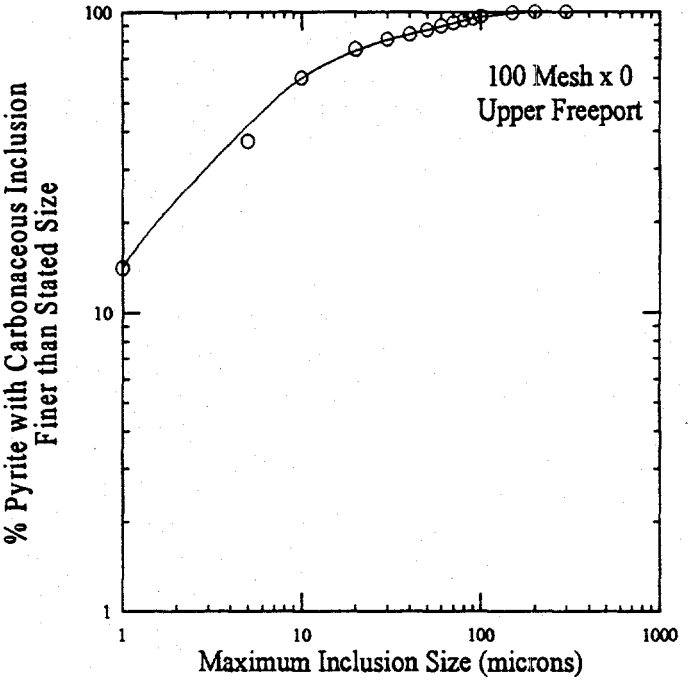

Figure 43. Weight percent pyrite containing carbonaceous inclusions finer than a given size for minus 100 mesh Upper Freeport coal.

Subtask 2.3: SEM-IPS Analysis of Flotation Products

The purpose of this subtask was to use the SEM-IPS system to analyze the flotation products obtained from the best EESR and PESR tests (See Tasks 5 and 6 for details). Since the original flotation test work was limited to the minus 100 mesh Illinois No. 6 and Pittsburgh No. 8 samples, only results from these coals are presented here.

Three tests from Tasks 5 and 6 were selected to represent the "best" performance. In the case of the Pittsburgh No. 8 coal, both an EESR and a PESR test were selected to represent the best of each of the two processes, while in the case of the Illinois No. 6 coal, a combination of the EESR and PESR processes was found to give the best result. The clean coal products from each of these three tests were screened into size fractions for analysis. These size distributions are shown in Tables 25 - 27.

Table 25. Size distribution for a clean coal product obtained using a combination of EESR and PESR on minus 100 mesh Illinois No. 6 coal (Overall Yield = 57.64%).

Size Class (Mesh)	Wt. % in Class
+150	41.74
150 x 200	17.41
200 x 270	13.94
270 x 400	10.30
-400	16.61

Table 26. Size distribution for a clean coal product obtained using EESR on minus 100 mesh Pittsburgh No. 8 coal (Overall Yield = 68.88%).

Size Class (Mesh)	Wt. % in Class
+150	38.21
150 x 200	16.17
200 x 270	13.48
270 x 400	9.60
-400	22.54

Table 27. Size distribution for a clean coal product obtained using PESR on minus 100 mesh Pittsburgh No. 8 coal (Overall Yield = 57.68%).

Size Class (Mesh)	Wt. % in Class
+150	52.49
150 x 200	13.98
200 x 270	10.50
270 x 400	8.57
-400	14.45

Following the sizing of each of the three clean coal products, a single size fraction from each product was mounted and polished for viewing under the SEM. In the original work plan, the size fraction showing the largest sulfur rejection was to be used in the SEM-IPS analysis; however, sulfur forms analyses were not possible due to the small amount of material present in each size fraction. Therefore, the 270 x 400 mesh size fraction was selected based on the fact that the particle size was small enough to have a significant amount of free or nearly free pyrite present, while the size was not so small that the image analysis results would be unreliable.

The results obtained for the combined EESR/PESR processing of the Illinois No. 6 sample are shown in Figures 44 and 45. As shown in Figure 44, the composition of the 270 x 400 mesh Illinois No. 6 sample shifts largely to particles of free or nearly free carbonaceous material after processing. This is generally what one would expect for any clean coal product. Of more significance, however, is the fact that the free pyrite and nearly free pyrite particles are totally eliminated from the clean coal product (Figure 45). In fact, all particles containing greater than 80% pyrite have been eliminated, even though nearly 35% of the pyrite in the original feed material was present in these types of particles. The pyrite remaining in the clean coal product is primarily in a finely disseminated form which is impossible to eliminate without significant losses in combustible recovery.

primarily in a finely disseminated form which is impossible to eliminate without significant losses in combustible recovery.

The trends appear to be similar for the Pittsburgh No. 8 sample (Figures 46 - 49) although the nearly liberated pyrite seems to be much more difficult to reject in this case. As shown in Figures 46 and 48, both the EESR and PESR processes cause a shift in the clean coal composition to particles of free or nearly free carbonaceous material. Furthermore, both processes appear to reject all free pyrite (Figures 47 and 49). Unfortunately, the rejection of particles containing greater than 90% pyrite is not as good as that obtained with the Illinois No. 6.

One possible explanation for the different behavior of the Illinois No. 6 and the Pittsburgh No. 8 samples is as follows. Pittsburgh No. 8 coal is generally considered easier to float (i.e., more hydrophobic) than Illinois No. 6 coal. As a result, a small amount of carbonaceous material contained in a pyrite particle may be more likely to cause flotation in Pittsburgh No. 8 coal than is the case with the Illinois No. 6 sample. This hypothesis appears to be supported by the data when one looks at mass yield as a function of particle composition (Figure 50). As shown, yield is nearly independent of particle composition for the Pittsburgh No. 8 coal until the particles become almost entirely pyrite. This would tend to indicate that the floatability of the carbonaceous portion of the Pittsburgh No. 8 coal is so great that it tends to overwhelm the pyrite present in a given particle. On the other hand, yield is a strong function of particle composition for the Illinois No. 6 sample. In this case, the lower floatability of the carbonaceous material makes it easier to reject the nearly liberated pyrite particles. This would suggest that the EESR and PESR techniques may have a bigger impact on more difficult to float coals such as Illinois No. 6.

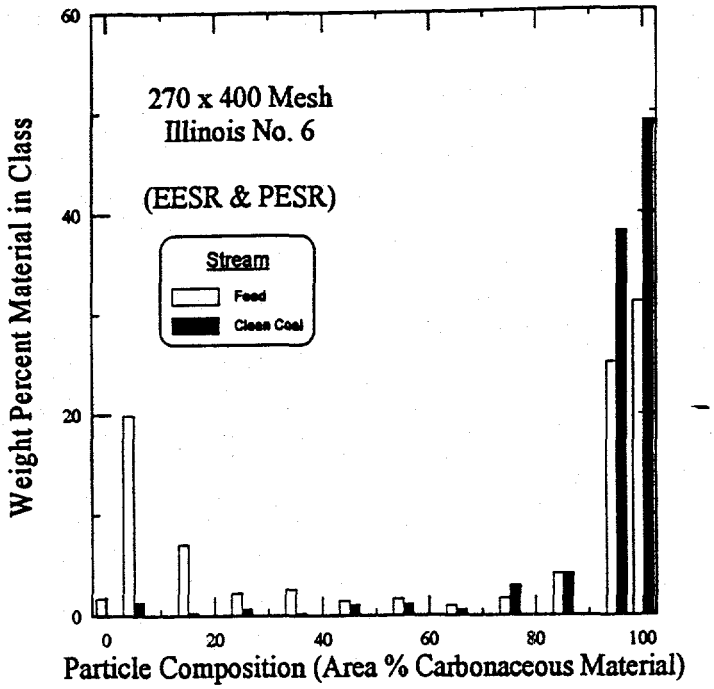

Figure 44. Comparison of feed and clean coal liberation spectra for 270 x 400 mesh Illinois No. 6 coal treated by a combination of the PESR and EESR processes.

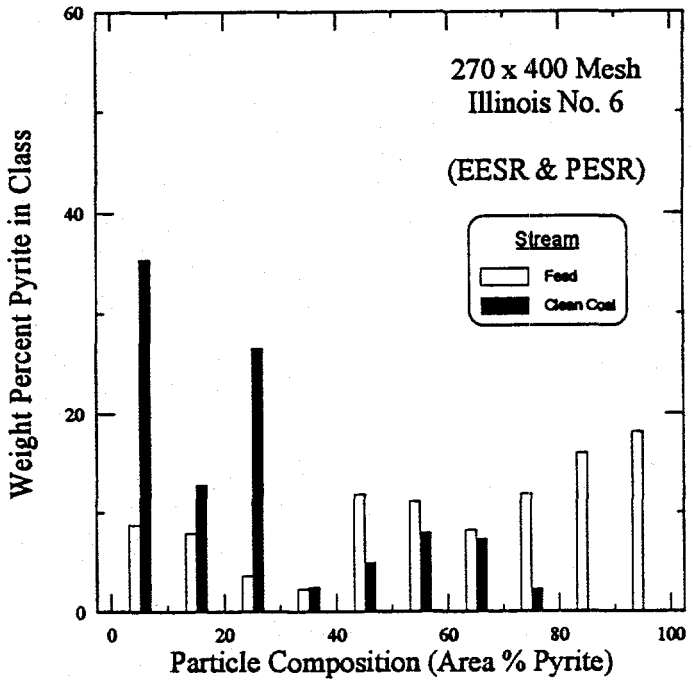

Figure 45. Comparison of feed and clean coal pyrite liberation spectra for 270 x 400 mesh Illinois No. 6 coal treated by a combination of the PESR and EESR processes.

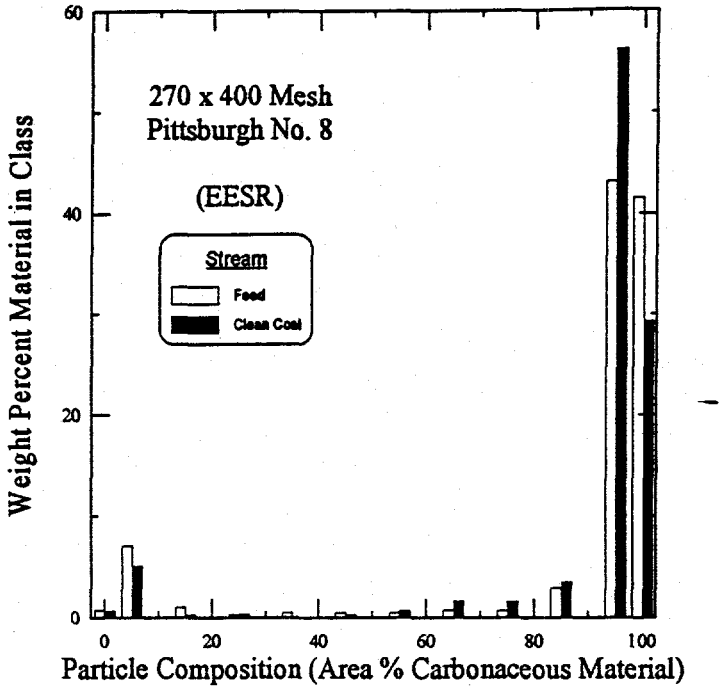

Figure 46. Comparison of feed and clean coal liberation spectra for 270 x 400 mesh Pittsburgh No. 8 coal treated by the EESR process.

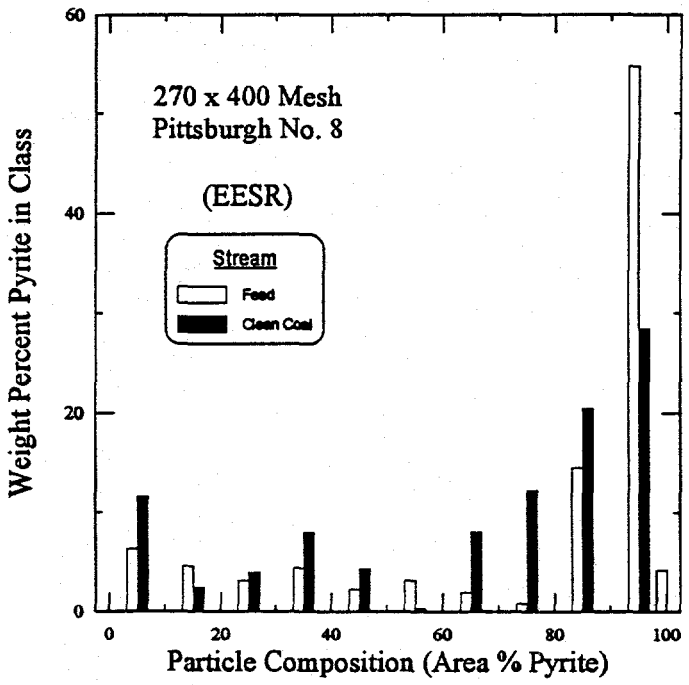

Figure 47. Comparison of feed and clean coal pyrite liberation spectra for 270 x 400 mesh Pittsburgh No. 8 coal treated by the EESR process.

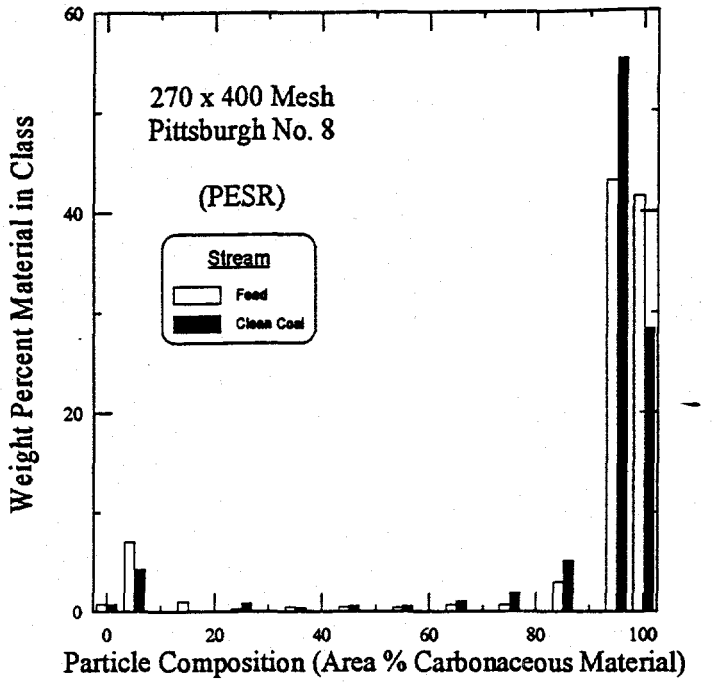

Figure 48. Comparison of feed and clean coal liberation spectra for 270 x 400 mesh Pittsburgh No. 8 coal treated by the PESR process.

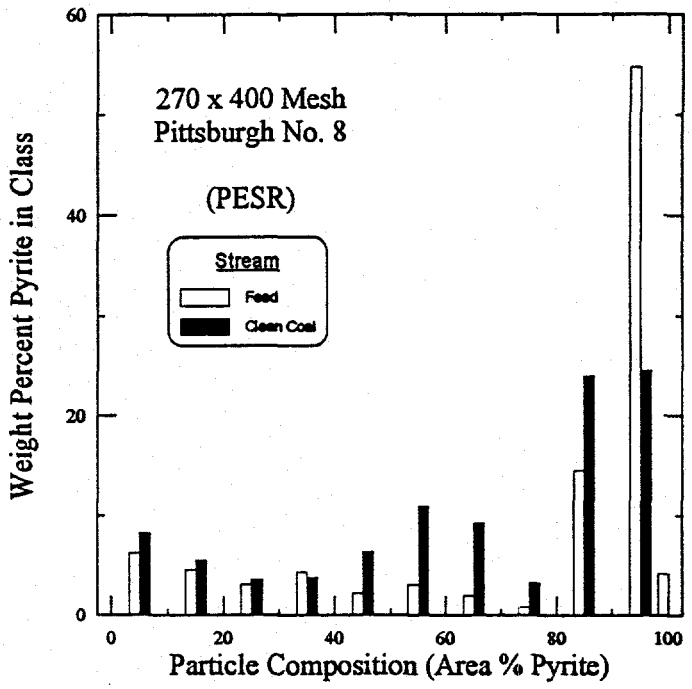

Figure 49. Comparison of feed and clean coal pyrite liberation spectra for 270 x 400 mesh Pittsburgh No. 8 coal treated by the PESR process.

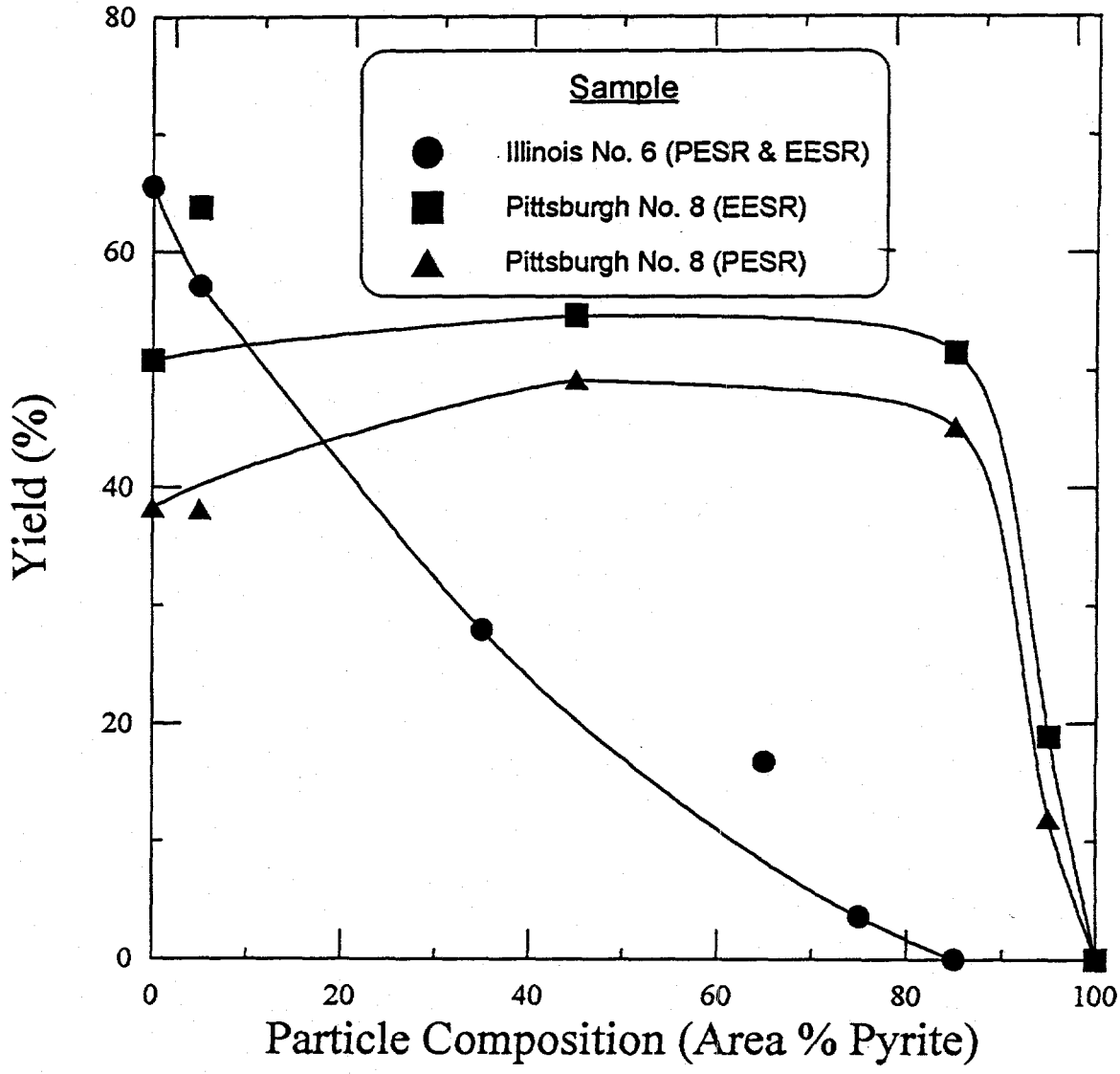

Figure 50. Yield as a function of particle composition for the three "best" EESR and PESR tests.

Task 3 - Electrochemical Studies

Subtask 3.1: Linear Voltammetric Sweeps

Oxygen reduction on rotating ring-disc electrodes of pyrite: The oxidation of sulfide minerals, including that of pyrite, is controlled by mixed potential, corrosion-type electrochemical reactions, in which the mineral undergoes anodic oxidation while oxygen is cathodically reduced. Oxygen serves as an electron scavenger and the kinetics of its reduction is important in determining the rate of pyrite oxidation and the mixed potential at which it occurs.

Studies of oxygen reduction on pyrite electrodes were conducted with the RRDE. Figure 51 (top) shows the current resulting from linear potential sweeps from 0.25 to -0.75 V on the Chinese coal-pyrite disc electrode at pH 9.2 for various rotation speeds in a solution saturated with oxygen; Figure 51 (bottom) shows the resulting ring currents. The current was negligible in the absence of oxygen in this potential range. At the beginning of the sweeps, the current is controlled by electron transfer (activation control) and is only slightly dependent on rotation rate, ω. As the potential becomes more negative, the diffusion of oxygen to the disc surface gradually limits the reaction rate and, hence, the current is increasingly dependent on rotation speed. At more negative potentials, the current is diffusion-limited. The onset of the diffusion-limited current shifts to more negative potentials with increasing rotation speed. The limiting current, i_L (mA/cm^2), is given by the Levich Equation (1) (Greef et al., 1985),

$$i_L = 0.62\, nFD^{2/3} \nu^{-1/6} C_b \omega^{1/2}, \qquad (1)$$

where n is the number of electrons in the overall reaction, F the Faraday's constant, D the diffusion coefficient for the relevant species undergoing oxidation or reduction, ν the kinematic viscosity, C_b the concentration of the electroactive species in the bulk solution, and ω is the angular velocity of the

electrode. According to Biegler et al. (1975), $D = 1.93\times10^{-5}$ cm^2/sec, $\nu = 0.941\times10^{-3}$ cm^2/sec and $C_b = 1.21\times10^{-6}$ mole/cm^3 for oxygen. Substituting these values and other relevant constants into Equation (1), one obtains,

$$I_L = 0.0457n\omega^{1/2}, \quad (2)$$

where I_L is in units of mA. A plot of I_L vs. $\omega^{1/2}$, as shown in Figure 52, is linear, in agreement with Equation (2). The value of n calculated from Equation (2) is 3.5, suggesting that the reduction of oxygen proceeds to OH^- primarily by the 4-electron process,

$$O_2 + 2H_2O + 4e^- = 4OH^- \ (E = 1.229 - 0.059pH). \quad (3)$$

The presence of a single wave on the disc during linear sweeps indicates that no intermediate soluble species is generated during oxygen reduction at pH 9.2. This is substantiated by the absence of a ring current from 0.25 to -0.55 V when the ring was held at 0.25 V, which is positive enough to oxidize any hydrogen peroxide (H_2O_2) produced on the disc. The small ring current observed at potentials < -0.55 V is due to the cathodic decomposition of pyrite and will be discussed later.

The reaction order with respect to O_2 can be determined from the slope of the plot of log I vs. log $(1 - I/I_L)$, as shown in Equation (4) (Babic and Metikos-Hukovic, 1993):

$$\log I = \log I_k + m \log (I - I/I_L) \quad (4)$$

where I_k is the kinetic current density and m is the reaction order with respect to dissolved oxygen molecules. The values of current I at all rotation rates were chosen at -0.2 V and -0.25 V for the plot of log I against log $(1 - I/I_L)$. The results are shown in Figure 53. The slopes are found to be 0.9372 and 0.9515, respectively, indicating that oxygen reduction on pyrite at pH 9.2 is a first order reaction. This is in agreement with Biegler et al.'s conclusion (Biegler et al., 1975) that the formation of O_2 is the rate determining step.

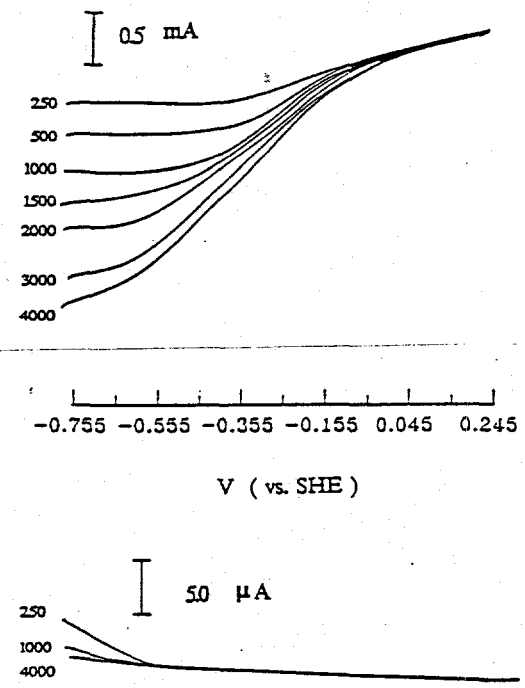

Figure 51. Ring-disc linear sweep current for oxygen reduction on Chinese coal-pyrite at pH 9.2 (ring at 0.25 V).

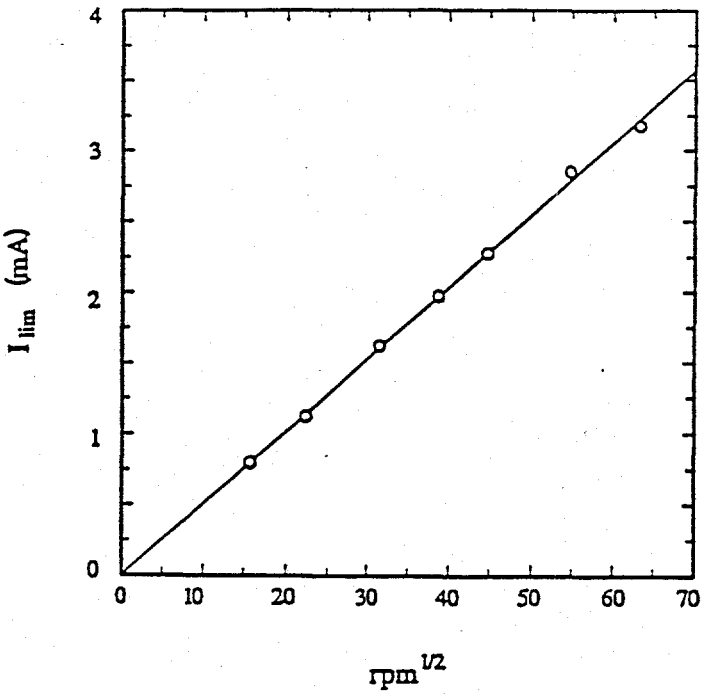

Figure 52. Limiting current of oxygen reduction as a function of electrode rotation speed on Chinese coal-pyrite at pH 9.2.

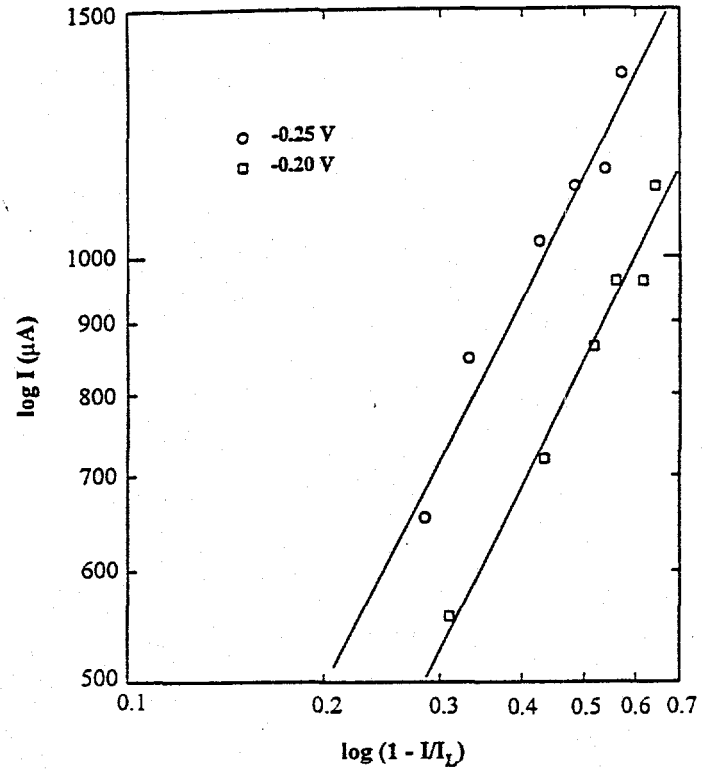

Figure 53. Dependence log I on log (1 - I/IL) for oxygen reduction on Chinese coal-pyrite at -0.2 V and -0.25 V at pH 9.2.

The results shown in Figure 51 can be expressed in Equation (5) (Babic and Metikos-Hukovic, 1993):

$$\log\frac{II_L}{I_L - I} = Constant + logC_b - \frac{\alpha nF}{2.3RT}E \qquad (5)$$

Tafel slopes at different electrode rotation speeds can be determined from the plot of E against log $[II_L/(I_L - I)]$. In all cases, a straight line was observed over one or two decades of current with an average slope of 0.224 V/dec, as shown in Figure 54.

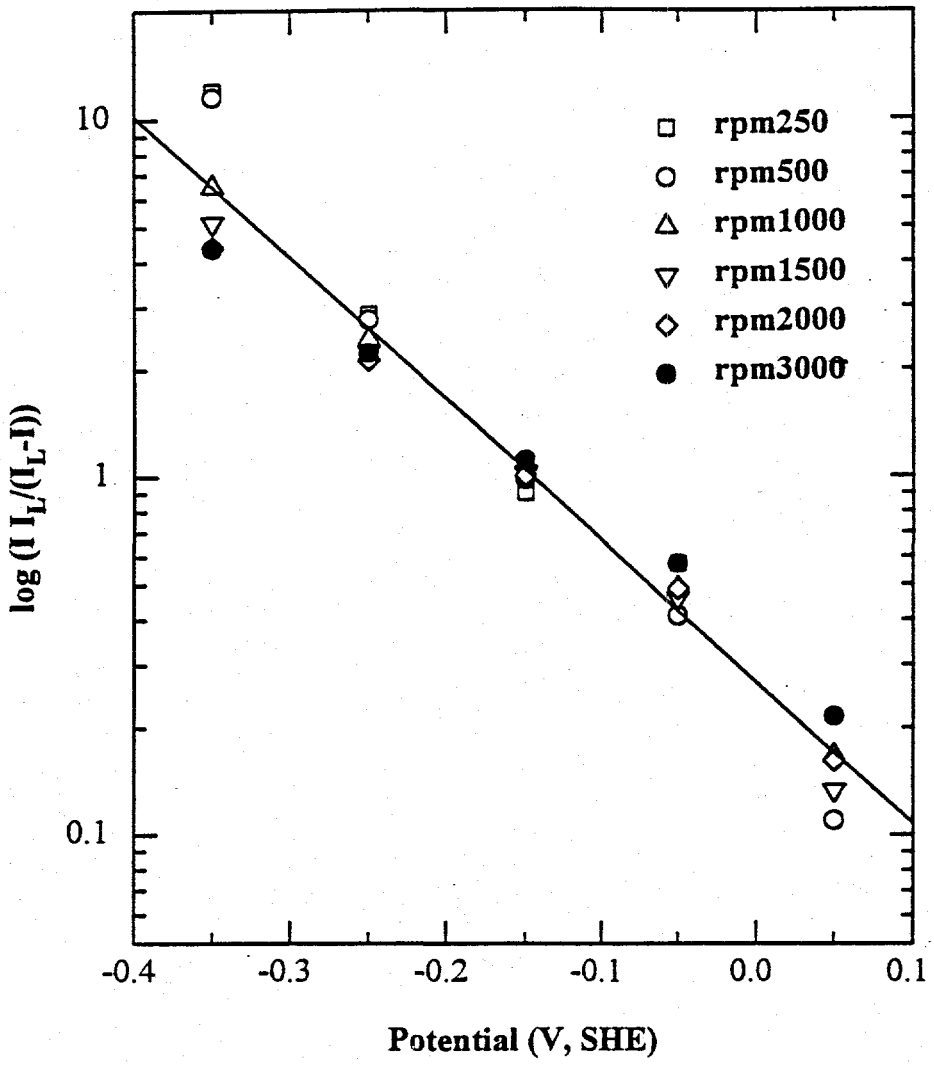

Figure 54. Tafel plots for oxygen reduction on Chinese coal-pyrite at pH 9.2 at specified rotation speed in rpm.

The results of oxygen reduction on Pittsburgh No.8 coal- and mineral-pyrite were similar with regard to the shape of the disc current during linear sweeps and the resulting ring response. Mineral- and Chinese coal-pyrite electrodes showed nearly identical disc currents for oxygen reduction that were higher than those exhibited by Pittsburgh No. 8 coal-pyrite.

The disc currents during linear potential sweeps in the negative direction for oxygen reduction on Pittsburgh No. 8 coal-pyrite, Chinese coal-pyrite and mineral pyrite at pH 6.8 are shown in Figure 55. The overall features of these currents are similar to those at pH 9.2 for all three pyrite samples, with no evidence of the formation of hydrogen peroxide. The magnitude of the disc currents at identical overvoltages at pH 6.8 is in the order of Pittsburgh No. 8 coal-pyrite > Chinese coal-pyrite ≈ mineral-pyrite.

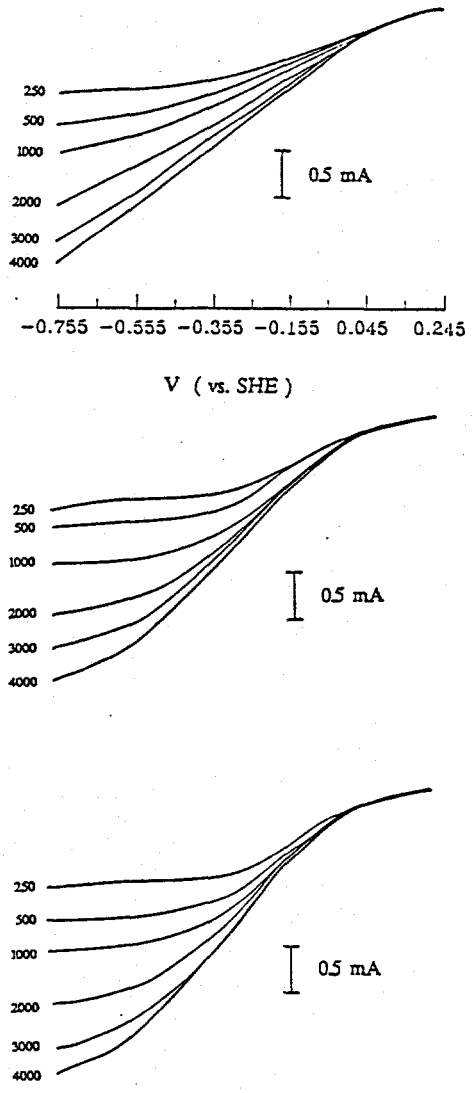

Figure 55. Disc current during potential sweep, for O_2 reduction at pH 6.8 on Pittsburgh No. 8 coal-pyrite (top); Chinese coal-pyrite (middle); mineral-pyrite (bottom) at specified rpm.

However, there are still some remarkable differences on sweeps obtained at pH 9.2 and 6.8 and these differences are sample-dependent. Oxygen reduction at pH 6.8 consistently showed a higher current than at pH 9.2 for all three pyrites. For mineral-pyrite, the diffusion-limited current was observed at lower potentials at pH 6.8 than at pH 9.2. For Chinese coal-pyrite, although the current was higher at pH 6.8 than at pH 9.2, the potential at which the diffusion-limited current was reached did not change remarkably as the solution pH decreased from 9.2 to 6.8. For Pittsburgh No. 8 coal-pyrite, the oxygen reduction current increased considerably with decreasing pH from 9.2 to 6.8, and the potential where the diffusion-limited current was reached shifted significantly, especially at higher electrode rotation rates.

In acidic solution, oxygen reduction on pyrite proceeded *via* a different route. Figure 56 shows the linear sweep voltammograms for oxygen reduction on Chinese coal-pyrite at pH 4.6. In the activation-controlled region, there are two distinct cathodic reduction processes occurring, as evidenced by the change in slope of the curves at about 0 V. The current on the ring, which was held at 0.55 V during the potential sweep, shows that a soluble intermediate species was produced at potentials < -0.15 V. This can be attributed to hydrogen peroxide produced on the disc by the reaction, followed by its re-oxidation on the ring.

$$O_2 + 2H^+ + 2e^- = H_2O_2 \quad (E = 0.695 - 0.059pH) \qquad (6)$$

The ring current reached a maximum at a disc potential of -0.25 V. When the limiting current on the disc was reached (< -0.3 V), the overpotential was large enough that hydrogen peroxide was reduced at the disc to OH^-, with less diffusing to the ring. Consequently, the ring current decreased. At more negative potentials (< -0.5 V), significant cathodic decomposition of pyrite occurred, producing decomposition products which were oxidized at the ring.

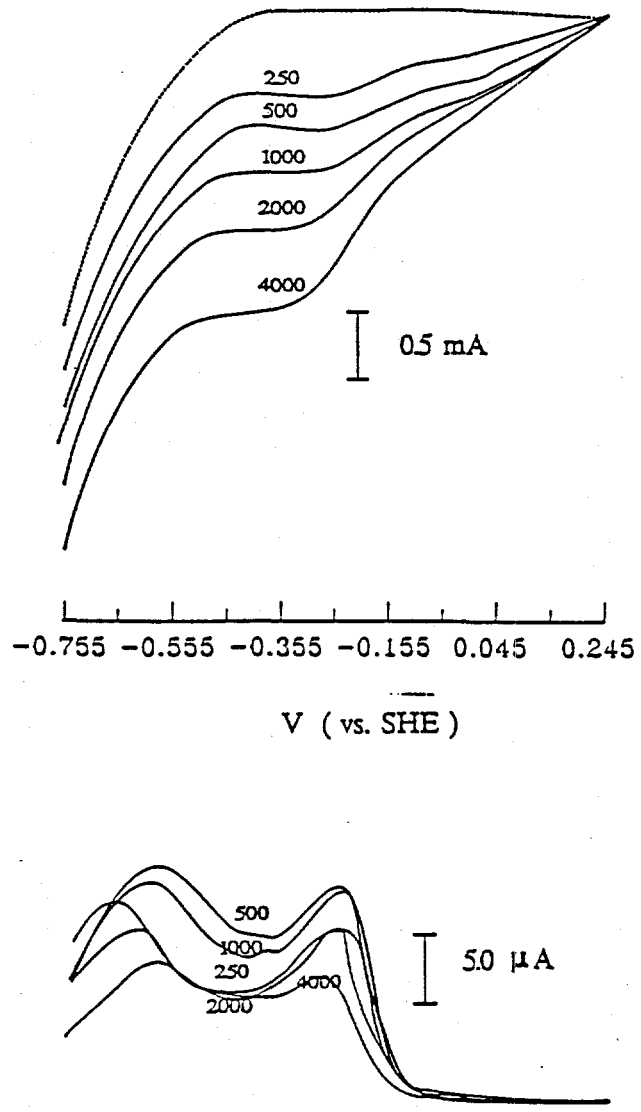

Figure 56. Ring-disc currents during linear potential sweeps for oxygen reduction on Chinese coal-pyrite at pH 4.6 (ring at 0.55 V, dashed line is the current in N_2 bubbled solution).

Mineral-pyrite showed a behavior similar to that shown in Figure 56. However, on Pittsburgh No. 8 coal-pyrite, most of the oxygen was reduced to water, with only a small amount of hydrogen peroxide escaping the disc surface. The electroactivity towards oxygen reduction at pH 4.6 for the three pyrite samples is in the same order as at pH 6.8.

All three pyrite samples examined in this study possessed a consistent characteristic, i.e., the magnitude of the diffusion-limited current for oxygen reduction followed the order: pH 6.8 > pH 9.2 > pH 4.6. The lowest oxygen reduction rate at pH 4.6 may be attributed to the cathodic decomposition of pyrite to elemental iron. The formation of passivating layers of iron hydroxide on the surface at pH 9.2 may explain the observation that the rate at pH 9.2 was lower than at pH 6.8.

Biegler et al. (1975) studied oxygen reduction on mineral-pyrite using the rotating disc electrode. They suggested the formation of hydrogen peroxide during oxygen reduction in acid solutions from changes in slopes on the voltammetry curves. Under neutral or alkaline conditions iron-hydroxides or oxides on the surface may catalyze the decomposition of peroxide (McIntyre and Peck, 1979). The present study clearly demonstrated that coal-pyrites are electroactive with respect to oxygen reduction. The difference in electroactivity for oxygen reduction among the three pyrite samples may be attributed to differences in crystalline defects and the morphology of the surface. While Chinese coal-pyrite exhibits a morphological appearance similar to that of mineral pyrite, Pittsburgh No. 8 coal-pyrite appears very different in that it is much more porous and poorly crystallized. It is believed that in neutral and acidic solutions, the more porous nature of Pittsburgh No. 8 coal-pyrite may hinder the diffusion of hydrogen peroxide away from the disc, fostering its further reduction to OH^- before it can be convected to the ring. At pH 9.2, the electroactivity of Pittsburgh No. 8 coal-pyrite to reduce oxygen is lower than that of the other two pyrites. This is possibly because in alkaline solutions, the pores of Pittsburgh No. 8 coal-pyrite become blocked with reaction precipitates.

Pyrite oxidation/reduction on rotating ring-disc electrodes: Figure 57 (top) shows the first and fifth voltammograms on a RRDE of Chinese coal-pyrite at pH 9.2. Previous studies with mineral pyrite at pH 11 (Ahlberg et al., 1990) and at pH 9.2 (Hamilton and Woods, 1981; Zhu et al., 1991)

concluded that the anodic peak I at -0.4 V represents the oxidation of elemental iron to $Fe(OH)_2$ by the reaction,

$$Fe + 2OH^- = Fe(OH)_2 + 2e^- \quad (E = -0.047 - 0.059pH). \tag{7}$$

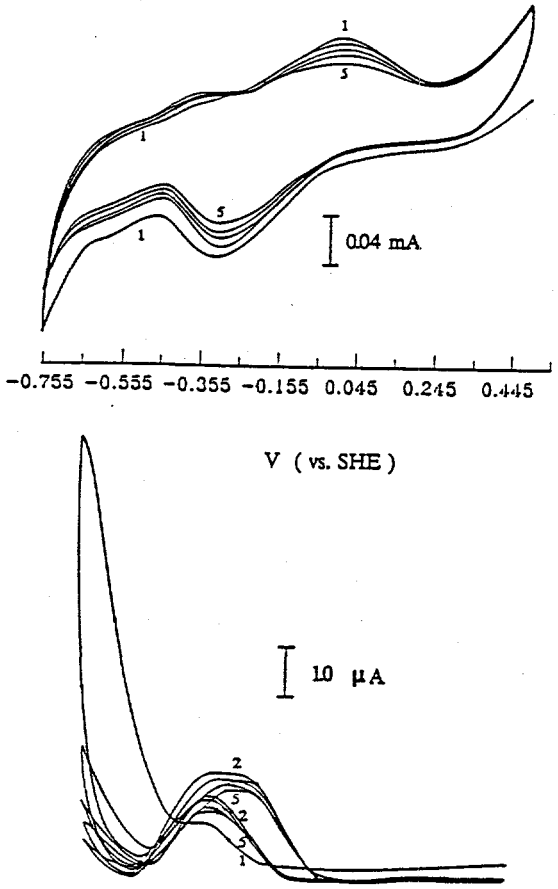

Figure 57. The first and fifth voltammograms on RRDE of Chinese coal-pyrite at pH 9.2 with ring held at 0.25 V.

Elemental iron is produced by the cathodic reduction of pyrite or of iron oxidation products during the negative going sweep. Anodic currents in this potential region may also be associated with the reaction,

$$Fe + HS^- + OH^- = FeS + H_2O + 2e^- \quad (E = -0.578 - 0.03pH - 0.03\log[HS^-]), \tag{8}$$

where HS^- is also produced on the surface of pyrite by its cathodic decomposition.

The current (III) on the anodic sweep at potentials above 0.25 V increases with increase in the upper potential limit up to 0.65 V, and has been attributed to the oxidation of pyrite itself to form sulfate and ferric hydroxide by the reaction (Hamilton and Woods, 1981; Ahlberg et al., 1990; Michell and Woods, 1978),

$$FeS_2 + 11H_2O = Fe(OH)_3 + 2SO_4^{2-} + 19H^+ + 15e^- \quad (E = 0.412 - 0.0749pH + 0.0078\log[SO_4^{2-}]). \tag{9}$$

Reductive decomposition of pyrite takes place at potentials more negative than -0.65 V, which is indicated by a consistent increase in cathodic current VI at potentials <-0.7 V.

The above reactions do not involve the production and conversion of hydrophobic species that render pyrite floatable in the absence of collectors and cannot explain the origin of collectorless flotation. For studying the self-induced flotation and depression of pyrite, the most important reactions are represented by peaks II and IV in Figure 57. Peak II, which occurs at 0 V on the anodic sweep, is generally attributed to the oxidation of $Fe(OH)_2$ to $Fe(OH)_3$ (Ahlberg et al., 1990; Zhu et al., 1991). This reaction presupposes that pyrite has been oxidized and a layer of $Fe(OH)_2$ has been formed on the surface which can be further oxidized to $Fe(OH)_3$. If this reaction is solely responsible for peak II, the charge associated with this peak cannot exceed that of peak I which represents the formation of ferrous hydroxide. However, peak II obviously contains more charge than peak I in Figure 57.

Hamilton and Woods (1981) and Buckley et al. (1988) reported that peak II was observed on sweeps commencing at potentials positive of peak I, even when a fresh surface free of iron hydroxide was generated by polishing under a nitrogen atmosphere. Our experiments confirmed their results.

Chander et al. (1992) resolved the anodic peak at -0.09 V into two current peaks by conducting voltammetry experiments in carbonate and EDTA (ethylenediaminetetraacetic acid) solutions. They suggested that oxidation of ferrous hydroxide and sulfur species both contribute to the anodic current. Michell and Woods (1978) determined the ferric hydroxide coverage on pyrite from the anodic peak at about -0.05 V on voltammograms and from X-ray emission spectroscopy. Careful examination of their data reveals that the amount of oxides on three different pyrite electrodes calculated from the integrated charge are considerably larger than that determined from X-ray emission measurements, although they claimed that there is a "good agreement" between them. The results suggest that anodic oxidation may involve species other than iron hydroxide. Work on freshly fractured electrodes to be discussed in Subtask 3.3 provides convincing evidence that peak II arises from both the oxidation of ferrous to ferric hydroxide and the oxidation of pyrite to a S^o-like species, i.e., elemental sulfur (S^o), polysulfides (FeS_n) or metal-deficient sulfides ($Fe_{1-x}S_2$), as shown in reactions (10)-(12).

$$FeS_2 + 3OH^- = 2S^o + Fe(OH)_3 + 3e^- \quad (E = 0.628 - 0.059pH), \tag{10}$$

$$nFeS_2 + 3(n-2)OH^- = 2FeS_n + (n-2)Fe(OH)_3 + 3(n-2)e^-, \tag{11}$$

$$FeS_2 + 3xOH^- = Fe_{1-x}S_2 + xFe(OH)_3 + 3xe^-. \tag{12}$$

Detailed discussion of pyrite oxidation will be provided in Subtask 3.3. When a surface has been previously oxidized to a significant extent, the current due to pyrite oxidation on voltammetry curves may be essentially masked by the oxidation of $Fe(OH)_2$ to $Fe(OH)_3$.

It is noticed in Figure 57 that there is a substantial difference in the ring current between the first and the subsequent cycles. This can be explained by assuming that at least two reduction processes, i.e., reactions (13) and (14), are associated with peak IV.

$$Fe(OH)_3 + e^- = Fe(OH)_2 + OH^- \quad (E = 0.271 - 0.059pH), \tag{13}$$

$$(n-1)Fe(OH)_3 + FeS_n + 3(n-1)e^- = nFeS + 3(n-1)OH^-. \tag{14}$$

Reaction (13) produces a soluble ferrous hydroxide and reaction (14) an insoluble iron sulfide. As a result, peak IV would depend on the total amount of $Fe(OH)_3$ and sulfur-rich species (as excess sulfur in the lattice, polysulfide, or elemental sulfur) produced on the prior anodic sweep, and the ring current only on the amount of $Fe(OH)_3$ that is reduced to a soluble ferrous species. On the first cathodic sweep, there was less iron hydroxide to react with sulfur-rich species by reaction (14), and hence more HS^- released from the disc as the reduction product. On subsequent sweeps, the abundance of sulfur-rich species relative to iron hydroxide diminishes since most of the iron hydroxide produced during the anodic sweeps remain on the surface, while the major portion of HS^- diffuses into the bulk solution.

Further support for assigning at least two reduction processes to peak IV is provided in Figure 58, where the anodic limit has been increased. It is mentioned previously that pyrite oxidation can occur *via* two paths, reactions (9) and one or more of reactions (10) - (12). The relative yield of S^o-like species and SO_4^{2-} depends on the anodic limit. Higher potentials favor sulfate formation and thus lead to a reduction in the quantity of insoluble, reducible sulfur species on the electrode relative to the quantity of $Fe(OH)_3$. On the reverse cathodic sweep, a lower surface concentration of reducible sulfur species should decrease the contribution of reaction (14) to peak IV and increase the amount of soluble ferrous hydroxide that is reoxidized on the ring. This is consistent with Figure 57 which shows that the ring current increases with increases in the anodic limit, while the charge associated with peak IV changes only slightly with the anodic limit.

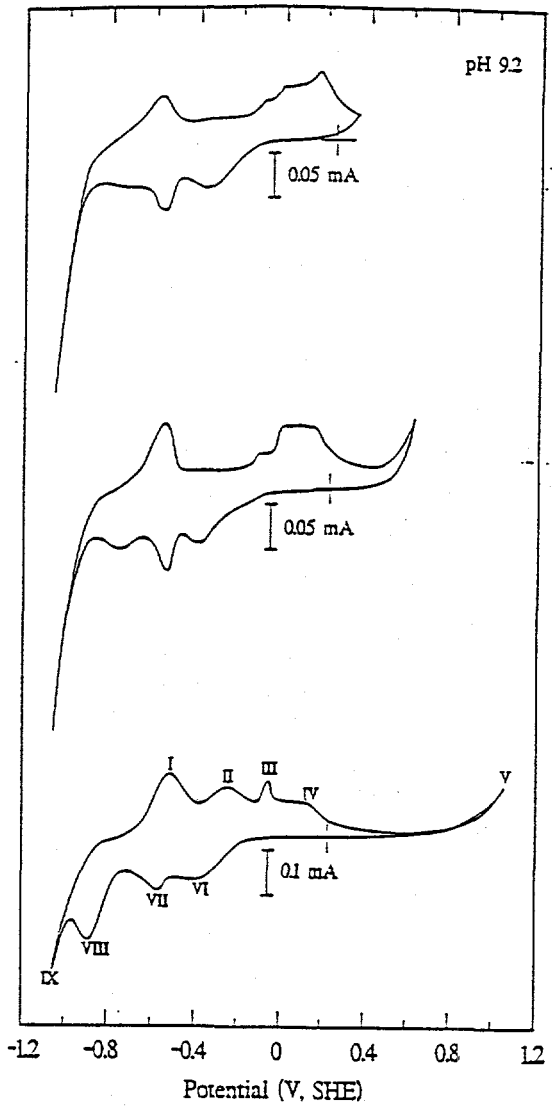

Figure 58. Voltammograms on RRDE of Chinese coal-pyrite at pH 9.2 with upper potential limit at 0.05 V, 0.25 V and 0.55 V. Ring was held at 0.25 V.

Figure 58 (bottom) shows the current observed at the gold ring held at 0.25 V. During the cathodic sweep, a ring current commences at -0.1 V which is clearly associated with oxidation of the species reduced over peak IV. The reduction product for this peak is believed to be a soluble ferrous hydroxide species such as $Fe(OH)_2$, $Fe(OH)^+$, Fe^{2+}, etc. (Fornasiero and Ralston, 1992). From the measured collection efficiency, it is determined that approximately 10 to 20% of the species reduced over peak IV is reoxidized on the ring. This value appears to be unreasonable if one only considers

thermodynamics of the hydrolysis of ferrous ions (K_{sp}=4.79×10^{-17} for $Fe(OH)_2$). However, thermodynamic data are true only at equilibrium. It is believed that pyrite oxidation may generate a number of intermediates. For example, Chander and Briceno (1987) and Chander et al. (1992) suggested that intermediate sulfur oxidation products may include $S_2O_3^{2-}$, $S_xO_y^{2-}$, etc. Zhu et al. (1991) proposed the reaction,

$$FeS_2 + (y+1)H_2O = Fe(OH)^{2+} + S_2O_y^{2-} + (2y+1)H^+ + (2y+1)e^- \qquad (15)$$

to explain the loss of passivation of pyrite during oxidation in stirred solution. In addition, hydrogen ions produced in reaction (9) can significantly reduce the local pH of the solution in the vicinity of the electrode, enhancing the dissolution of ferric hydroxide. It has been reported that the pH near an electrode can be different from its bulk value in a solution layer of a thickness of up to 1 mm (Kuhn and Chan, 1983). Finally, the intense centrifugal force and solution turbulence created by electrode rotation may facilitate the diffusion of ferrous species before they can be nucleated and precipitated on the surface of pyrite.

Figure 57 also shows that the ring current below -0.6 V during the cathodic sweep is associated with the reduction process labeled VI and perhaps also with peak V, particularly on the first sweep. Peak V has been attributed to the reduction of sulfur to HS^- (Zhu et al., 1991), with the sulfur produced on the positive going sweep. The height of this peak increases considerably with the addition of 1 mM Na_2S (not shown). The current increase at VI arises from the cathodic decomposition of pyrite, which produces HS^-. The ring current on the cathodic sweep at disc potentials < -0.6 V is due to the oxidation of HS^- to S^o.

Figure 59 illustrates the effect of the addition of ferrous chloride on the disc voltammograms and the ring response. It can be seen that with 5×10^{-5} M Fe^{2+} in solution, the cathodic peak IV on the disc voltammograms increased considerably and the peak potential shifted to about -0.4 V, confirming

the suggestion that part of the peak results from the reduction of ferric compounds. A second cathodic peak is also resolved at -0.65 V and can be attributed to the reduction of ferrous hydroxide to elemental iron. The additional ring current observed during both the cathodic and anodic sweeps indicates that the addition of Fe^{2+} leads to an increase in $Fe(OH)_3$ formation during the anodic sweep at potentials near 0 V, and a subsequent increase in the concentration of soluble ferrous hydroxide produced during the cathodic sweep. The addition of Fe^{2+} also increased the ring current during the subsequent anodic scan, indicating a larger amount of elemental iron was produced at the negative potential limit which was then oxidized to form the soluble ferrous hydroxide species. However, it appears that the addition of ferrous ions hinders the reduction of pyrite at potentials < -0.7 V, possibly due to the existence of a thick passivating layer on the surface. This effect is similar to that observed when a high upper potential limit is used (Buckley and Woods, 1984; Zhu et al., 1991), where the potential for pyrite reduction shifts to values more negative than -0.9 V.

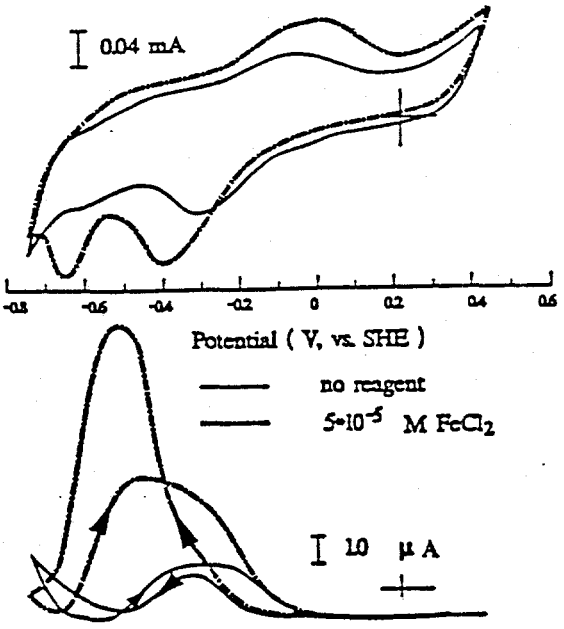

Figure 59. Voltammograms on RRDE of Chinese coal-pyrite at pH 9.2 in the absence/presence of ferrous chloride with ring held at 0.25 V.

Mineral- and Pittsburgh No. 8 coal-pyrite exhibit voltammograms similar to those for the Chinese coal-pyrite at pH 9.2. Figure 60 shows the second voltammograms and ring currents of the three pyrites for comparison. Both of the coal-pyrites are significantly more reactive than mineral-pyrite. It is interesting to notice that the oxidation of Pittsburgh No. 8 coal-pyrite produces less soluble species than the other two pyrites, while it forms more insoluble products than mineral-pyrite; on the other hand, mineral-pyrite generates the least amount of insoluble products. The difference in the relative amount of soluble to insoluble oxidation products may partially explain the differences in the flotation behavior of various pyrites.

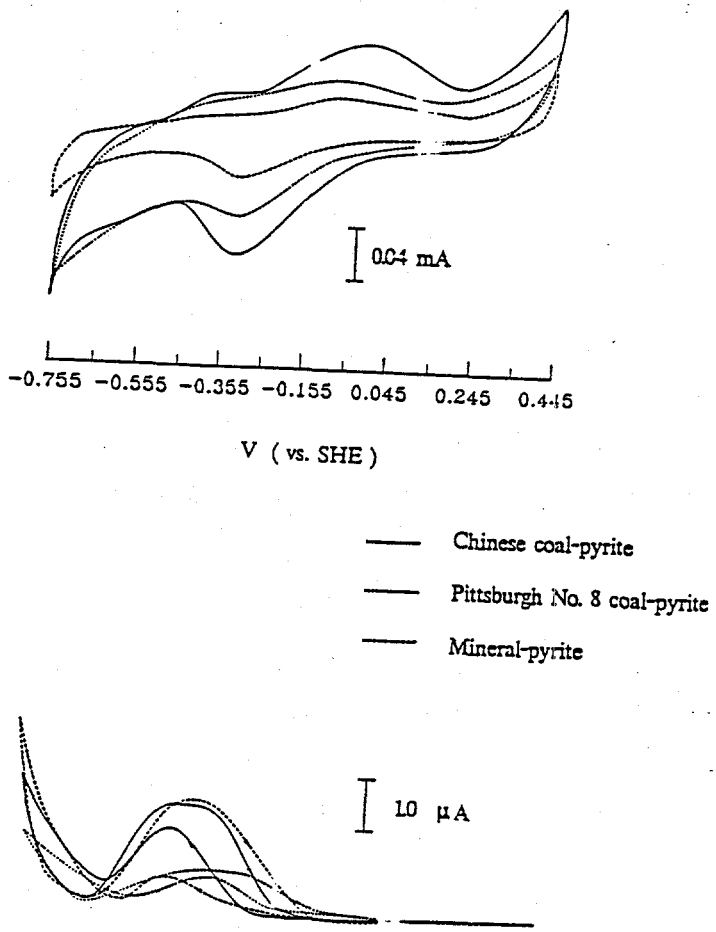

Figure 60. Ring-disc voltammograms of different pyrite samples at pH 9.2 (ring at 0.25 V).

Figure 61 shows the disc voltammograms and ring responses for three pyrite specimens at pH 6.8. Chinese coal-pyrite behaves similarly to mineral-pyrite but Pittsburgh No. 8 coal-pyrite exhibits considerably different characteristics. For mineral- and Chinese coal-pyrite, the cathodic peak on the disc voltammogram is observed at -0.1 V and results in a ring current. This behavior is similar to that exhibited at pH 9.2, with the peak shift due to the pH dependence of the reaction. Two small anodic peaks at -0.25 V and 0.1 V are more clearly discernable using a more sensitive current scale (not shown). The ring current is significant at the beginning of the anodic sweep and seems to be relatively constant up to 0.15 V, but no peak is present, in contrast with the observation at pH 9.2. In contrast, Pittsburgh No. 8 coal-pyrite exhibits a cathodic peak at -0.28 V which does not yield a corresponding ring current, implying that no soluble species is formed during cathodic reduction. The voltammetry curves and ring currents on the three pyrites clearly establish that the oxidation and reduction processes on Pittsburgh No. 8 coal-pyrite are considerably different than those on mineral-pyrite and those on well-crystallized Chinese coal-pyrite. Pittsburgh No. 8 coal-pyrite is much more reactive than the other pyrites and the products of the reaction appear to be different since no soluble reaction products are detected at the ring during the voltammetry sweeps.

The increased reactivity and the absence of soluble reaction products on Pittsburgh No. 8 coal-pyrite may arise from its porous nature, with the reactions taking place internally in pores. The large surface area associated with numerous pores would increase the apparent reactivity, whereas the reactions in pores would hinder diffusion of soluble products to the surface of the electrode where they could be convected to the ring to undergo further reaction.

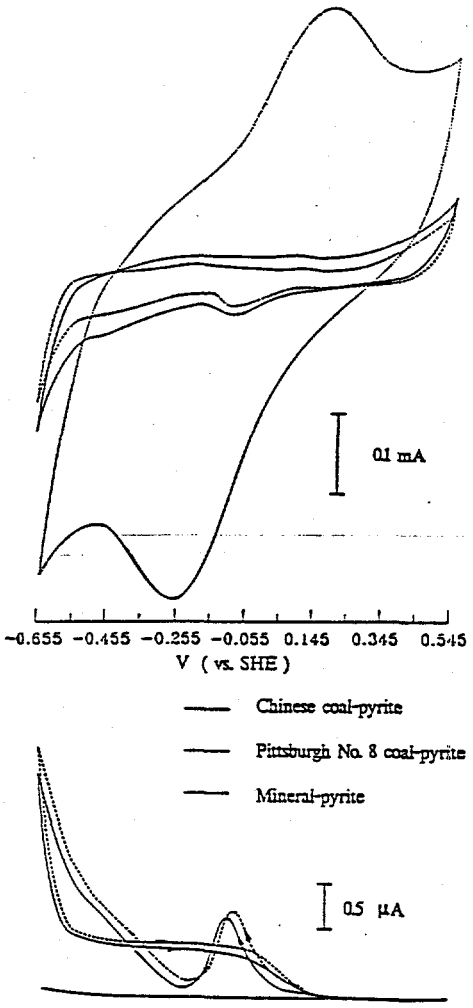

Figure 61. Ring-disc voltammograms of different pyrite samples at pH 6.8 (ring at 0.25 V).

At acidic pH's, pyrite exhibited a considerably different electrochemical behavior than at pH 9.2 and at pH 6.8. Figure 62 illustrates the disc voltammograms and ring currents between -0.4 V and 0.55 V at pH 4.6, when the potential of the ring electrode was held 0.25 V. Hamilton and Woods (1981) showed that a step is present on voltammograms of mineral pyrite at 0.4 V in pH 4.6 solutions during anodic sweeps on stationary electrodes, but not on rotating electrodes. The step was attributed to the reaction,

$$Fe^{2+} + 3H_2O = Fe(OH)_3 + 3H^+ + e^- \quad (E = 0.971 - 0.177pH - 0.059\log[Fe^{2+}]) \qquad (16)$$

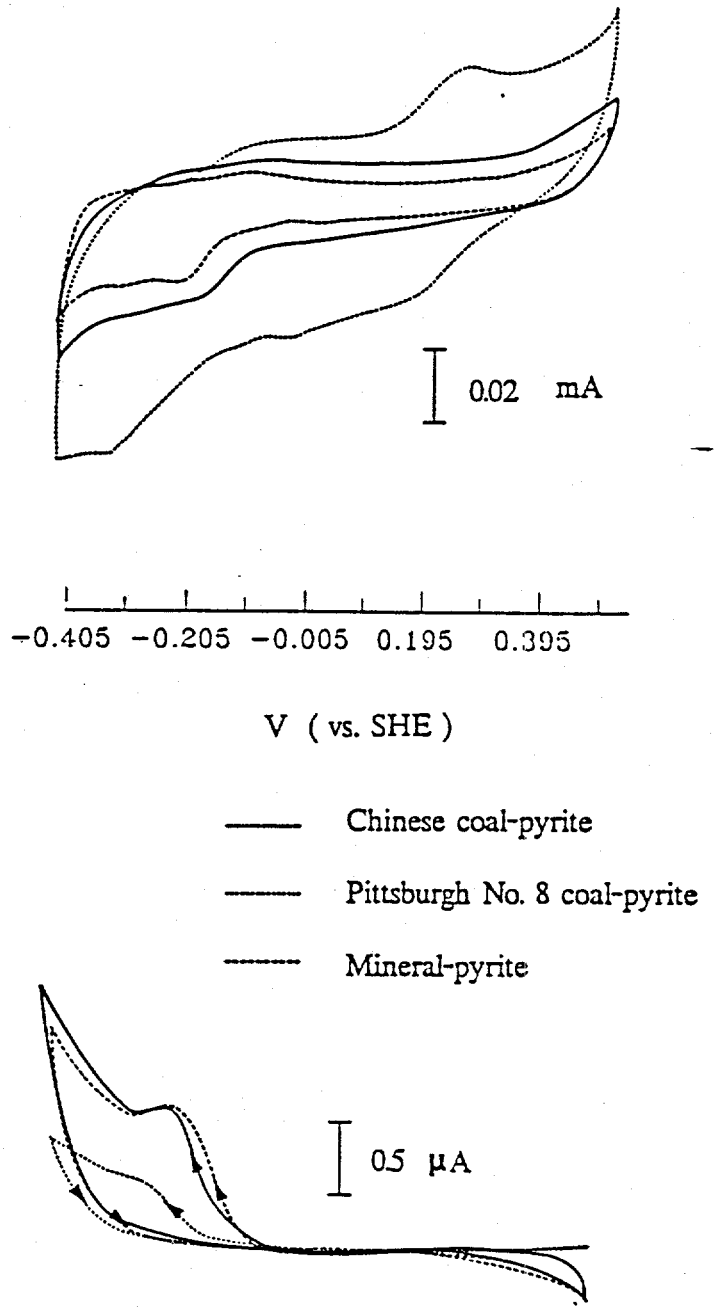

Figure 62. Ring-disc voltammograms of different pyrite samples at pH 4.6 (ring at 0.25 V).

and its absence on rotating electrodes was explained by the convection of the reactant, Fe^{2+}, away from the surface. In agreement with their results, there is no step at 0.4 V on rotating electrodes of mineral- and Chinese coal-pyrite (Figure 62). However, a distinct oxidation peak is observed at this potential on

the Pittsburgh No. 8 pyrite. There is a corresponding reduction process on the subsequent negative going sweep that begins at 0.3 V and is believed to represent the reverse of reaction (16). This provides further evidence that Pittsburgh No. 8 coal-pyrite is different from mineral-pyrite and Chinese coal-pyrite. Again, this difference can be accounted for by assuming that the surface area of the Pittsburgh No. 8 coal-pyrite is much larger than that of the other pyrites due to the presence of numerous pores and that the diffusion and convection of soluble reactants and products in the pores are hindered.

Distinct reduction processes are observed at potentials < -0.05 V on the voltammetry curves for the mineral- and coal-pyrite electrodes. The currents in this range of potentials are believed to represent the reduction of excess sulfur produced by anodic reaction at potentials > 0.4 V. Since the formation of $Fe(OH)_3$ is suppressed by dispersion of Fe^{2+} on the rotating electrode, the major insoluble reaction product formed at anodic potentials is excess sulfur, i.e., there is little $Fe(OH)_3$ to be reduced on the mineral- and Chinese coal-pyrite. On these two pyrites, the reduction of excess sulfur and oxidation of the reduction product result in a finite ring current. On the Pittsburgh No. 8 coal-pyrite, a broad reduction process begins at about 0.3 V on the cathodic sweep and continues until the cathodic limit is reached. Both $Fe(OH)_3$ and excess sulfur are present on the surface at the beginning of the cathodic sweep and the broad reduction process represents the reformation of an iron sulfide (FeS) when these products are reduced. It is believed that the $Fe(OH)_3$ is depleted before the excess surface sulfur. Thus, at more negative potentials, a sulfur species is reduced to H_2S and its reoxidation produces a small ring current. The H_2S does not appear to be trapped in the pores. This may be because the production of gaseous H_2S builds up sufficient pressure to force the product out of the pores.

Subtask 3.2: Determination of Reducing Potentials

Different metals have long been known to have different redox potentials in aqueous solutions and to undergo galvanic coupling when they are electrically connected. The metal that has the higher redox potential will act as a cathode, where reduction processes take place, and the metal that possesses the lower redox potential serves as the anode on which oxidation processes occur. Upon galvanic coupling, the potentials of two electrodes approach each other, i.e., the potential at the anode increases while the potential at the cathode decreases. Sulfide minerals are semiconducting materials and demonstrate behaviors similar to those of metals. Pyrite has been found to be the most noble of the sulfide minerals. Its rest potential is 0.6 V at pH 4.6 and 0.18 V at pH 9.2 (Chander and Briceno, 1987). Metals such as zinc (Zn), manganese (Mn) and aluminum (Al) possess theoretical redox potentials of -0.763 V, -1.185 V and -1.662 V, respectively, which are more negative than that of pyrite. When one of these metals is coupled with pyrite the potential of the pyrite electrode will be significantly reduced.

Figure 63 shows the potentials of both pyrite and metal (aluminum and manganese) electrodes as a function of galvanic coupling time. Prior to galvanic coupling, Pittsburgh No. 8 coal-pyrite possessed a potential of ~ -0.1 V at pH 9.2 while aluminum and manganese electrodes had potentials of -0.97 V and -1.09 V, respectively. Upon galvanic coupling with manganese, the potential of pyrite decreased to -0.43 V in a period of 60 seconds. It is believed that the following electrode reactions occur:

$$\textit{Cathode (pyrite):} \quad Fe(OH)_3 + e^- = Fe(OH)_2 + OH^- \quad \textit{and} \quad S^0 + H_2O + 2e^- = HS^- + OH^- \tag{18}$$

$$\textit{Anode (Manganese):} \quad Mn + 2OH^- = Mn(OH)_2 + 2e^- \tag{17}$$

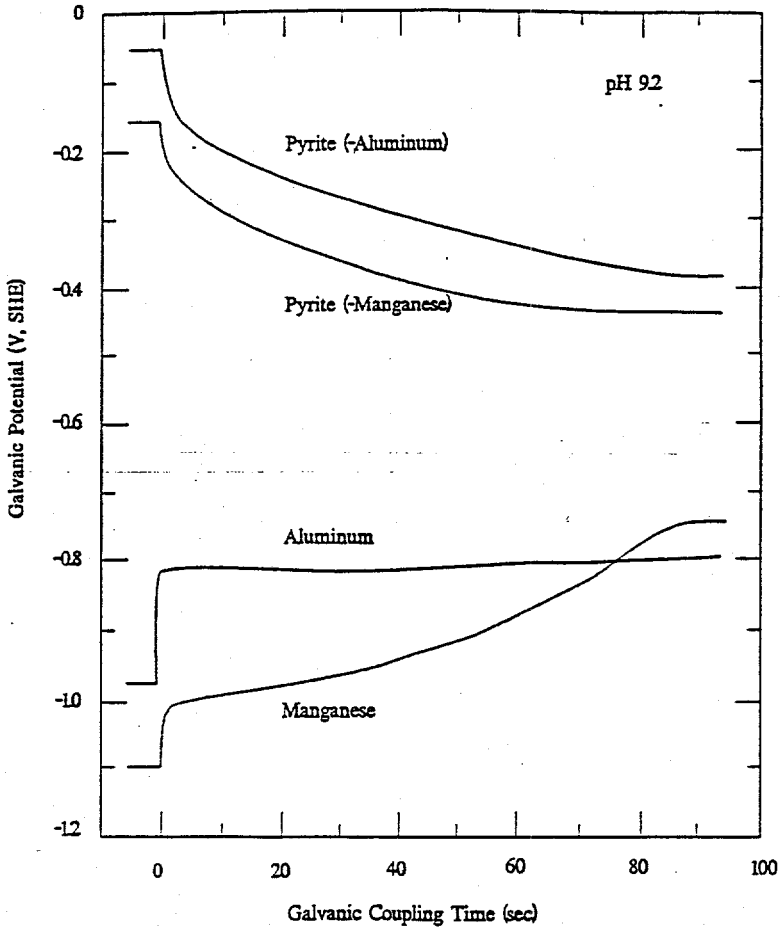

Figure 63. Potentials of Pittsburgh No. 8 coal-pyrite and metal (aluminum and manganese) electrodes as a function of galvanic coupling time at pH 9.2.

Galvanic coupling of pyrite with aluminum showed similar effects. The pyrite electrode assumed a potential of -0.38 V about 80 seconds after contact with aluminum.

The galvanic coupling between pyrite and zinc showed a much different behavior, as shown in Figure 64. Upon coupling, the potential of zinc increased from -0.91 V to -0.31 V in 1.4 minutes while the potential of pyrite decreased from -0.03 V to -0.17 V. However, the potential of zinc decayed for about 2.5 minutes, then gradually increased to -0.27 V. The potential decreased again, eventually reaching -0.54 V. The pyrite potential showed corresponding complex changes over the entire period of time. This experiment was repeated several times and reproducible results were obtained. The

irregular changes in potentials may be associated with the build-up and break-down of zinc hydroxide (solubility $K_{sp}=7.68\times10^{-17}$) on the zinc electrode. The process may be represented by the following reaction:

$$Zn + 2H_2O = Zn(OH)_2 + 2H^+ + 2e^- \quad (19)$$

In fact, white powder-like precipitates were observed on the surface of the zinc electrode after the experiments.

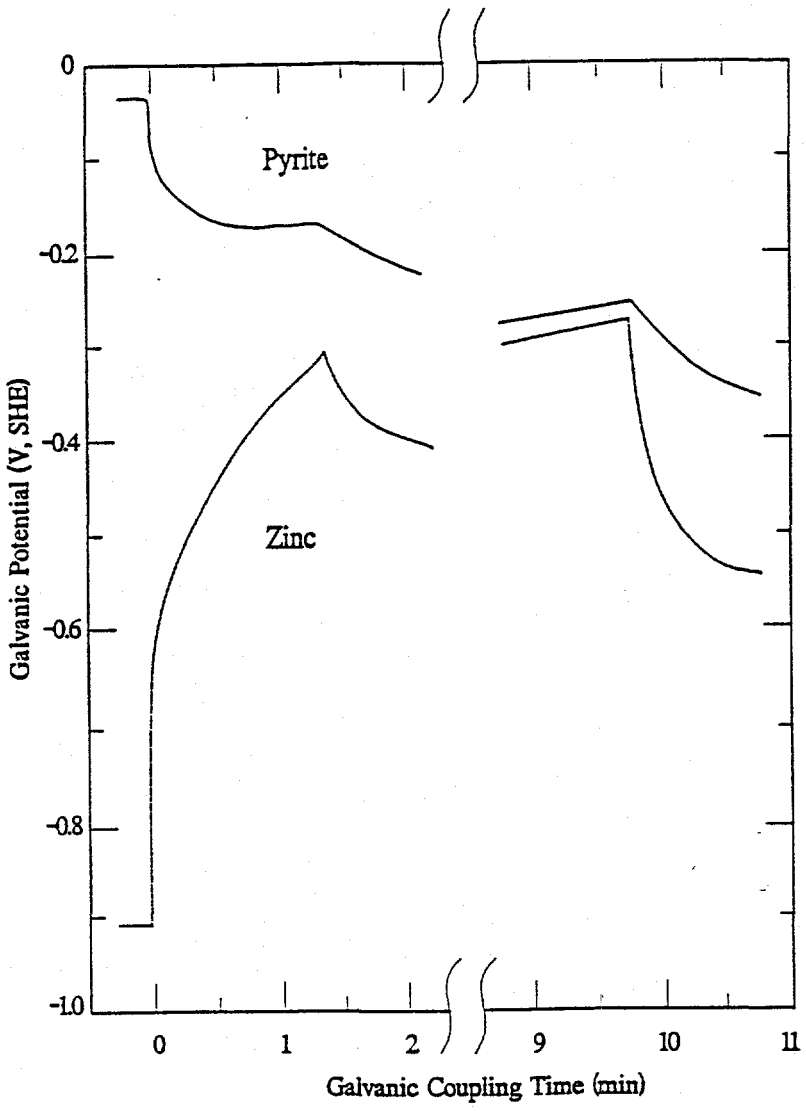

Figure 64. Potentials of Pittsburgh No. 8 coal-pyrite and zinc electrodes as a function of galvanic coupling time at pH 9.2.

Figure 65 demonstrates how the galvanic coupling currents vary as a function of time. All currents showed a steady decay after contact. However, the magnitude of the initial and equilibrium coupling currents and the decay rates differ significantly. Aluminum showed the highest initial and equilibrium currents, which may be attributed to its fast oxidation kinetics. Zinc exhibited an initial current intermediate between those of aluminum and manganese and the smallest equilibrium current. Manganese showed the lowest initial current and an equilibrium current larger than that of zinc but smaller than that of aluminum.

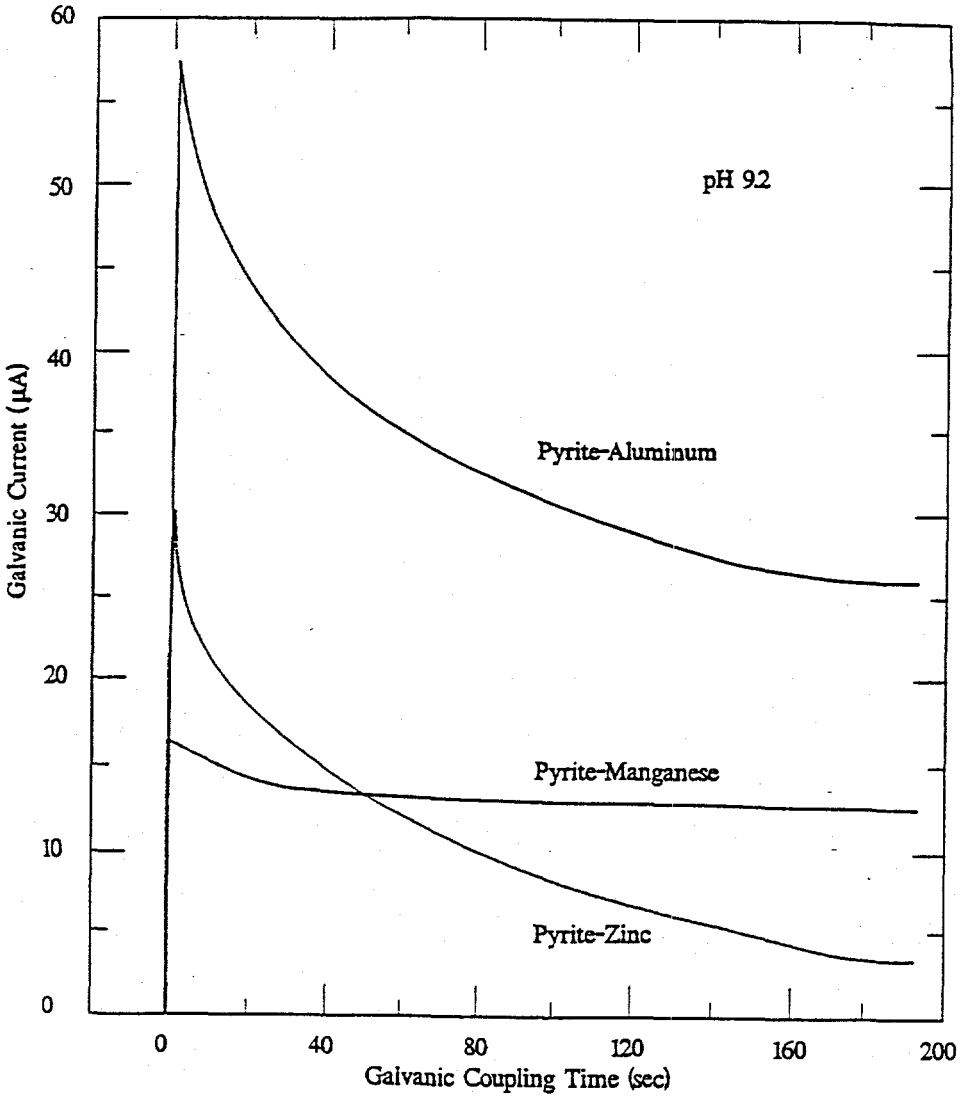

Figure 65. Galvanic coupling currents between Pittsburgh No. 8 coal-pyrite and metals as a function of time at pH 9.2.

Figure 66 shows the galvanic potentials of Pittsburgh No. 8 coal-pyrite with aluminum, zinc and manganese versus coupling time at pH 4.6. These potentials changed in a way similar to that shown in Figure 63. However, there are differences; the potentials measured on pyrite and zinc electrodes do not show complex changes after galvanic coupling as observed at pH 9.2. This may be due to the lack of a passivating layer on zinc at pH 4.6. It is important to notice that at pH 4.6, galvanic coupling appears to be more effective in reducing the pyrite potential than at pH 9.2. At pH 9.2, the potential of pyrite can be lowered by 0.3 to 0.4 V by galvanic coupling with zinc, manganese or aluminum, while at pH 4.6 it can be reduced by as much as 0.8 V. However, the galvanic current observed at pH 4.6 (not shown) is considerably larger than at pH 9.2, which could imply higher consumption of sacrificial metal in practical processes.

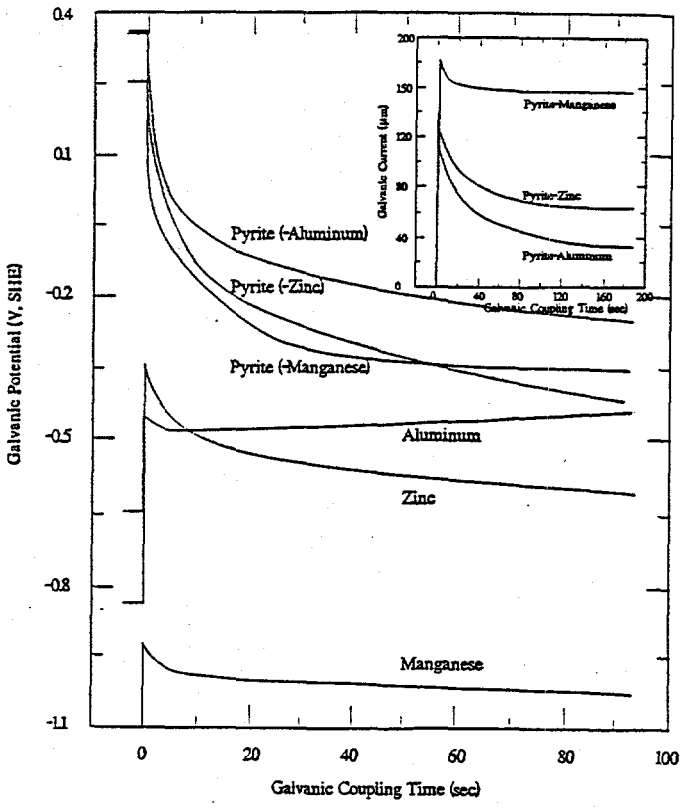

Figure 66. Potentials of Pittsburgh No. 8 coal-pyrite and metal (aluminum, zinc and manganese) as a function of galvanic coupling time at pH 4.6. The inset shows the galvanic current.

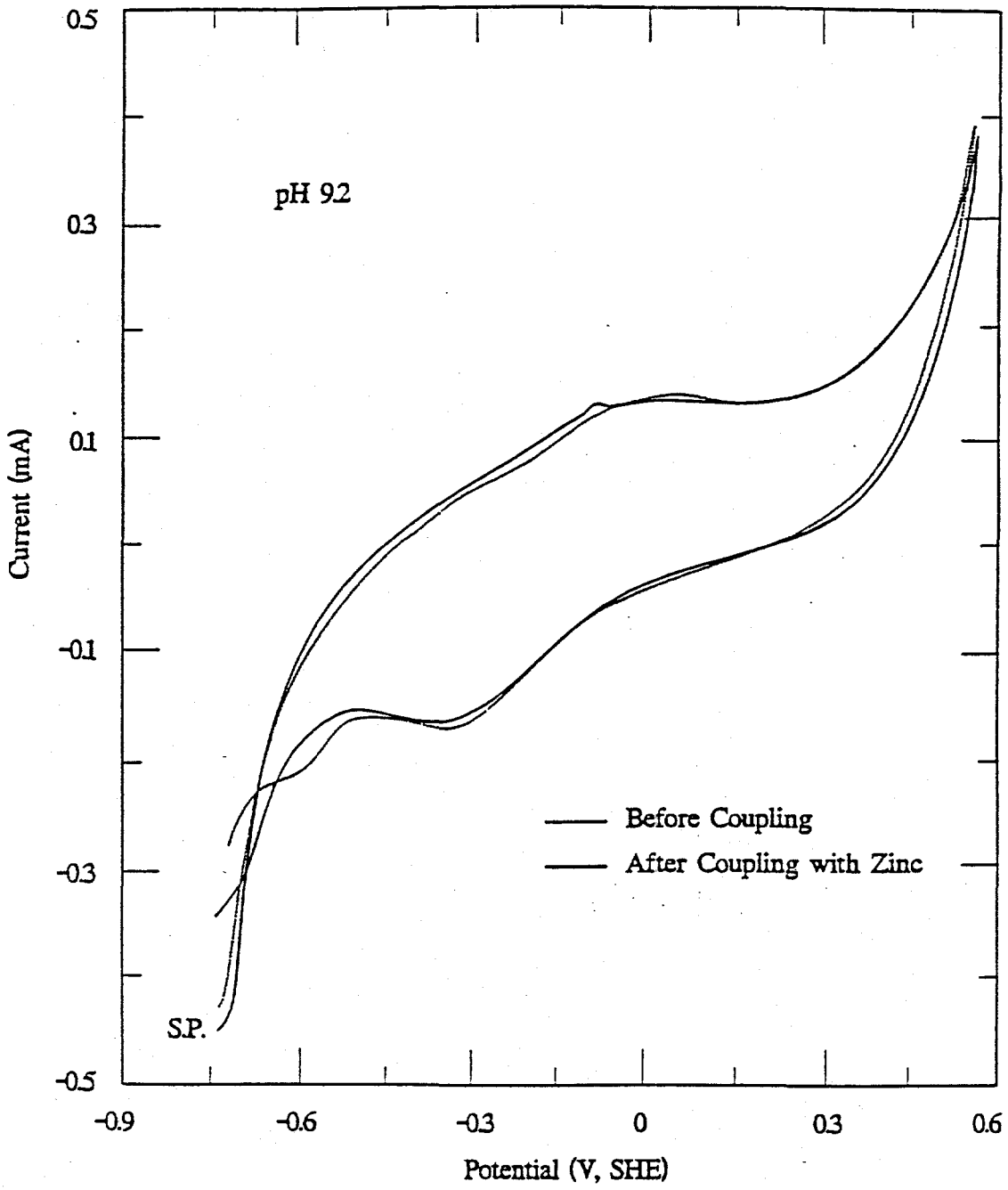

Figure 67. First-cycle voltammograms of Pittsburgh No. 8 coal-pyrite before and after galvanic coupling with a zinc anode for 30 minutes at pH 9.2.

Figure 67 compares the first-cycle voltammograms of Pittsburgh No. 8 coal pyrite before and after galvanic coupling for 30 minutes at pH 9.2. It is apparent that galvanic coupling altered the

voltammogram. The anodic peak at -0.1 V is distinguishable on the voltammogram when pyrite has been subjected to galvanic coupling. This may be attributed to the following anodic reactions:

$$HS^- + (1-x)Fe + OH^- = Fe_{1-x}S + H_2O + 2e^- \quad (20)$$

$$2FeS = FeS_2 + Fe^{2+} + 2e^- \quad (21)$$

$$HS^- + OH^- = S^o + H_2O + 2e^- \quad (22)$$

where FeS or HS^- is the product of galvanic coupling. The smaller major anodic peak at ~ 0 V after galvanic coupling may also indicate that some ferric hydroxide, formed during electrode polishing, is reduced to a more soluble species. There is also a difference in the cathodic sweep. Prior to galvanic coupling, there is a cathodic wave at -0.6 V which increases and becomes a distinct peak in the following cycles. After galvanic coupling, however, this wave disappears in all five cycles in the potential range scanned. Galvanic coupling appeared to have cleaned the pyrite surface and/or changed the local pH, inhibiting the anodic product that produces the cathodic peak.

One of the objectives of the present work is to determine if galvanic coupling can reduce hydrophobic sulfur species on already oxidized pyrite to some soluble species such as HS^-. If this is true, peaks characteristic of soluble species will disappear on the voltammograms after galvanic coupling in a stirred solution. It is of importance, therefore, to study the effect of solution stirring during galvanic coupling.

Figure 68 shows the first voltammogram of the Illinois No. 6 coal-pyrite electrode after it was galvanically coupled with a manganese anode at pH 4.6. In quiescent solution, galvanic coupling greatly reduced the anodic peak at 0 V and the cathodic peak at -0.2 V. In stirred solution, galvanic coupling eliminated these peaks. These two peaks were found by Hamilton and Woods (1981) and Tao et al. (1993) to correspond to oxidation/reduction processes involving the S^o/HS^- couple. Apparently, galvanic coupling reduced sulfur-like species to HS^-, which diffused away from the

surface. Solution stirring accelerated the diffusion process. The removal of sulfur-like species from the surface eliminates the source of the hydrophobicity of pyrite and reduces its self-induced floatability.

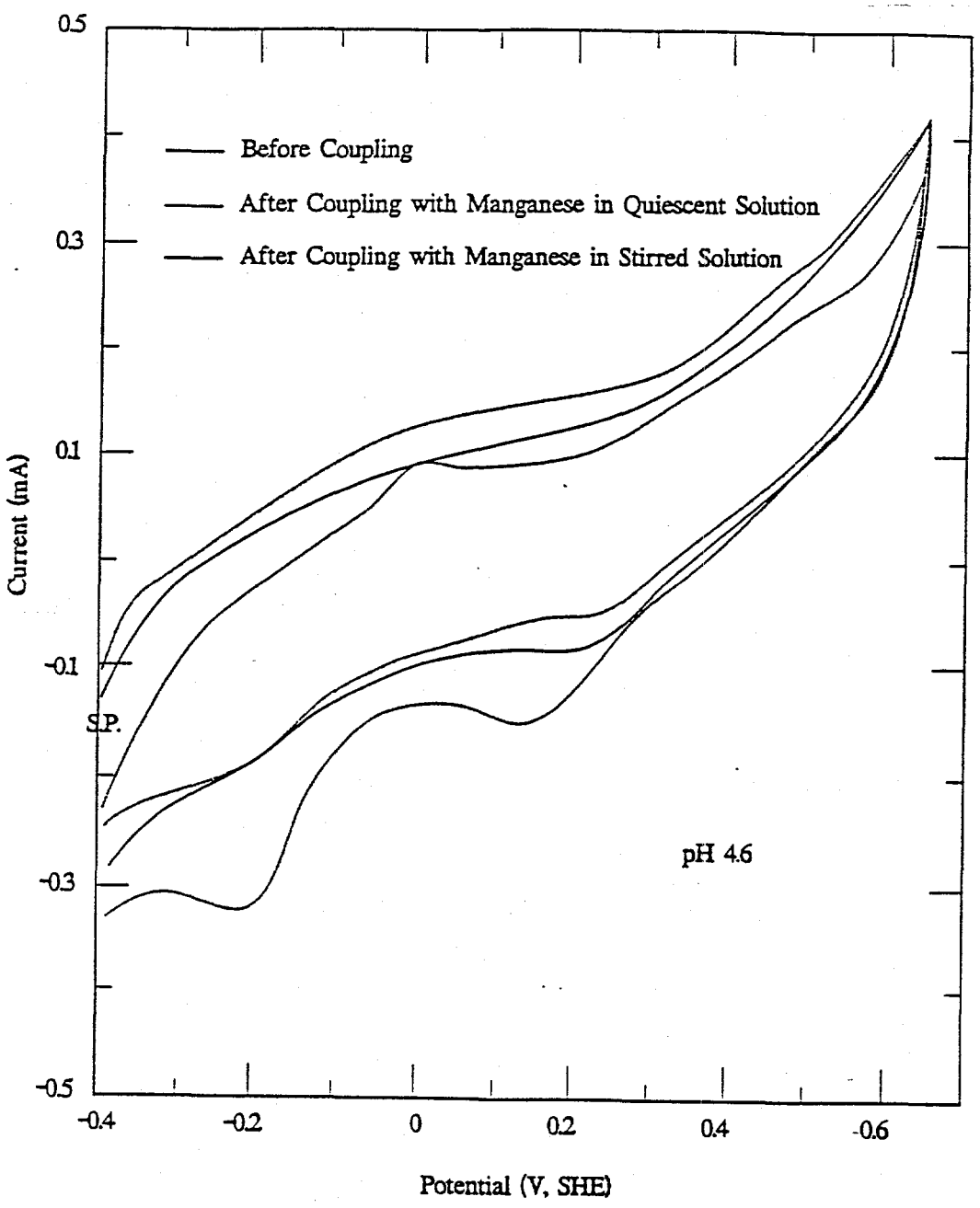

Figure 68. The effect of galvanic coupling of Illinois No.6 coal-pyrite with a manganese anode on the first voltammograms at pH 4.6.

Subtask 3.3: Mechanism/Kinetics of Pyrite Oxidation by Cyclic Voltammetry

Incipient oxidation of pyrite on in situ fractured electrodes: Figure 69 illustrates chronoamperometry curves (current as a function of time after fracture) of Chinese coal pyrite electrodes at pH 9.2. Before discussing these curves, it is worthwhile pointing out the similarity between chronoamperometry on a fractured surface to the better known technique of controlled potential step chronoamperometry for studying electroactive species in solution. In the latter, the potential is stepped from an electrochemically inactive region to a value where an electroactive species is rapidly reduced or oxidized. This requires, initially, a large current to reduce or oxidize those species within the reaction layer at the surface. Charging of the double layer and redox processes involving any adsorbed species are fast processes that contribute to the initial current. The current then decays as a concentration gradient that controls the diffusion of the electroactive species to the surface develops. The present experiments differ from the usual controlled potential step method in several aspects. First, the electroactive species is the pyrite electrode itself. Second, the potential step experienced at fracture represents the difference between the applied potential and the potential a newly created surface assumes at the instant of fracture. Third, fracture momentarily destroys the double layer, and a new double layer must be formed on the surface. Based on these comparisons, it is believed that the initial spike observed on the current-time curves at the moment of fracture represents a combination of double layer charging and faradaic oxidation (or reduction) of the fresh pyrite surface. Double layer charging is fast compared to the time scale used in Figure 69, and thus the decay in the current after the initial spike is believed to represent primarily faradaic reactions involving pyrite.

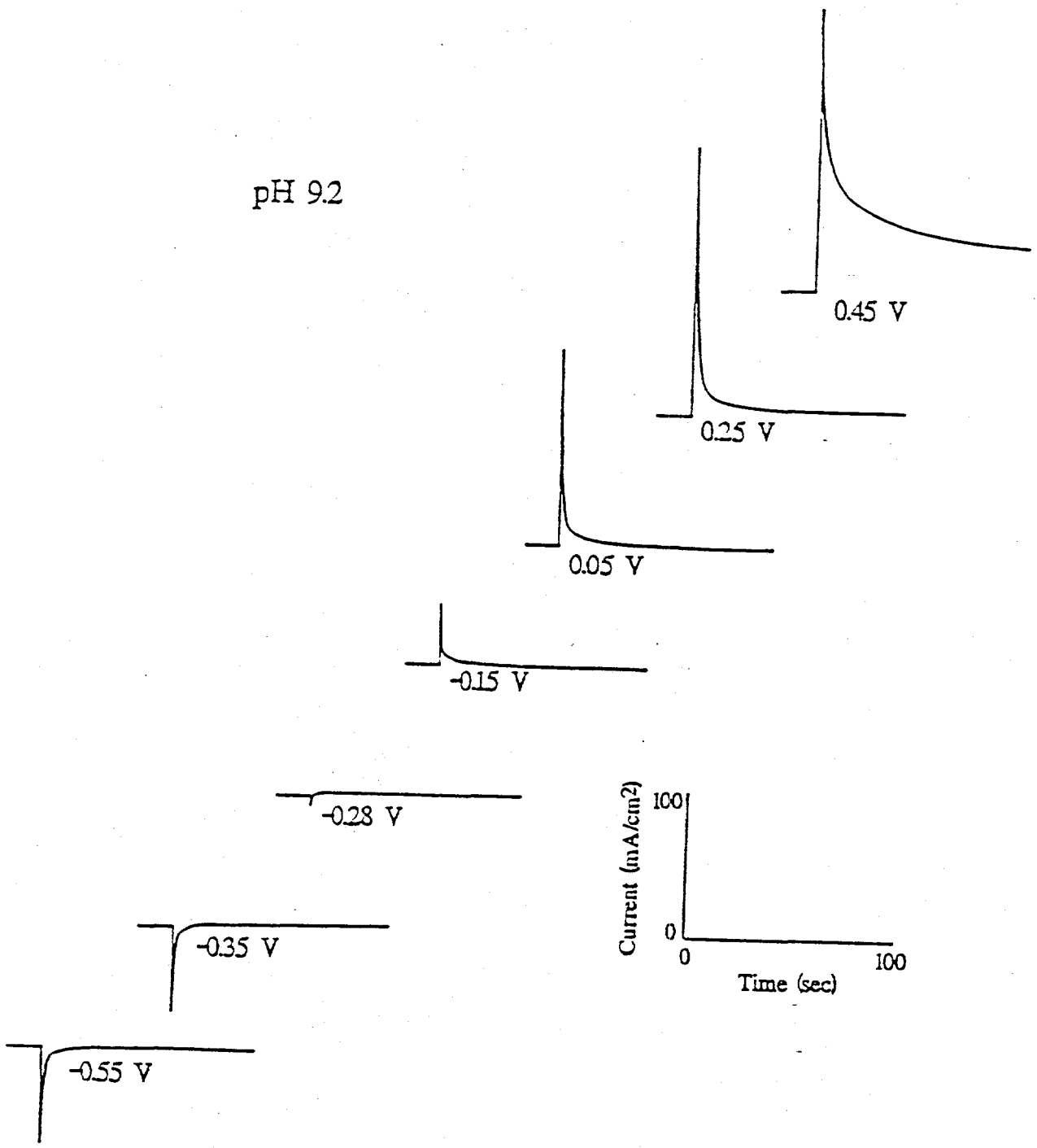

Figure 69. Chronoamperometry curves of Chinese coal-pyrite fractured at different potentials at pH 9.2.

In chronoamperometry experiments, electrodes were potentiostated at different potentials in the range -0.55 V to 0.45 V. Before fracture the electrodes were held for 5 to 20 minutes at the indicated potentials until a steady state current (usually very close to zero) was reached. Anodic (positive) currents obtained after fracture indicate pyrite undergoes oxidation following fracture and cathodic (negative) currents suggest pyrite undergoes reduction. A zero current at fracture indicates pyrite is neither oxidized nor reduced. Figure 69 establishes that pyrite undergoes spontaneous oxidation when fractured at potentials of -0.15 V or higher, and spontaneous reduction when fractured at -0.35 V or lower. The fresh surface created at -0.28 V exhibited nearly zero current. It appears that the "zero-reaction" potential of pyrite is at about -0.28 V at pH 9.2. This represents the potential at which neither oxidation nor reduction of pyrite takes place to a significant extent. It can be assumed that a fresh pyrite surface remains stable at this potential. When pyrite is placed in air-saturated solutions or exposed to the open air, it will inevitably undergo significant oxidation since the potential is always higher than -0.28 V. The fact that the mixed potential of pyrite is 0.18 V at pH 9.2 (Chander and Briceno, 1987) establishes that pyrite is oxidized in normal aqueous solutions.

Electrodes fractured in aqueous solutions at pH 4.6 exhibited chronoamperometry curves similar to these shown in Figure 69 with the "zero-reaction" potential shifted to ~ 0 V. The "zero-reaction" potentials of -0.28 V and 0 V obtained at pH 9.2 and pH 4.6 lie within the thermodynamic stability domain on the E_h-pH diagram for pyrite, as shown in Figure 70. The chronoamperometry technique developed in the present work is significant because it specifies not only a method of *obtaining* an unreacted pyrite surface, but also a way of *maintaining* an unreacted surface, i.e., fracture pyrite while holding its potential in the region where pyrite is thermodynamically stable. This procedure overcomes one of the usual difficulties of interpreting electrochemical measurements on sulfide electrodes due to the presence of oxidized products arising from the preparation of the

electrodes, e.g., products introduced by polishing. For pyrite, pre-oxidation leads to voltammograms that appear to be dominated by Fe^{o}/Fe^{2+} and Fe^{2+}/Fe^{3+} redox couples. The presence of these species makes it difficult to determine when pyrite itself begins to oxidize to form incipient oxidation products. The identification of the sulfur oxidation products, e.g., polysulfides, metal-deficient sulfide, or elemental sulfur, is of particular interest in flotation and the reactions leading to these products may be masked by iron containing species.

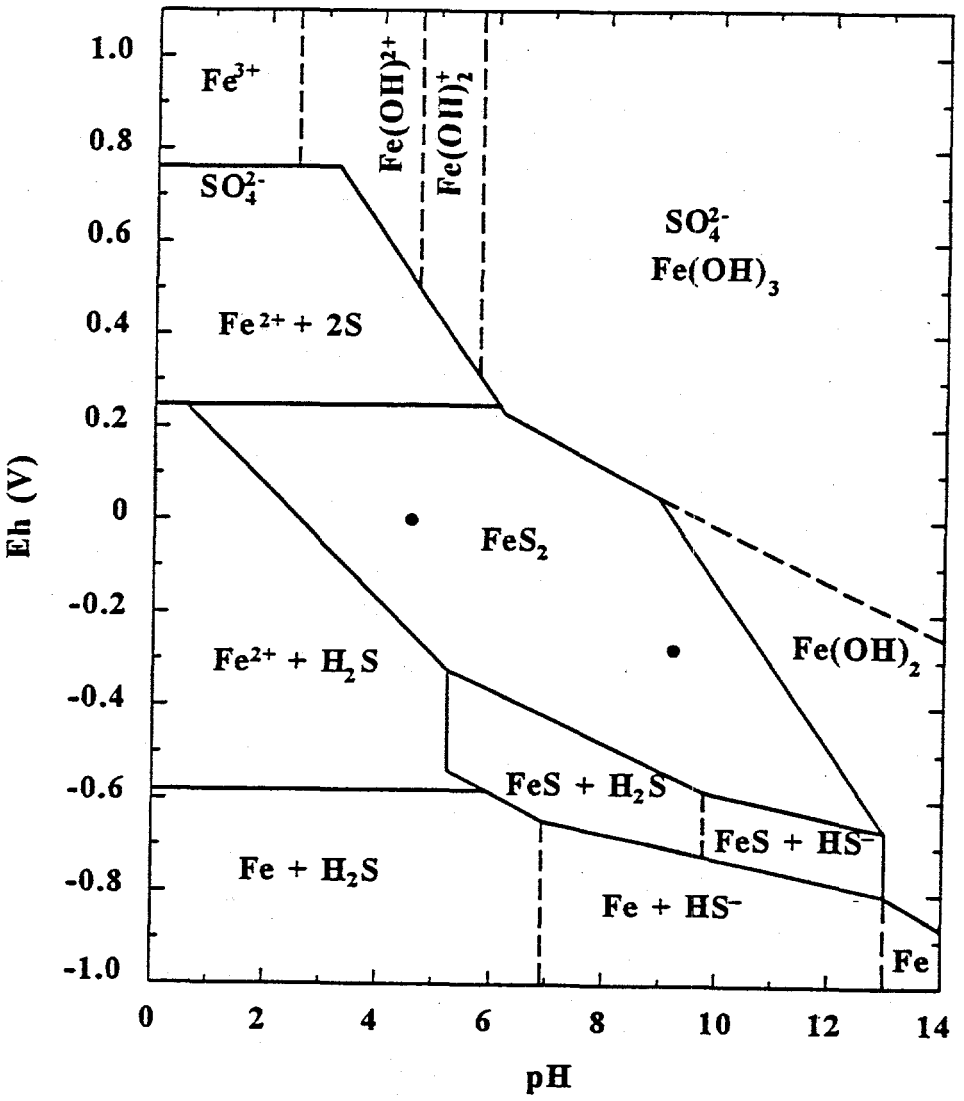

Figure 70. Eh-pH diagram for Fe-S-H_2O system at 298 K and 10^{-5} M (Kocabag et al., 1990). Two points in the middle of the stability domain were obtained in the present study.

The first three voltammograms obtained on a fresh pyrite surface generated by fracture at -0.28 V are shown in Figure 71. The potential sweep was started at -0.28 V in the anodic direction and reversed at 0.25 V on the first cycle. The lower potential limit was chosen to be -0.55 V to avoid

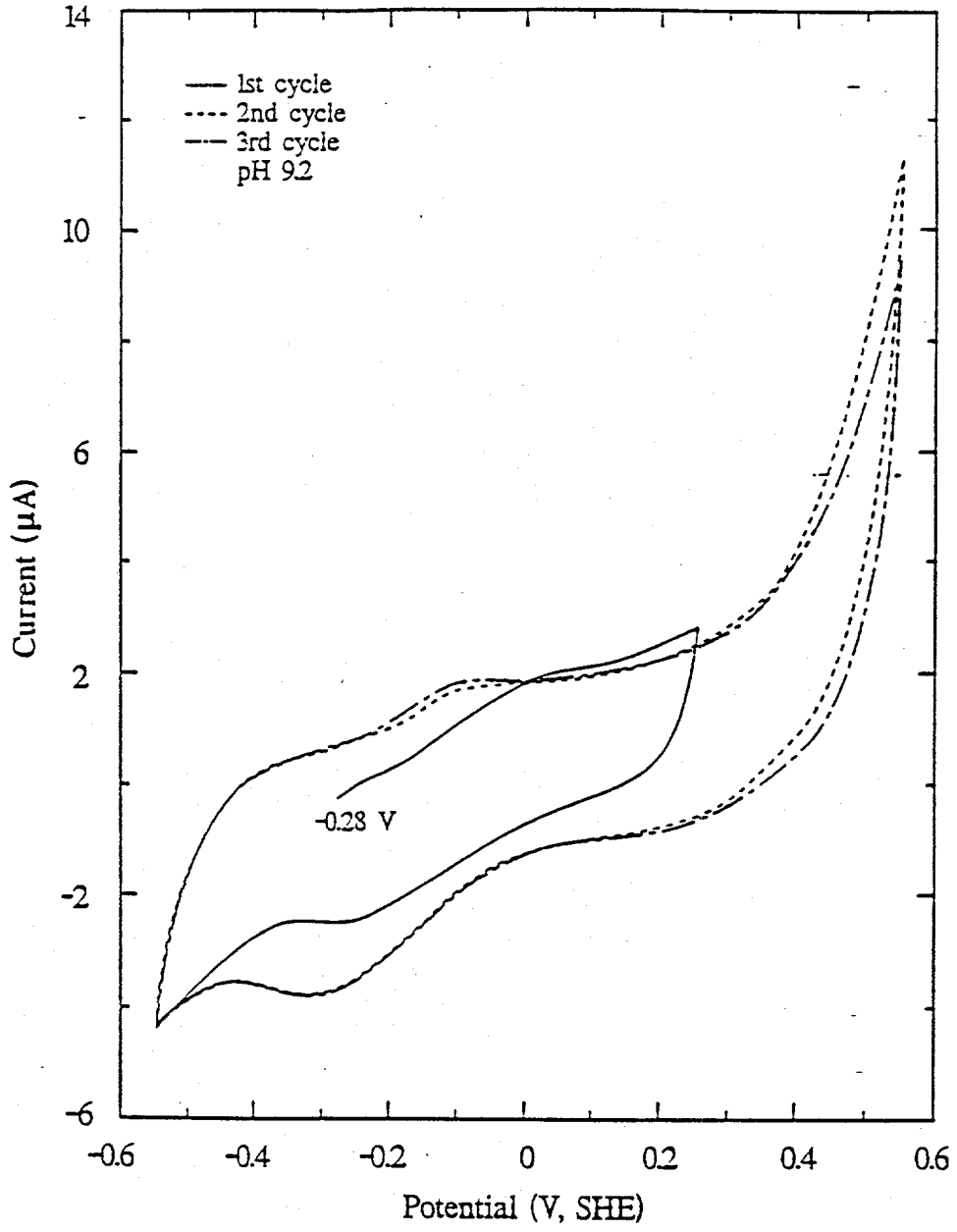

Figure 71. Voltammograms on Chinese coal-pyrite freshly fractured at -0.28 V at pH 9.2. The potential sweep started anodically.

possible complications that may arise from the aggressive reductive decomposition of pyrite to elemental iron that was found to occur near -0.7 V at pH 9.2. On the second potential sweep, the upper potential limit was set at 0.55 V to show the effect of aggressive oxidation of pyrite on the subsequent voltammogram.

An oxidation current appears at about -0.20 V on the first voltammogram with an anodic peak at about 0 V. Since the pyrite electrode was held at -0.28 V during fracture, no elemental iron or ferrous hydroxide should be present on the surface. The current can only arise from the oxidation of pyrite itself. The possible reactions are one or more of reactions (10) - (12). Hamilton and Woods (1981) abraded pyrite under nitrogen to prevent oxidation and found an oxidation peak at approximately 0 V at pH 9.2. They attributed this peak to pyrite oxidation to $Fe(OH)_3$ and elemental sulfur. From XPS studies, Buckley and Woods (1984) established that moderate oxidation of pyrite leaves sulfur in normal lattice sites, creating a metal-deficient surface ($Fe_{1-x}S_2$). Yoon et al. (1991) observed significant flotation of pyrite at potentials slightly above -0.1 V and suggested from XPS and electrochemical studies that polysulfides (FeS_n) are more likely oxidation products. XPS and Laser Raman spectroscopic studies conducted by Zhu et al. (1991) and Mycroft et al. (1990) supported this conclusion. Since the equilibrium potential for reaction (10) is 0.09 V, i.e., significantly above -0.15 V, Figure 71 suggests polysulfides or a metal-deficient sulfide is formed rather than elemental sulfur. It is believed that this sulfur-rich sulfide or S^o-like species could render pyrite floatable at -0.1 V as observed by Yoon et al. (1991).

The oxidation current near 0 V is considerably different on the second and third sweeps than on the first sweep. No peak is observed at 0 V on the second and third sweeps, but a new peak occurs at -0.1 V. This peak is known to represent the oxidation of $Fe(OH)_2$ to $Fe(OH)_3$ (Zhu et al., 1991). The presence of passivating layers of $Fe(OH)_3$ on the surface may retard or even inhibit the oxidation

of the mineral, making it difficult to observe the initial oxidation of pyrite on the second and third sweeps. The same problem arises when polished electrodes are used. It can thus be concluded that multiple potential sweeps and/or the use of polished electrodes cannot be used to study the early stages of pyrite oxidation.

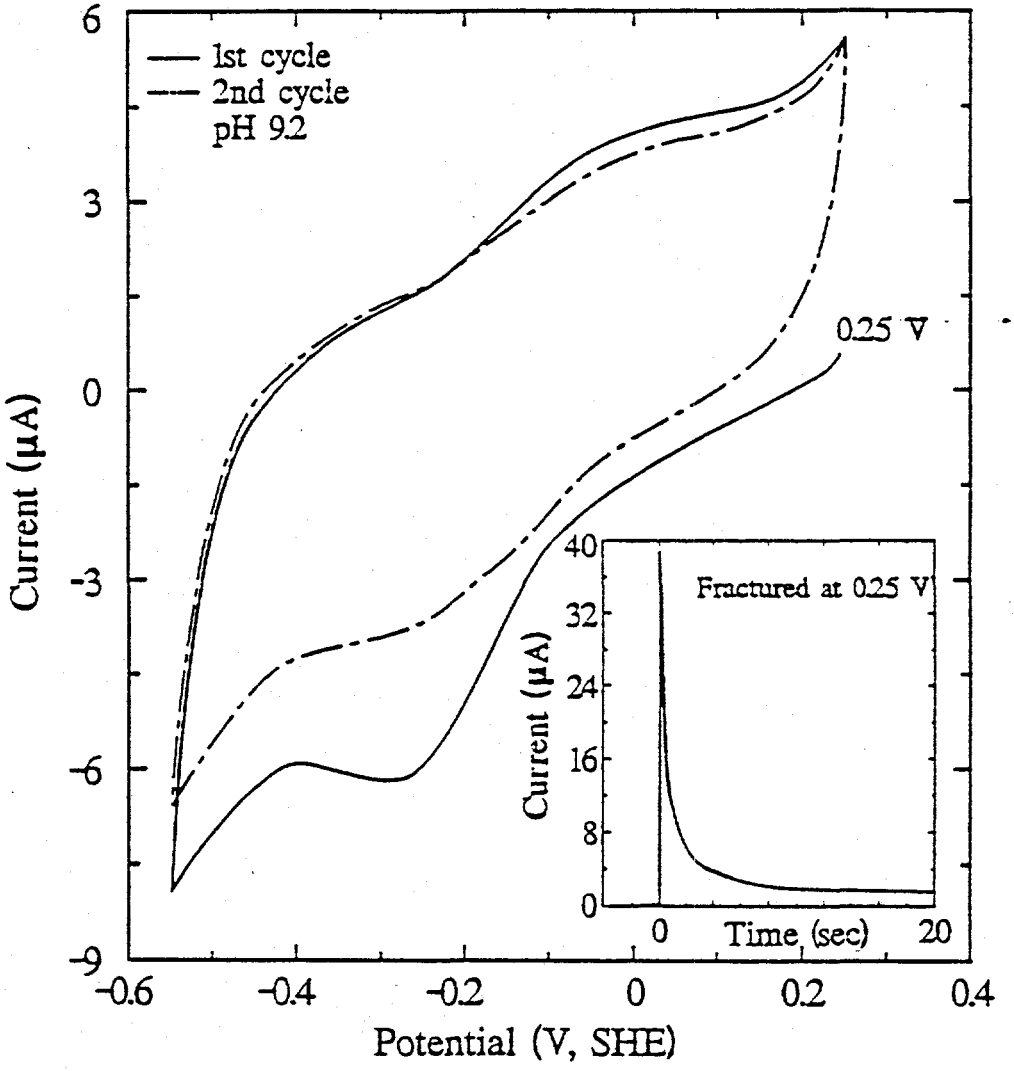

Figure 72. The first voltammogram on Chinese coal-pyrite freshly fractured at 0.25 V at pH 9.2. The inset is the chronoamperometry curve upon fracture.

Figure 72 shows the first voltammetry curve obtained on a fresh surface of pyrite that was fractured at 0.25 V. The inset illustrates the current passed as a function of time after fracture. The charge generated during the first two minutes is approximately 550 mC/cm^2, based on the geometric surface area of the electrode. This charge density corresponds to the oxidation of approximately two or three monolayers of pyrite for a three electron oxidation process such as reaction (10). After holding the electrode at 0.25 V for approximately four minutes after fracture, voltammograms were obtained with the potential sweep starting in the negative direction to reduce the oxidation products formed at 0.25 V. There is a reduction process beginning at about -0.05 V, with a cathodic peak at -0.27 V. The integrated charge is about 510 mC/cm^2 between -0.05 and -0.55 V. This reduction current confirms that solid oxidation products formed on pyrite during oxidation at 0.25 V can be reduced at -0.05 V. Since approximately the same charge was consumed at fracture as on the subsequent negative going potential scan, reduction of sulfur oxidation products (polysulfide or metal-deficient sulfide) must also be involved in this process, in addition to reduction of ferric to ferrous hydroxide.

Experiments were also carried out to investigate the reduction of pyrite, as shown in Figure 73. The electrode was freshly fractured at -0.28 V to minimize surface alteration of pyrite. The potential sweep began cathodically from -0.28 V. Since the fresh surface has not undergone oxidation, the first cathodic current must arise from the reduction of pyrite. The initial cathodic current observed from -0.28 V to -0.7 V is believed to represent the reduction of pyrite to iron sulfide. The greater current below -0.7 V represents the aggressive reduction of pyrite to elemental iron. The possible reactions are (Ahlberg et al., 1990; Zhu et al., 1991; Peters and Majima, 1968),

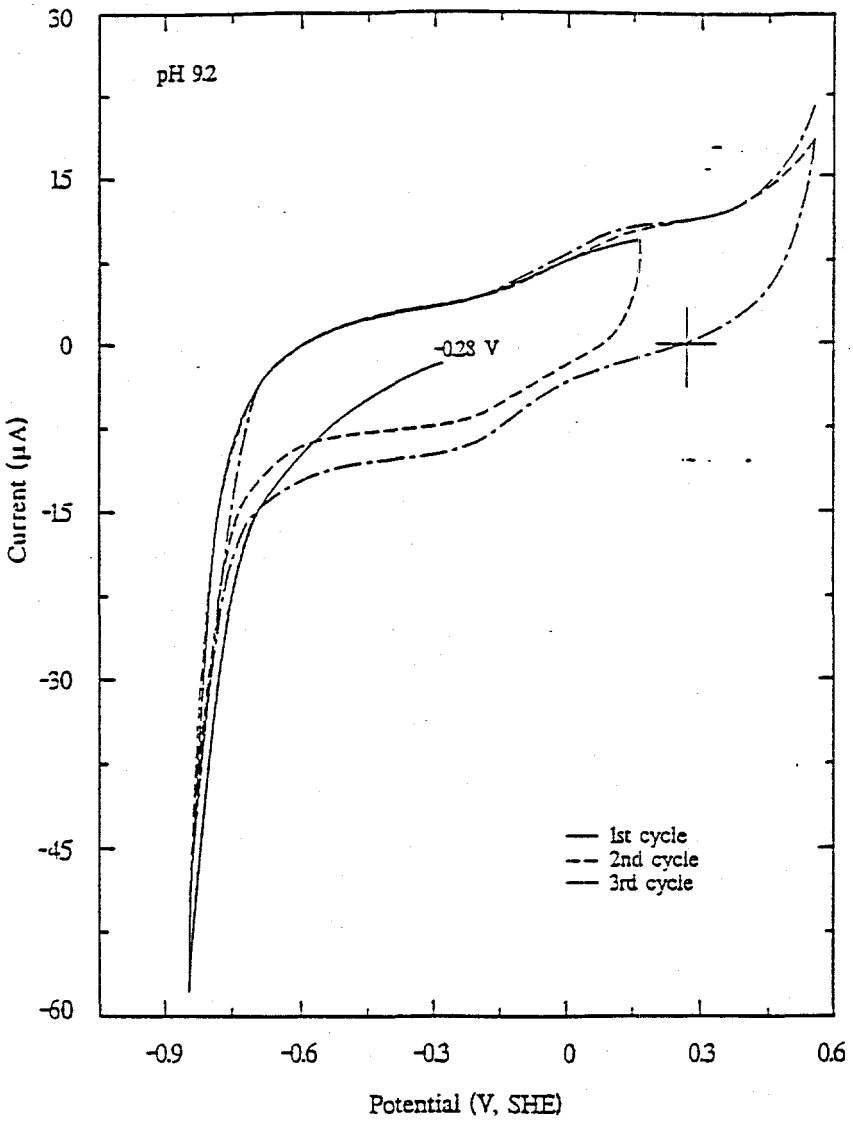

Figure 73. Voltammograms on Chinese coal-pyrite freshly fractured at -0.28 V at pH 9.2. The potential sweep started cathodically.

$$FeS_2 + H_2O + 2e^- = FeS + HS^- + OH^- \quad (E = -0.403 - 0.03pH - 0.03\log[HS^-]) \tag{23}$$

$$FeS_2 + 2H_2O + 4e^- = Fe + 2HS^- + 2OH^- \quad (E = -0.491 - 0.03pH - 0.03\log[HS^-]) \tag{24}$$

Interestingly, the cathodic process between -0.3 and -0.6 V observed on the first sweep (finite slope) is absent on the second and third voltammograms. This shows that the initial reduction of pyrite observed on the first reduction cycle is different than on subsequent sweeps. Continued sweeps shifted the pyrite reduction potential toward more negative values and eventually a small cathodic peak was resolved at -0.7 V. The potential of this peak shifted to more negative values when the upper potential limit was increased.

When the pyrite electrode was fractured at -0.45 V, a significant cathodic current was observed, as shown by the inset in Figure 74. This current gave rise to a charge density of 106 mC/cm^2 during the first two minutes after fracture, which corresponds to a reduction reaction involving less than a monolayer of pyrite. The first two voltammograms after fracture at -0.45 V are shown in Figure 74. The potential sweep was initiated in the positive direction to oxidize reduction products formed following fracture. An anodic current appears at -0.25 V, which reaches a peak at about 0 V. The integrated charge density from -0.25 V to 0.25 V on the voltammogram is 240 mC/cm^2, considerably larger than 110 mC/cm^2 produced when the electrode was fractured and held at -0.45 V. This difference provides further evidence that the oxidation of pyrite itself contributes to the anodic current in this range.

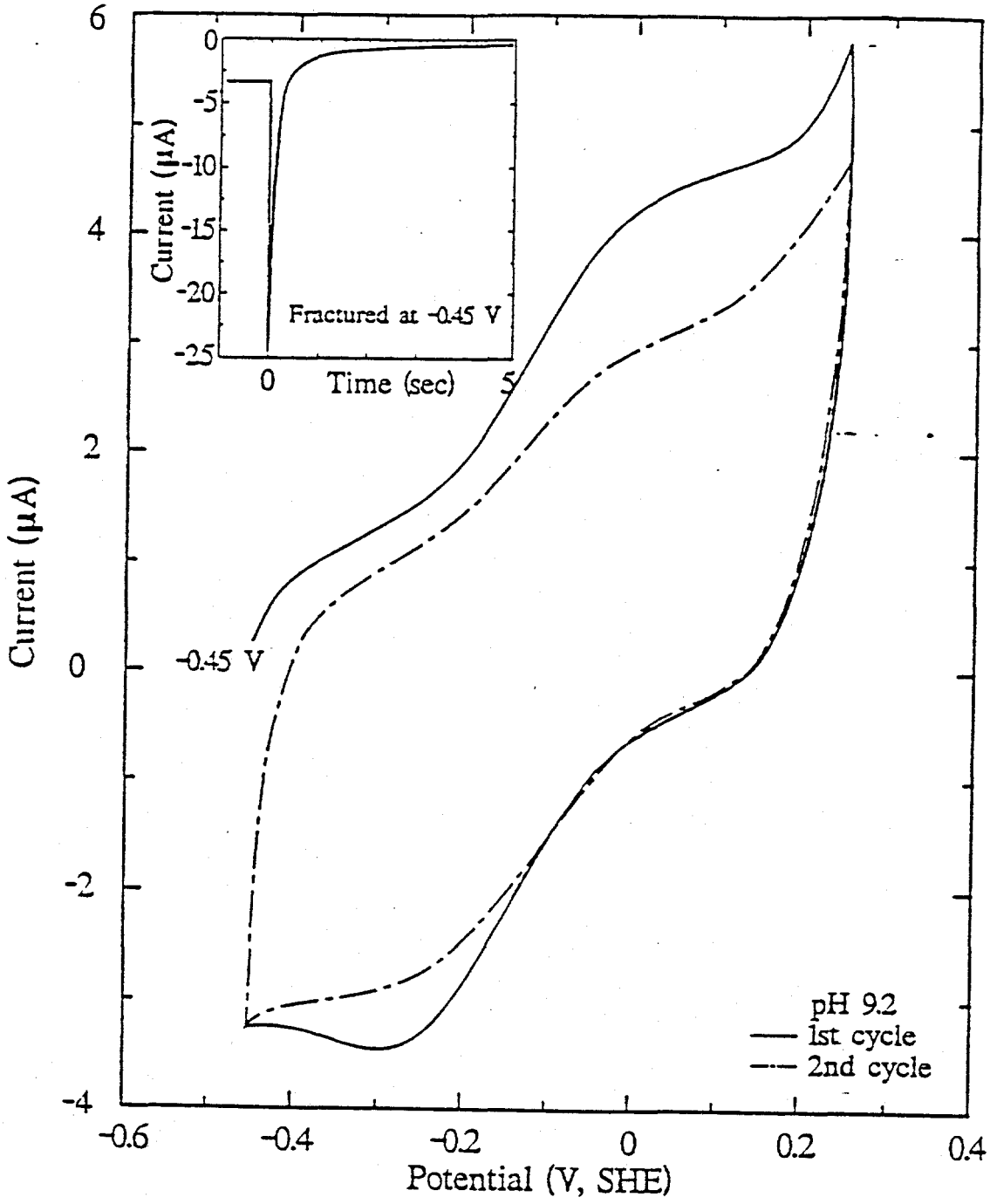

Figure 74. Voltammograms on Chinese coal-pyrite freshly fractured at -0.45 V at pH 9.2. The inset is the chronoamperometry curve upon fracture.

Similar studies were performed on mineral- and Pittsburgh No. 8 coal-pyrite. Mineral-pyrite exhibited electrochemical characteristics close to those observed with Chinese coal-pyrite, and its *stable* potential was at -0.28 V. An anodic peak at 0 V was also observed on the first sweep voltammogram at pH 9.2. Pittsburgh No. 8 coal-pyrite, however, was significantly different than the other two pyrite samples. It exhibited nearly zero current when fractured at about -0.15 V, rather than -0.28 V as observed with mineral- and Chinese coal-pyrite. This may suggest that Pittsburgh No. 8 coal-pyrite is already oxidized or that its stoichiometry is not identical to the other pyrites. In addition, voltammograms obtained on Pittsburgh No. 8 coal-pyrite after fracture differed remarkably in terms of the position of the peaks and their height, indicating the surface reactions on Pittsburgh No. 8 coal-pyrite may be different than on the other pyrites.

XPS study of the surface oxidation of Pittsburgh No. 8 coal-pyrite: The foregoing study of surface reactions on pyrite by cyclic voltammetry yielded detailed kinetic and mechanistic information on processes taking place on the mineral. However, electrochemical techniques lack the molecular specificity required to give unequivocal identification of the nature of species on the surface of electrodes. To complement electrochemical studies, X-ray photoelectron spectroscopy (XPS) was employed to provide information on the elemental and molecular composition of surface oxidation products of Pittsburgh No. 8 coal-pyrite.

XPS is one of the most widely used surface analysis techniques. It subjects the sample to monochromatized X-ray radiation and detects the photoemitted electrons. The observed photoelectrons come from the outermost 2-6 atomic layers, i.e., 5-40 Å, and carry information on the surface electronic structures and bonding. The value of the binding energy determines the type of atoms present in the solid and the chemical shifts give information on the chemical bonds of the elements, i.e., difference in the oxidation state, difference in molecular environment, and difference in

lattice site. Quantitative information on atomic ratios can be obtained by the analysis of the photoelectron emission intensities.

It has been well established (Buckley and Woods, 1987, Mycroft et al., 1990; Yoon et al., 1991) that the binding energy of the $S2p_{3/2}$ component of unoxidized pyrite is in the range of 162.2-162.4 eV while the corresponding value for bulk elemental sulfur is 163.5 - 164.0 eV; the binding energy of $Fe2p_{3/2}$ component of unoxidized pyrite is 707 - 707.5 eV. The peak at 168 or 169 eV in the S2p spectrum is characteristic of iron sulfate (Buckley and Woods, 1984; 1987). Yoon et al. (1991) also found a broad shoulder in the 710 - 715 eV in the Fe2p spectrum which is believed to represent the oxidized iron in the form of $Fe(OH)_3$, $FeO(OH)$, Fe_2O_3, Fe_3O_4, etc. Buckley and Woods (1984) reported that the three distinct binding energy regions in the O1s spectrum at about 530, 531 to 532 and near 533 eV are associated with oxide, hydroxide and chemisorbed oxygen species, and physically adsorbed water, respectively.

In the present work, XPS analysis has been carried out on Pittsburgh No. 8 coal-pyrite to better understand its oxidation. The surface of the coal-pyrite sample was wet polished with a 600 grit silicon carbide paper before being subjected to oxidation treatment. The oxidation was accomplished under different conditions, including (i) exposure to air for one hour, (ii) conditioning in aqueous solution at pH 9.2 at the open circuit potential for 10 minutes, and (iii) conditioning in aqueous solutions at pH 9.2 at 0.7 V for 10 minutes. For comparison, fresh coal-pyrite surfaces were also characterized. These were prepared by scraping the sample surface under ultra high vacuum (UHV) in a special scraping chamber of the XPS spectrometer. Figure 75 shows the S2p spectrum of coal-pyrite scraped under UHV. Unoxidized pyrite surfaces generally exhibit a well-resolved doublet composed of $S2p_{3/2}$ and $S2p_{1/2}$, which are separated by 1.2 eV with an intensity ratio of 2:1 (Buckley and Woods, 1987). In the S2p spectrum of this coal-pyrite sample, additional signals were observed on both sides

of the main S2p doublet. The spectrum can be fitted reasonably well with three different components. The main component shown by the most intense peaks at 162.5 eV and 163.7 eV is attributed to the $S2p_{3/2}$ and $S2p_{1/2}$ doublet from bulk FeS_2. An additional S2p doublet component on the lower binding energy side is apparent in Figure 75 with the $S2p_{3/2}$ peak at 161.5 eV. This peak was also observed by Mycroft et al. (1990) at 161.8 eV on a fresh mineral-pyrite surface. Buckley and Woods (1984) reported that unoxidized pyrrhotite exhibits a doublet with a $S2p_{3/2}$ component near 161.1 eV. Therefore, it is likely that the doublet with the $S2p_{3/2}$ component at 161.5 eV, which accounts for about 10% of the total S2p intensity, arises from an FeS-like species in the FeS_2 substrate. This FeS-like surface component on Pittsburgh No. 8 coal-pyrite may explain why freshly fractured electrodes of Pittsburgh No. 8 coal-pyrite exhibited zero-current upon fracture at -0.15 V while mineral- and Chinese coal-pyrites had zero-current at -0.28 V. The broad S2p doublet component in the 164-166 eV region may be attributed to energy loss of S2p electrons escaping from an unaltered pyrite surface (Buckley and Woods, 1987) and a possible residual effect due to inelastic scattering (Microft et al., 1990).

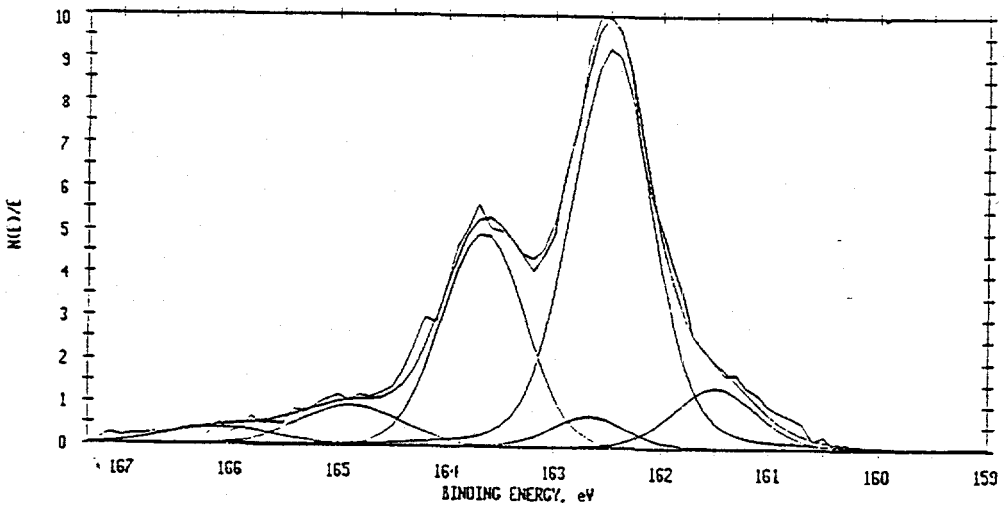

Figure 75. S2p spectrum of Pittsburgh No. 8 coal-pyrite scraped under UHV.

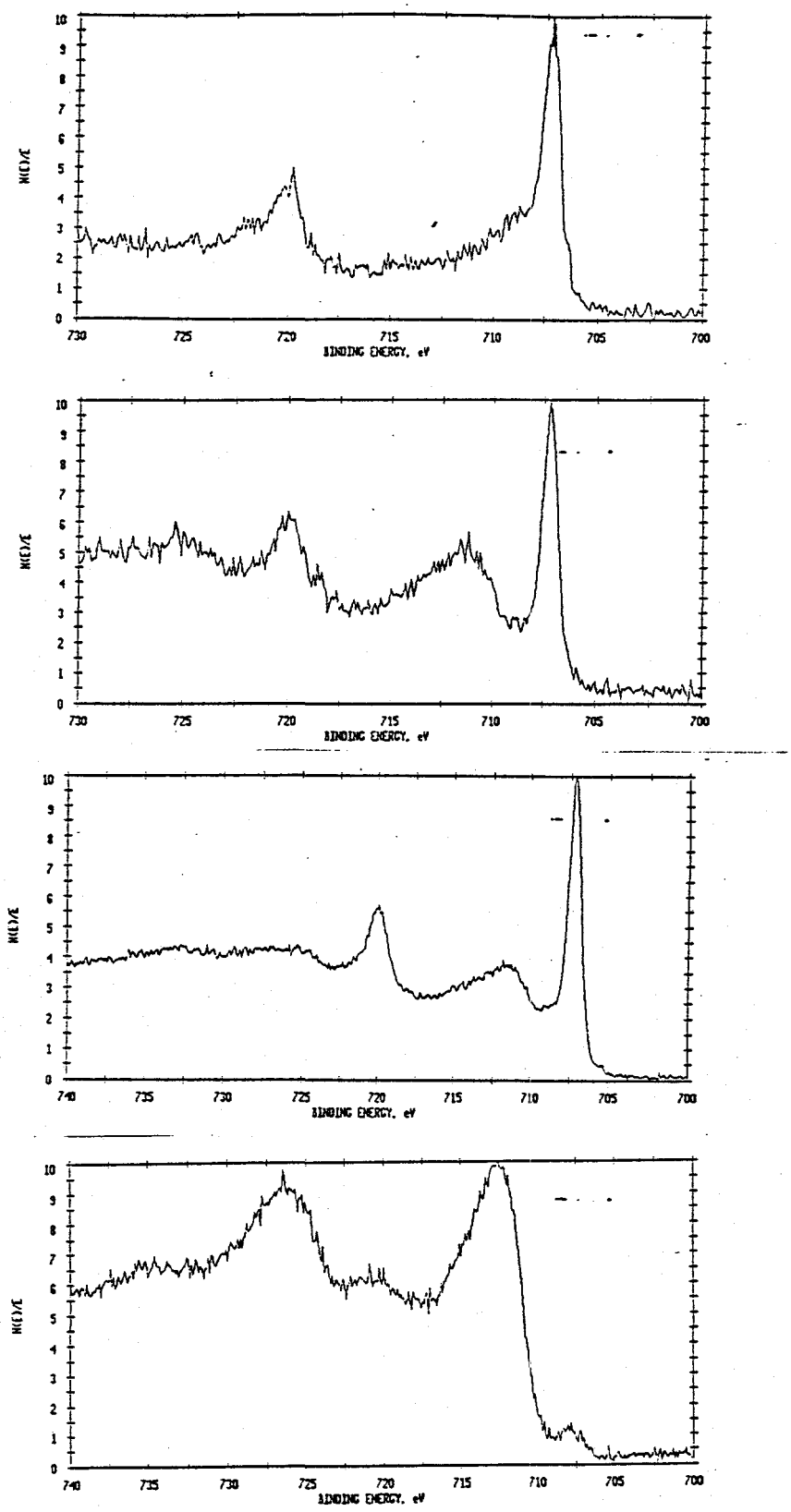

Figure 76. Fe2p spectrum of Pittsburgh No. 8 coal pyrite (a) scraped under UHV; (b) exposed to air for one hour; (c) oxidized at pH 9.2 at open circuit potential for 10 min; (d) same as (c) but at 0.7 V.

The Fe2p spectrum of the sample scraped under UHV (Figure 76a) showed a single doublet with the ($Fe2p_{3/2}$) component at 707.3 eV, indicative of FeS_2 based on previous studies (Buckley and Woods, 1987, Mycroft et al., 1990; Yoon et al., 1991). No discernible signals from iron oxidation products are present in the Fe2p spectrum, which is in good agreement with the results obtained by Buckley and Woods (1987) with fresh surfaces of mineral-pyrite. There is a small signal near 708 eV, which may be caused by the FeS-like species.

The fresh surface showed small amounts of oxygen and carbon contaminants. These contaminants were not observed on mineral-pyrite scraped under UHV. Oxygen and carbon contamination of the coal-pyrite sample may be associated with small amounts of coal inclusions in the sample. An appreciable amount of oxygen-containing species was reported on the fresh fracture surface of mineral-pyrite exposed to air for no more than a few seconds, and this species was identified to be chemisorbed water or hydroxide by Brundle et al. (1977).

Figure 77a shows the S2p spectrum for the Pittsburgh No. 8 coal-pyrite sample oxidized in air for one hour. Oxidation of the sample in air results in a decrease of the $S2p_{3/2}$ component at 161.5 eV, possibly due to the oxidation of the FeS-like surface species to FeS_2. The signal of the S2p doublet of the FeS-like product decreased to about 1% of the total S2p intensity. However, there is no indication for the formation of elemental sulfur or sulfate.

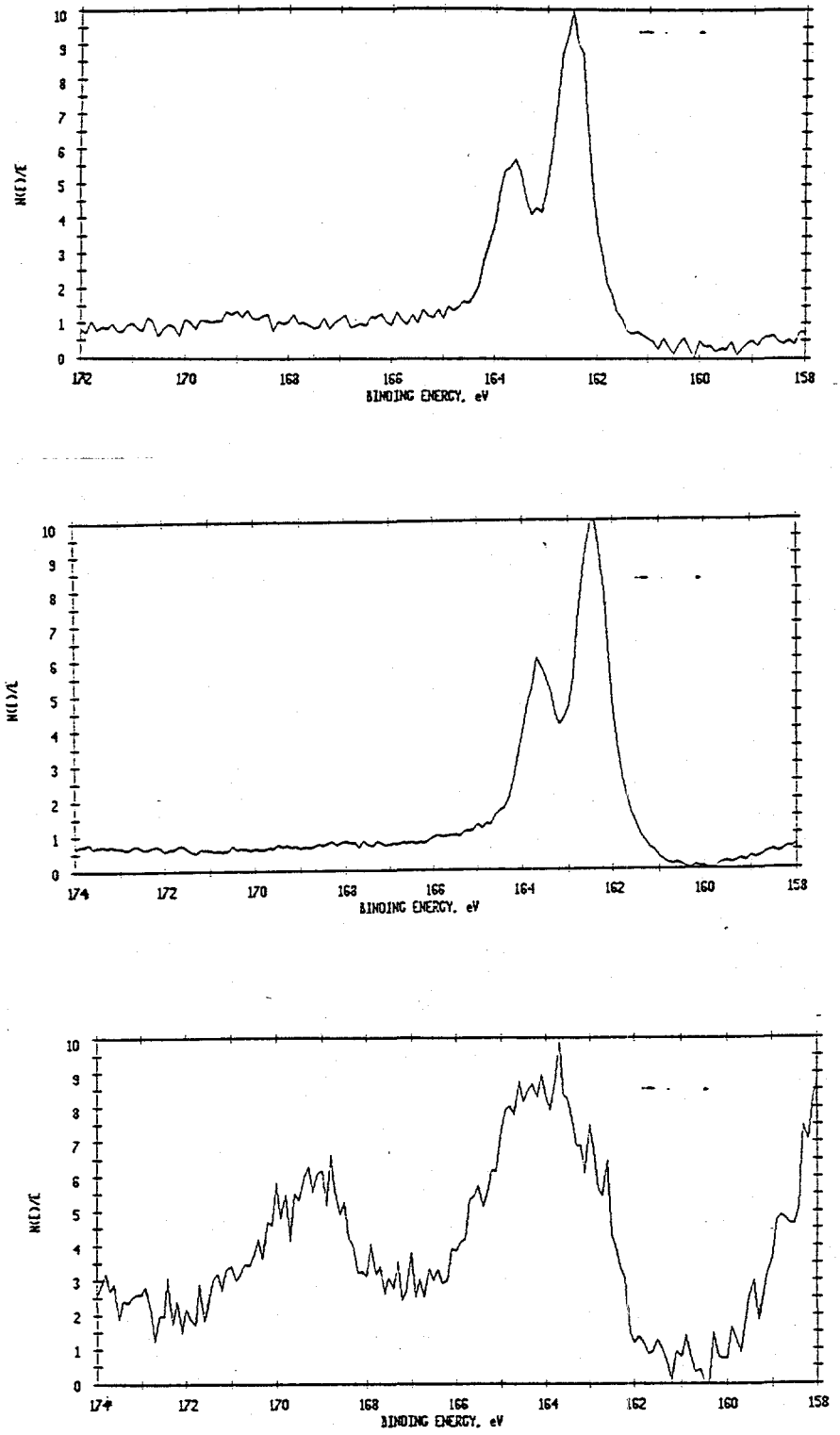

Figure 77. S2p spectrum of Pittsburgh No. 8 coal-pyrite oxidized (a) in open air for one hour; (b) in pH 9.2 solution at open circuit for 10 minutes; (c) in pH 9.2 solution at 0.7 V for 10 minutes.

The Fe2p spectrum shows a new component at around 711.5 eV (Figure 76b) which indicates the presence of iron oxide and/or iron hydroxy-oxide (Brion, 1980; Harvey and Linton, 1981; Baltrus and Proctor, 1990). This is confirmed by the shift of the O1s peak to a lower binding energy. The same behavior was exhibited by mineral-pyrite surfaces that were abraded under oxygen-free water, dried, and then exposed to air (Buckley and Woods, 1987). Theoretically, the oxidation of the iron component of pyrite must be accompanied with a change in the oxidation state of the sulfur component. The absence of sulfur oxidation products suggests that iron oxides or hydroxides are formed during wet-polishing while sulfate produced is dissolved. Iron oxides and hydroxides may passivate the surface and inhibit the oxidation of pyrite on exposure to air.

Freshly fractured mineral-pyrite surfaces oxidized under similar conditions were reported to have spectra that are considerably different from those shown above. Buckley and Woods (1987) found that exposure of a fresh fracture surface to ambient air at 65% relative humidity and 295 K for a few days produced a peak near 168.5 eV in the S2p spectrum, which they attributed to sulfate, and new intensity at 711 eV in the Fe2p spectrum, which they identified as ferrous sulfate rather than hydrated iron oxide. The onset of sulfate formation was apparent in spectra from fracture surfaces exposed to air for a few minutes. The formation of iron oxide, most probably hydrated, was barely evident on the surface of pyrite exposed to air for 14 days.

Pittsburgh No. 8 coal-pyrite treated in pH 9.2 aqueous solutions at open circuit showed an S2p spectrum (Figure 77b) similar to that observed with the sample oxidized in air for one hour (Figure 77a). No sulfur oxidation products other than FeS-like species are evident in Figure 77b. On the other hand, the corresponding Fe2p spectrum shown in Figure 76c also exhibits a component near 711.5 eV, indicating the existence of iron oxides or hydroxides. The O1s and C1s spectra are almost identical to those for the sample oxidized in air for one hour. It is very likely that the sulfur component in pyrite

was oxidized to sulfate that dissolved in solutions. These results suggest that the degree of oxidation obtained in air for one hour is similar to that achieved in pH 9.2 aqueous solutions at the open circuit potential for 10 minutes, which appears to confirm the preceding postulation that iron oxides or hydroxides produced during polishing hinders further oxidation of pyrite due to the formation of a passivating layer.

Figure 76c shows the S2p spectrum of Pittsburgh No. 8 coal-pyrite oxidized at 0.7 V in aqueous solutions of pH 9.2 for 10 minutes. The spectrum is significantly different from that of the fresh surface. The difference arises from aggressive oxidation of the mineral at 0.7 V. The S2p line is shifted to higher binding energy due to surface charging caused by the formation of an insulating oxidation product overlayer. The spectrum can be curve-fitted with at least three doublets which are different from those obtained for the fresh surface shown in Figure 75. The doublet on the low binding energy side, with a corrected binding energy for $S2p_{3/2}$ of 162.4 eV, is characteristic of pyritic sulfur. The presence of elemental sulfur is indicated by the doublet with a corrected $S2p_{3/2}$ component at 164.1 eV. The third doublet is between those for pyritic and elemental sulfur, which can be attributed to the formation of polysulfides. There is also another component observed at 168.5 eV that indicates the presence of iron sulfate.

It is interesting to note that after warming the sample overnight to about 300 K, the intensity associated with the $S2p_{3/2}$ component at 164.1 eV decreased from 23% to about 17% of the total sulfur intensity, which confirms that this doublet arises from volatile elemental sulfur. There are no changes in the spectrum for the other sulfur components except for the loss of surface charging.

The corresponding Fe2p spectrum obtained after oxidation at 0.7 V for 10 minutes, as given in Figure 77d, shows a substantial decrease in the FeS_2 component represented by $Fe2p_{3/2}$ at 707.4 eV, while the iron oxide, iron hydroxide and iron sulfate species indicated by the $Fe2p_{3/2}$ component in the

711 to 713 eV region increased sharply. The presence of iron sulfate is confirmed by the S2p and O1s spectra and the presence of the iron oxide and/or iron hydroxide is substantiated by the O1s spectrum.

The above data indicates that Pittsburgh No. 8 coal pyrite is aggressively oxidized at 0.7 V to iron oxides or hydroxides, iron sulfate, elemental sulfur and polysulfides. While the formation of polysulfides or a metal-deficient region on mineral-pyrite under alkaline conditions has been reported previously (Buckley and Woods, 1984; 1987; Mycroft et al., 1990; Yoon et al., 1991), elemental sulfur has not been observed before on other pyrites by XPS. Both elemental sulfur and polysulfides are hydrophobic species that are able to induce surface hydrophobicity on pyrite. The presence of iron oxides and sulfates, on the other hand, would tend to render the mineral hydrophilic. The decrease in the floatability of pyrite at high positive potentials in alkaline solutions is attributed to the high abundance of iron oxides or hydroxides rather than the lack of hydrophobic products. These XPS results are in good agreement with those derived from electrochemical studies.

Task 4 - In Situ Monitoring of Reagent Adsorption on Pyrite

Subtask 4.1: Mechanistic Studies of Reagent Adsorption on Pyrite

The adsorption behavior of kerosene, hexane, methyl isobutyl carbinol (MIBC), M-150 frother, and a polymeric depressant (S7261) on pyrite were studied by Fourier Transform Infrared (FTIR) spectroscopy. The spectroscopic measurements were carried out on mineral pyrite conditioned in sodium borate buffer solutions (pH 9.2), except for S7261 which used a pH 6.8 buffer solution. The infrared reflection absorption spectroscopic (IRRAS) technique was used to monitor the reagent adsorption at different potentials. A pure pyrite specimen in the form of a 40 x 10 x 5 mm plate was used in the spectroscopic measurements.

In all adsorption experiments except those using S7261, the pyrite sample was held at the starting potential of -0.4 V (SHE) for one minute, then the potential was stepped to the desired

potential and held for five minutes. With the S7261 polymer, the starting potential used was the rest potential (about 0.24 V). The sample was then withdrawn from the electrochemical cell, rinsed with deionized water, dried and transferred to the spectrometer.

No adsorption of kerosene, MIBC, hexane, and M-150 on pyrite was observed over the entire potential range studied (-0.4 to 0.4 V). However, the absence of any indication of adsorption from the FTIR data does not mean that these reagent do not adsorb on pyrite. It is possible that these reagents were weakly physisorbed on the mineral surface and were readily removed by the rinsing. The weak physisorption of kerosene and MIBC was indicated by the contact angle data provided in Subtask 4.2. There was an increase in contact angle, a measure of hydrophobicity, at lower potentials in the presence of these reagents. The increase in hydrophobicity may be explained by the physical adsorption of these reagents.

The FTIR spectra obtained for pyrite conditioned in 60 ppm polymer S7261 at pH 6.8 at different potentials are shown in Figure 78. The adsorption of the polymeric depressant is indicated by the absorption peaks at 1243, 1166, 1027 and 905 cm^{-1}. These peaks are characteristics of C=S, C-S and C-N-S vibrations. The absorption peak at 1097 cm^{-1} is due to the S-O vibrations from the oxidation products of pyrite. Figure 79 shows the IR signal intensity of S7261 adsorbed on the pyrite sample as a function of the conditioning potential. It appears that reducing potentials are preferred for the adsorption of polymer S7261. This possibly indicates that cathodically treated surfaces of pyrite can react more readily with the polymer than oxidized surfaces covered by iron hydroxides. It is also interesting to point out that the peak at 1097 cm^{-1} is observed here but not in the spectra obtained in the other experiments using kerosene, hexane, MIBC or M-150. This may partly explain the observed difference in hydrophobicity with the use of these reagents.

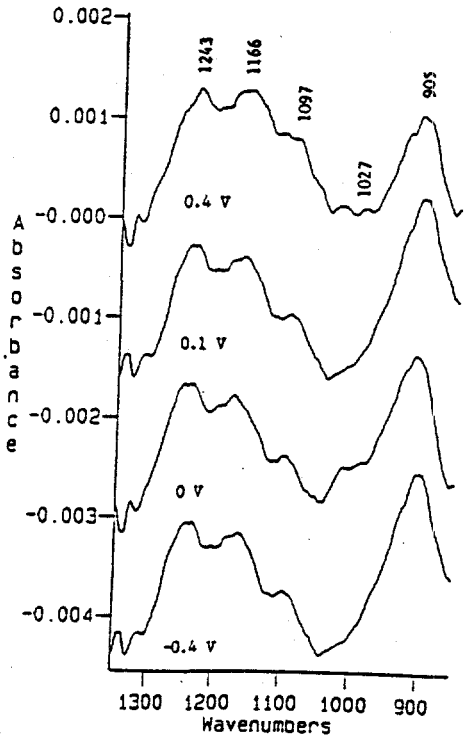

Figure 78. Effect of potential on IR signal intensity of S7261 adsorbed on pyrite conditioned in 60 ppm S7261 solution at pH 6.8.

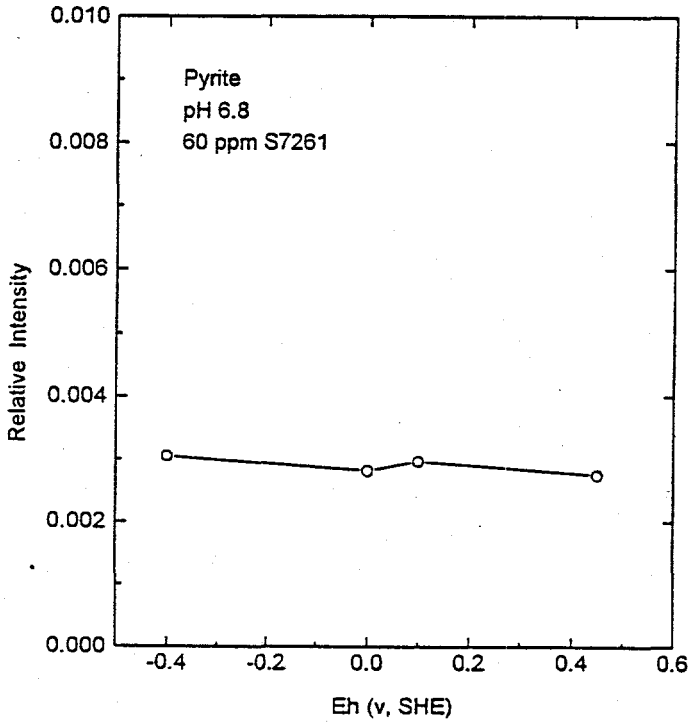

Figure 79. FTIR spectra of pyrite conditioned in 60 ppm S7261 at pH 6.8 and different potentials.

Subtask 4.2: Contact Angle Measurements of Reagents on Pyrite Surfaces

Contact angles have been measured on mineral pyrite in order to further understand the adsorption of the reagents on pyrite. The reagents studied included two frothers (MIBC and M150), two collectors (kerosene and hexane) and one polymeric depressant (S7261 from Cytec).

Figure 80 shows the contact angle as a function of electrochemical potential for the sodium tetraborate buffer solution (pH 9.2) containing MIBC and M150. In the buffer solution alone, a finite contact angle develops on pyrite at potentials above -0.3 V (SHE). The potential where a finite contact angle is observed is in good agreement with the potential at which pyrite first begins to oxidize, as discussed in Subtask 3.3, and with the lower flotation edge of pyrite (see Figs. 75 and 76 below). The decrease in the contact angle at potentials >0.2 V is also consistent with the decrease in recovery (Figs. 75 and 76) at higher potentials.

In the presence of MIBC, a finite contact angle appears to develop on pyrite at a lower potential than in the buffer solution alone. This may indicate some adsorption of the MIBC. Interestingly, the M150 frother shifts the potential where a finite contact angle is developed to more positive potentials. This may indicate that this frother adsorbs more strongly on pyrite than MIBC and inhibits its oxidation.

Figure 81 shows the effect of kerosene, hexane and S7261 on the contact angle of pyrite. Kerosene appears to induce a finite contact angle on pyrite even at negative potentials where it is known that pyrite does not float. This indicates a potential-independent adsorption of a component of the kerosene. On the other hand, the contact angle in the presence of hexane is nearly identical to that in the buffer, indicating no adsorption.

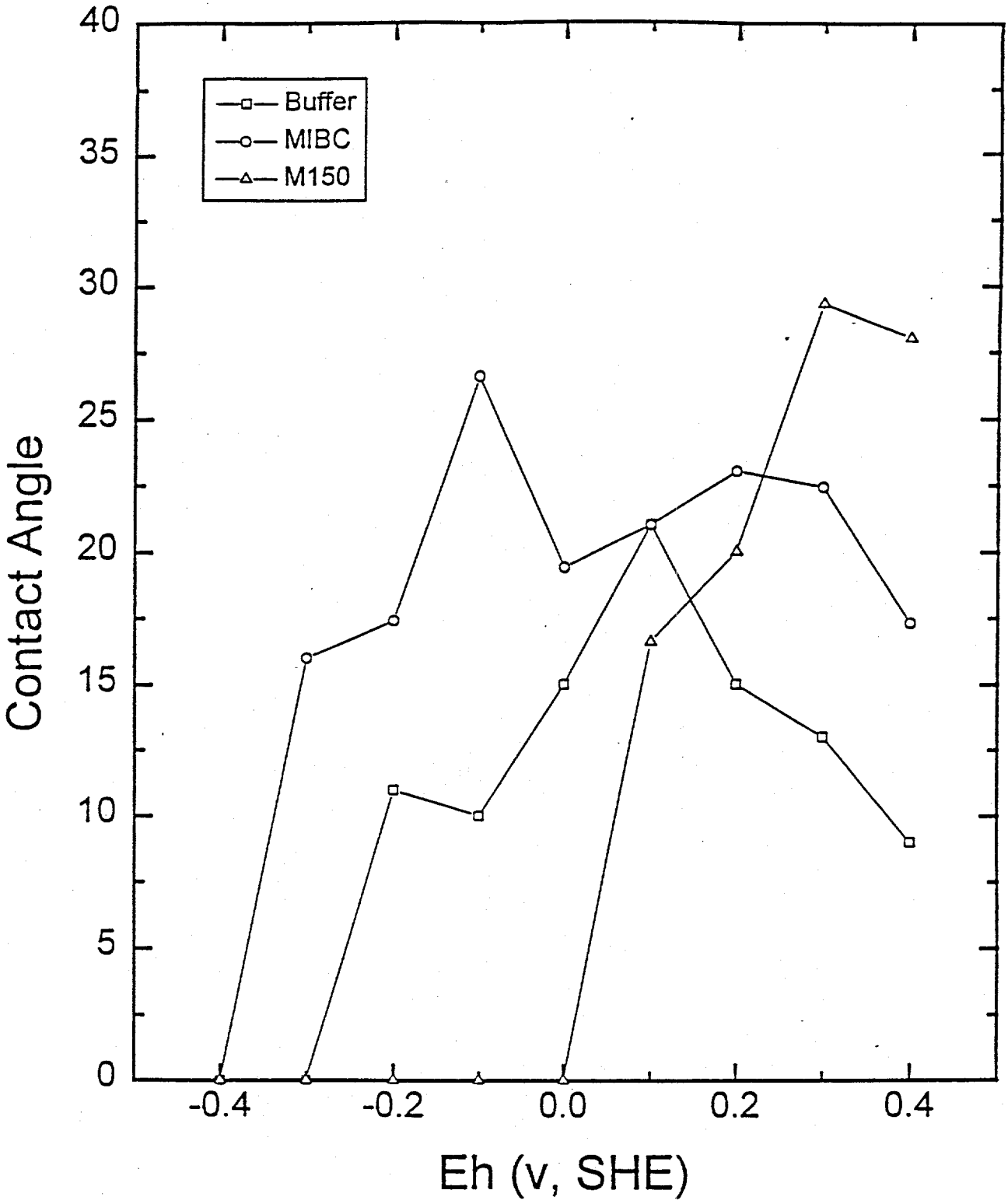

Figure 80. Contact angle as a function of electrochemical potential for mineral pyrite in a sodium tetraborate buffer and in the buffer containing the frothers MIBC and M150.

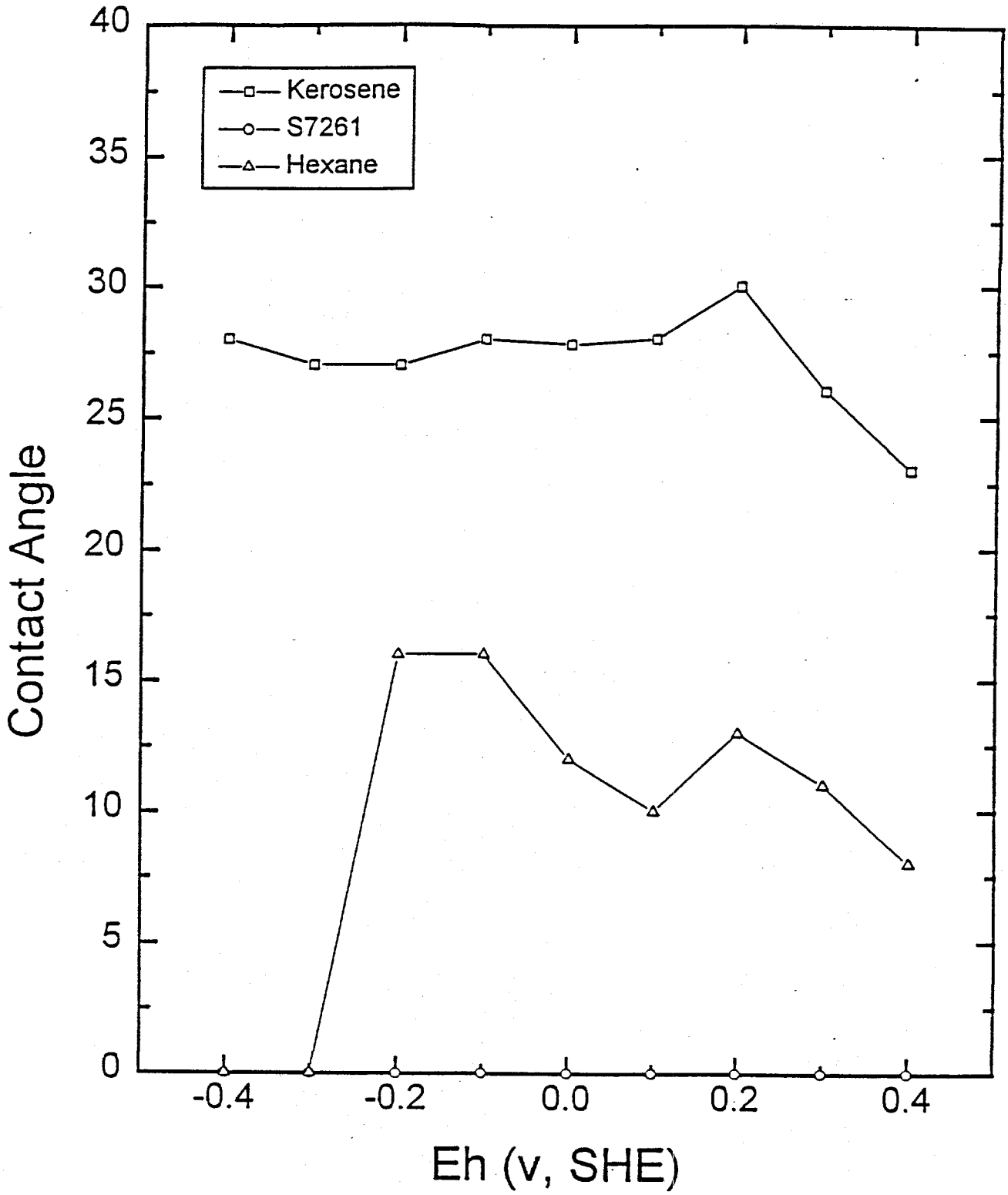

Figure 81. Contact angles as a function of electrochemical potential for mineral pyrite in the presence of kerosene, hexane, and the polymeric depressant S7261.

In the presence of the polymeric depressant S7261, the contact angle on pyrite is zero and it is independent of potential. This indicates strong adsorption of the polymer. The zero contact angle must be the result of the hydrophilic groups attached to this polymer.

Task 5 - Bench Scale Testing of the EESR Process

Subtask 5.1: Microflotation Tests

A series of microflotation tests was conducted to evaluate the effect of electrochemical potential (E_h) on pyrite floatability at various solution pH's. The potential of pyrite was controlled either by a potentiostat or by the addition of hydrazine and sodium sulfide as reducing agents and potassium permanganate as an oxidizing agent.

Figure 82 shows the flotation recovery of mineral pyrite at several pH's as a function of potential adjusted by the addition of reagents. Illinois No. 6 coal-pyrite exhibited similar behavior, although flotation recoveries were lower. It is clear that the floatability of pyrite is dependent on potential and solution pH. Pyrite exhibits maximum flotation recovery over a narrow potential range. Figure 83 shows similar results obtained in the electrochemical-microflotation cell in which the bed potential was controlled by a potentiostat. The lower and higher flotation edges are, respectively, -0.3 V and 0.4 V at pH 9.2, 0.1 V and 0.8 V at pH 4.6. The flotation results appear to be in good agreement with the known electrochemistry of pyrite oxidation. It has been suggested in Subtasks 3.1 and 3.3 that elemental sulfur (S^o), metal-deficient sulfide ($Fe_{1-x}S_2$, $x < 1$) or polysulfide (FeS_n, $n > 2$) are produced *via* reactions (10) - (12). These sulfur-rich surface species are naturally hydrophobic and can render the mineral floatable. The lower flotation edge clearly defined in Figure 83 corresponds well to the potential at which incipient oxidation of pyrite occurs. The upper flotation edge is determined by reaction (9), which represents the aggressive oxidation of pyrite to ferric hydroxide and sulfate.

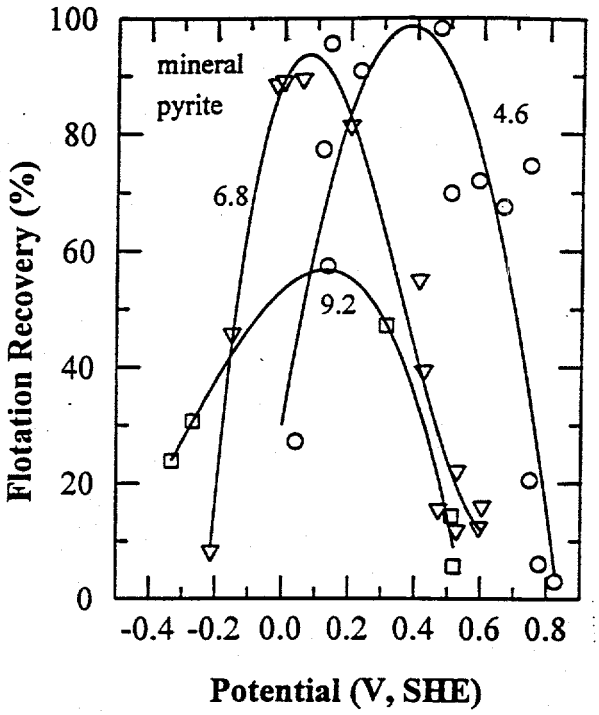

Figure 82. Flotation recovery of 100 x 200 mesh mineral-pyrite as a function of pyrite potential at different pH's.

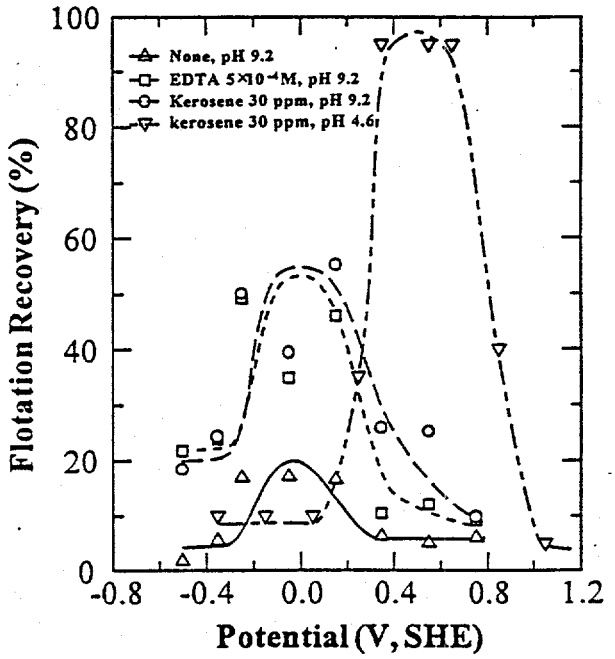

Figure 83. Flotation recovery of 65 x 100 mesh mineral-pyrite as a function of potential at pH 4.6 and 9.2.

Figures 82 and 83 also show that the flotation recovery is generally lower at pH 9.2 than at pH 4.6. As the solution pH increases, more ferric hydroxide is formed on the surface of pyrite, which suppresses its hydrophobicity. Ahlberg et al. (1990) and Pang and Chander (1993) reported a substantial increase in pyrite floatability at pH 9.2 and 11 when an iron chelating agent, EDTA, was used to remove ferric hydroxide from the surface of pyrite. This is in agreement with the electrochemical-microflotation tests shown in Figure 83, which shows that EDTA dramatically increased the floatability of mineral-pyrite in pH 9.2 solution. Figure 83 also indicates that the use of kerosene in coal flotation will lead to a pronounced increase in unwanted pyrite recovery. Olson and Aplan (1987) reported that an oil dosage of 0.35 kg/ton promoted the flotation of clean coal by a factor of 3 and that of pure pyrite by a factor of 30. It is believed that moderate hydrophobicity of coal-pyrite induces a hydrophobic interaction (Xu and Yoon, 1989) between pyrite and kerosene which, in turn, considerably increases the hydrophobicity of pyrite.

Mineral-pyrite exhibits stronger floatability than Illinois No. 6 coal-pyrite. Mineral-pyrite showed almost 100% recovery at pH 4.6 and 6.8 while recovery of coal-pyrite was less than 25% (not shown). The lower floatability of coal-pyrite indicates that there are more hydroxides on its surface due to oxidation. As discussed in Task 3, Pittsburgh No. 8 coal-pyrite produced lower amounts of soluble iron-hydroxyl species compared to mineral-pyrite; Coal-pyrite is poorly crystallized and possesses more defects on the surface. Consequently, it oxidizes faster than mineral-pyrite and metastable hydrophobic sulfur species may be more readily transformed to soluble sulfate, increasing the net hydrophilicity of the surface (Tao et al., 1993, Zhu et al., 1991).

Subtask 5.2: Galvanic Control Using Metal and Alloy Powders

An important conclusion that can be drawn from the above study is that pyrite can be depressed under reducing or strongly oxidizing conditions; however, oxidizing conditions are not

preferred for coal-pyrite depression because they also oxidize coal, thus decreasing its floatability and reducing the separation efficiency. Sadowski et al. (1988) studied the behavior of Upper Freeport coal and found that the oxidation of coal gradually increased both the carboxyl and hydroxyl concentration on the coal surface and reduced the hydrophobicity of coal. Therefore, reducing conditions may be more appropriate for enhancing pyrite rejection. Work described in Subtask 3.2 has shown that galvanic coupling of pyrite with reactive metals can considerably reduce the potential of pyrite.

Microflotation tests were conducted to determine the most effective sacrificial anode material to depress pyrite. Pyrite was conditioned with metal powders (minus 325 mesh) for 10 seconds prior to flotation. Figure 84 shows the effect of galvanic coupling with Mn and Zn on the potential and floatability of Illinois No. 6 coal-pyrite at pH 4.6. As shown, pyrite was effectively depressed by galvanic contact with the metals. In the absence of metal powders, the coal-pyrite exhibited a flotation recovery of 73%. With the addition of Mn and Zn powders, the coal-pyrite showed only negligible floatability.

Of the anodes examined in the present work (Zn, Mn, Fe, Al and several alloys), zinc was the most effective for depressing pyrite, although it did not lower the potential of pyrite as much as manganese. This may be due to the lower solubility of $Zn(OH)_2$ ($K_{sp} = 7.18\times10^{-17}$) compared to $Mn(OH)_2$ ($K_{sp} = 2.04\times10^{-13}$), leading to a higher degree of passivation. During galvanic interaction, metal ions released from the anode by oxidation may migrate to the cathode to combine with OH^-, forming hydroxides, as suggested by Kuhn and Chan (1983). Such hydrophilic coatings may aid in depressing pyrite. It is believed that galvanic coupling of pyrite with active metals depresses pyrite through two important mechanisms: 1), decreasing the pyrite potential to a value negative enough to prevent superficial oxidation and/or reducing hydrophobic species already present on the surface, and

2), preferentially forming metal hydroxides on the surface by the generation of hydroxyl ions, i.e., reaction (17).

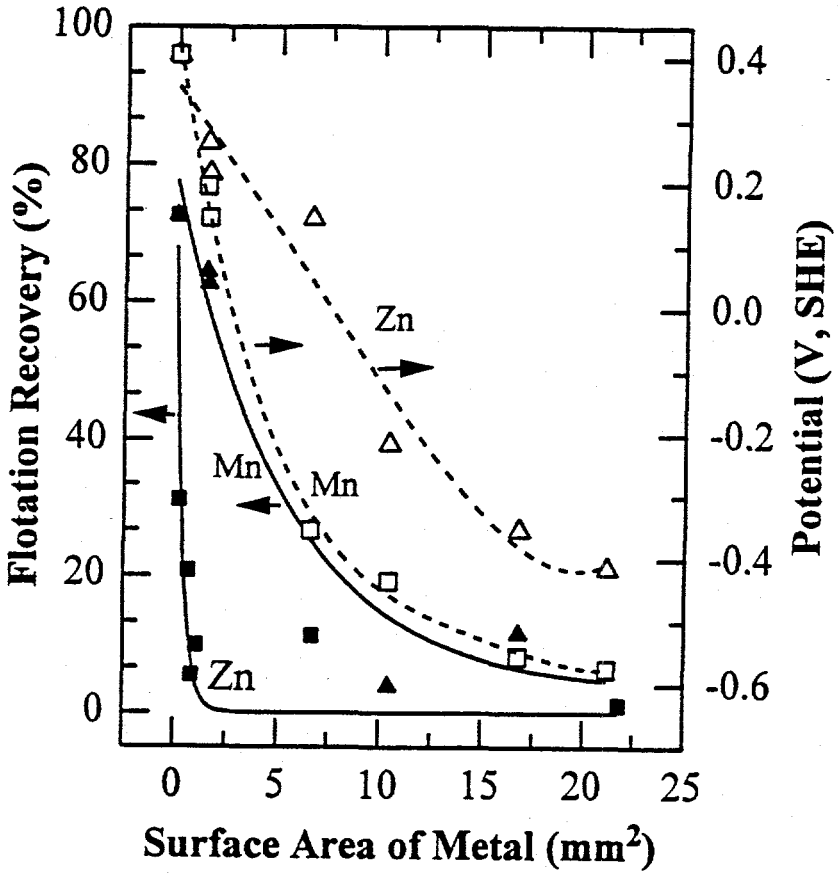

Figure 84. The effect of the surface area of manganese and zinc powders on the flotation and electrochemical potential of 100 x 200 mesh Illinois No. 6 coal-pyrite at pH 4.6.

Subtask 5.3: Galvanic Control Using Sacrificial Anodes

An experimental design was developed to optimize bench-scale flotation conditions for highest sulfur rejection. Operating parameters to be optimized included pulp density and dosage of sacrificial anodes. Zinc was found in Subtask 5.2 to be the most effective sacrificial anode and was employed in this task. Three levels, designated as high, intermediate and low, were selected to provide 10, 15, and 20 weight percent solids for the first parameter and 0.6, 1, and 1.4% relative to the feed solids for the second. The operating conditions for each test are summarized in Table 28. It should be pointed out that the powder dosage was lower than originally estimated and suggested in the test plan. This is because later experiments showed that lower Zn powder concentration effectively reduced the potential. In addition, the Zn powders were found to float. High dosages may significantly increase the ash content in the froth product and damage the reliability of the flotation results. All flotation tests were conducted in a 3/4"-diameter column. The minus 100 mesh Pittsburgh No. 8 and Illinois No. 6 coals were used for evaluation of the EESR process for improving sulfur rejection.

Figures 85 and 86 show the flotation results of Pittsburgh No. 8 coal obtained with and without galvanic coupling with Zn powder. It can be seen from Figure 85 that the total sulfur rejection can be increased by 10 - 15% by the galvanic coupling at the same combustible recovery. The biggest improvement in total sulfur rejection, i.e., about 20%, was achieved at the highest dosage of Zn. Figure 86 shows the relationship between the combustible recovery and the pyritic sulfur rejection. The scatter in the data is more pronounced than shown in Figure 85, possibly due to the fact that analysis of pyritic sulfur is not as accurate and reliable as that of total sulfur. Nevertheless, Figure 86 confirms that a significant improvement in pyritic sulfur rejection can be obtained by using Zn powder. It should be pointed out that all data points fall on the same curve of combustible recovery vs. ash rejection (not shown). This indicates that the difference observed in Figures 85 and 86 is indeed caused

by the decreased floatability of pyrite, not by increased ash content as a result of the addition of metal powders.

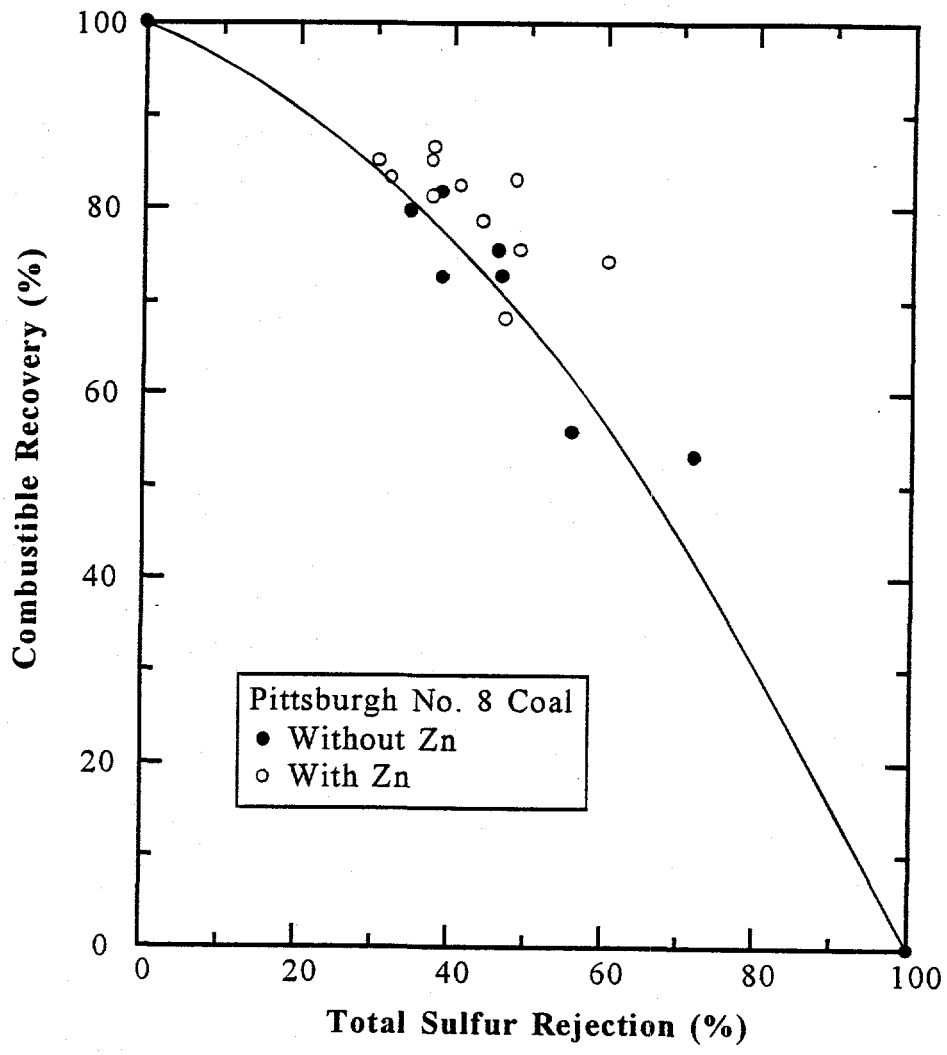

Figure 85. The improvement of total sulfur rejection with Pittsburgh No. 8 coal achieved by the use of Zn powders.

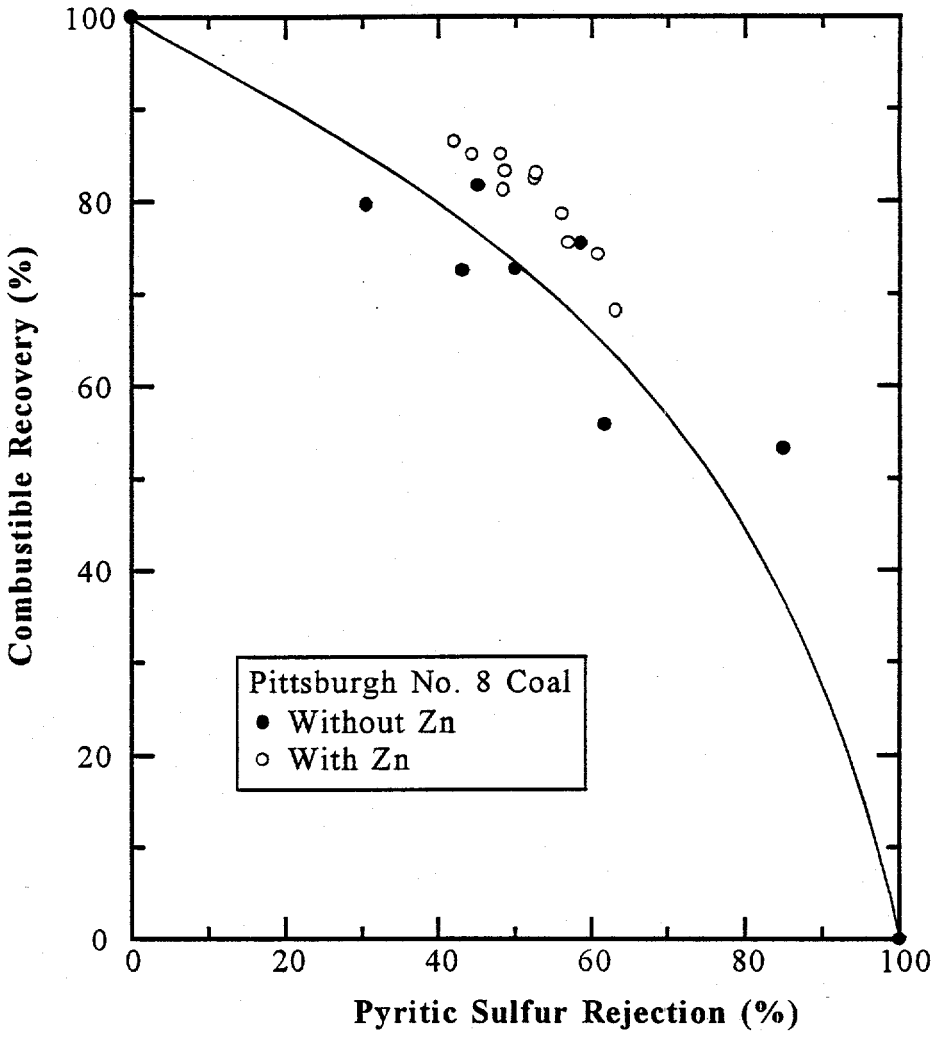

Figure 86. The improvement of pyritic sulfur rejection with Pittsburgh No. 8 coal achieved by the use of Zn powders.

Table 28. Operating conditions of flotation tests for evaluating the EESR process.

Run Order	X1 Solids (weight %)	X2 Powder (weight %, relative to solids)
1	20	1.4
2	15	0.2
3	15	1.0
4	15	1.0
5	10	0.6
6	15	1.0
7	20	0.6
8	15	1.8
9	15	1.0
10	10	1.4
11	25	1.0
12	5	1.0
13	15	1.0

Figures 87 and 88 show combustible recovery vs. total sulfur rejection and combustible recovery vs. pyritic sulfur rejection, respectively, for Illinois No. 6 coal obtained in the presence and absence of Zn powders. The data points appear to fall on the same curves, which indicate that galvanic coupling did not improve the rejection of pyrite for this specific coal. This is consistent with the fact that pyrite in the Illinois No. 6 coal is not as well liberated as in the Pittsburgh No. 8 coal and there are greater quantities of pure or nearly pure coal particles in the Pittsburgh No. 8 coal, as shown by the image analysis results described in Subtask 2.2. The floatability of pure or nearly pure coal particles would not be affected by galvanic coupling. The high concentration of middling particles in the Illinois No. 6 coal increased the difficulty in demonstrating the improvement in sulfur rejection that can be achieved by the EESR process.

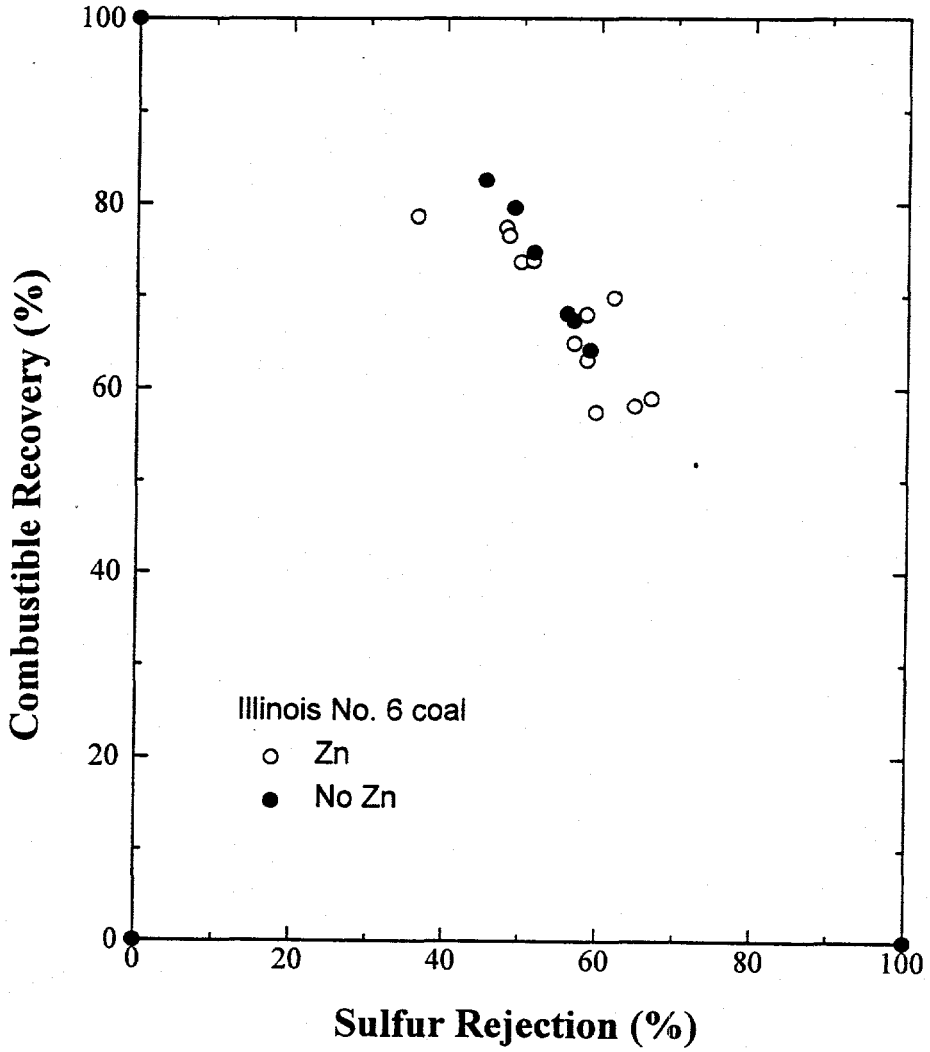

Figure 87. The relationships between combustible recovery and total sulfur rejection of Illinois No. 6 coal with or without Zn powders.

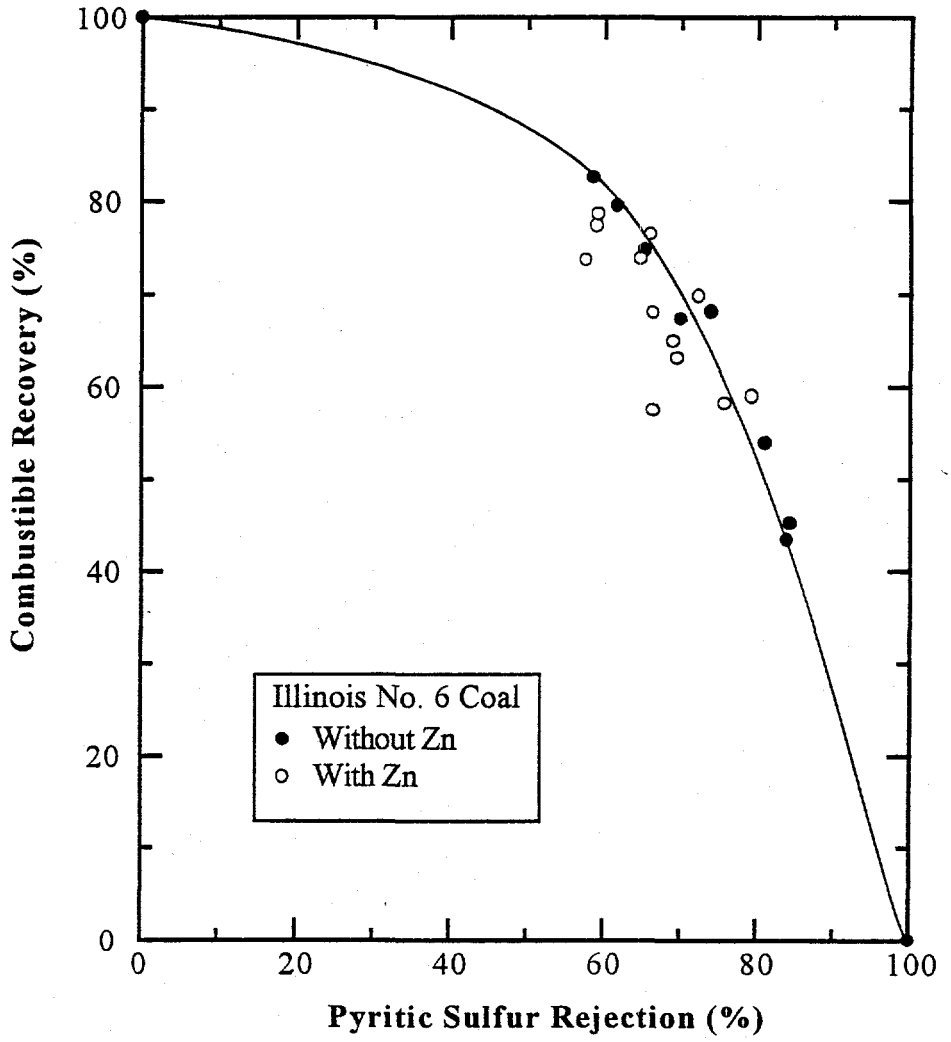

Figure 88. The relationships between combustible recovery and pyritic sulfur rejection of Illinois No. 6 coal with or without Zn powders.

Task 6 - Bench-Scale Testing of the PESR Process

Subtask 6.1: Microflotation Tests

One of the most important mechanisms of pyrite recovery in coal flotation is related to pyrite-coal composite particles resulting from incomplete liberation. It was observed by Wang et al. (1993) that composites containing small amounts of coal had flotation behavior resembling coal rather than pyrite. Oblad (1985) reported that all pyrite particles recovered in the froth product had coal on the surface, and those remaining in the tailings were free of coal. It appears necessary to mask the carbonaceous component of middlings to obtain effective depression.

Polymers are commonly used as flocculants in mineral and coal processing processes but their applications as depressants are scarce, especially for sulfide minerals. Griffith and Parkinson (1975) reported that acrylamide polymers can be employed as gangue depressants in cassiterite ore flotation. Recently, Nagaraj et al. (1992) showed that some functionalized synthetic polymers sharply decreased pyrite flotation recovery. This is attributed to the incorporation of sulfide-specific functional groups into these hydrophilic polymers which strongly adsorb on the mineral surface and provide more hydrophilic sites. However, polymer depressants have not been studied for pyrite-coal composite particles. If functional groups in the polymer react with pyrite, the hydrophilic polymer chains may be able to stretch over the coal inclusions, rendering pyrite-coal composites hydrophilic.

Four functionalized synthetic polymers have been developed recently by CYTEC Industries (formerly American Cyanamid). They were dissolved in water and emulsified to make 3% aqueous solutions prior to use. The polymers were tested on freshly-ground 100 × 200 mesh mineral-pyrite and 100 × 200 mesh Pittsburgh No. 8 coal at pH 6.8. In each test, diluted and emulsified polymer was added directly to the microflotation cell and conditioned for 1.5 minutes before the addition of kerosene. Figure 89 shows the effect of polymer dosage on the flotation of coal and pyrite. Dosages

of 50 to 100 g/ton are sufficiently high for effective depression of pyrite and higher dosages do not offer much additional benefits. With the exception of polymer S7261, these polymers also reduced the floatability of coal even at relatively low dosages. Polymer S7261 exhibited significant depression effect on pyrite and marginal adverse influence on coal floatability at dosages of less than 100 g/ton and is clearly the most appropriate for use in coal flotation.

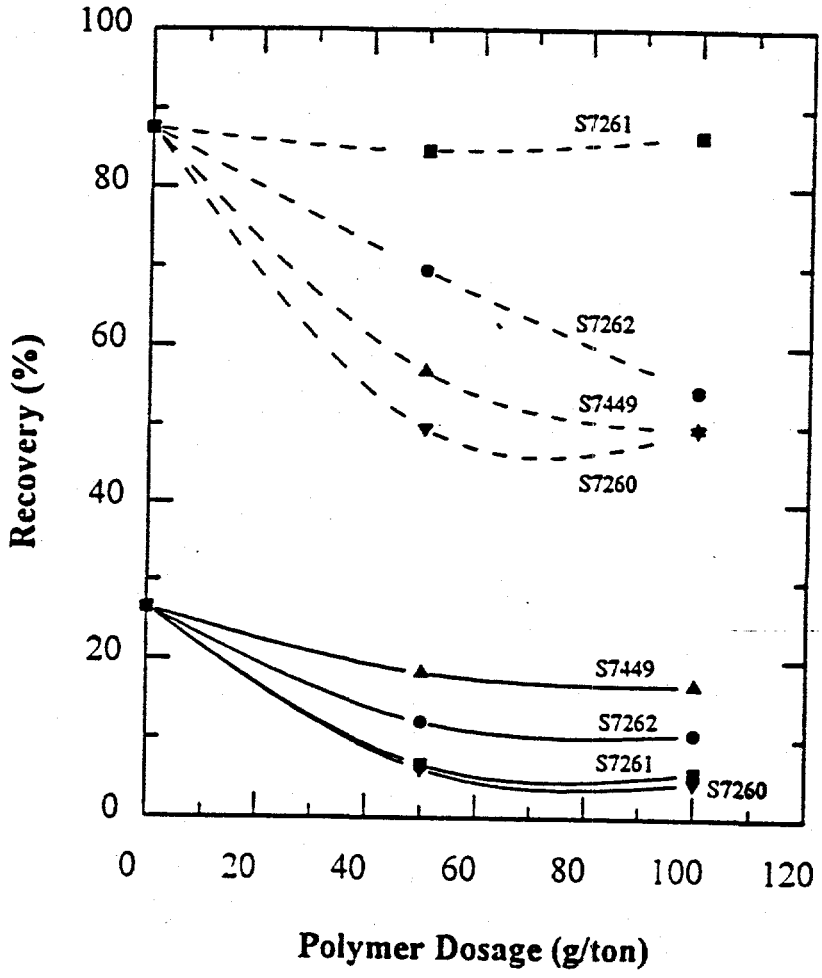

Figure 89. The effect of polymer dosage on the flotation recovery of 100 x 200 mesh mineral-pyrite (solid line) and Pittsburgh No. 8 coal (dashed line) at pH 6.8.

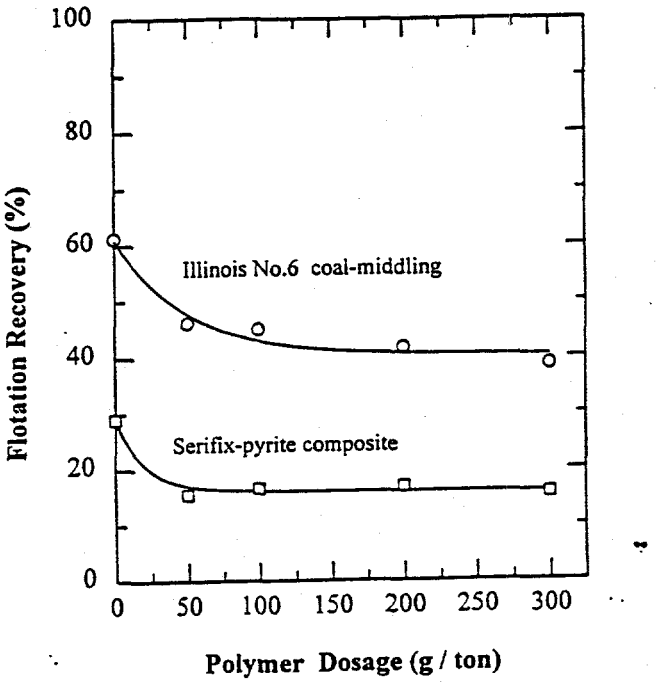

Figure 90. The effect of polymeric depressant S7261 on the recovery of Illinois No. 6 middlings and on Serifix-pyrite synthetic composite middlings at pH 6.8.

The results of microflotation tests on Illinois No. 6 coal-pyrite middlings and Serifix-pyrite composites using polymer S7261 at pH 6.8 are given in Figure 90. A dosage of 50 g/ton gives rise to an impressive reduction in middlings recovery from 61 to 46% and a reduction in Serifix-pyrite-composite recovery from 29 to 15%. Dosages greater than 50 g/ton have almost no further depression effect.

To further evaluate the depressing effect of S7261, SEM-Image Analysis studies were conducted on the feed, concentrate and tailing for the test in which a dosage of 50 g/ton polymer was added. Figure 91 illustrates the effect of the polymer in rejecting different middling particles for Illinois No. 6 coal. It is obvious that the polymer is more effective in depressing middlings with more pyrite. This is because the pyrite provides adsorption sites for the polymer that covers the carbonaceous part

of the surface. For particles with 30 - 70% pyrite by weight, the polymer rejected 50 - 60% of the pyrite-coal middlings.

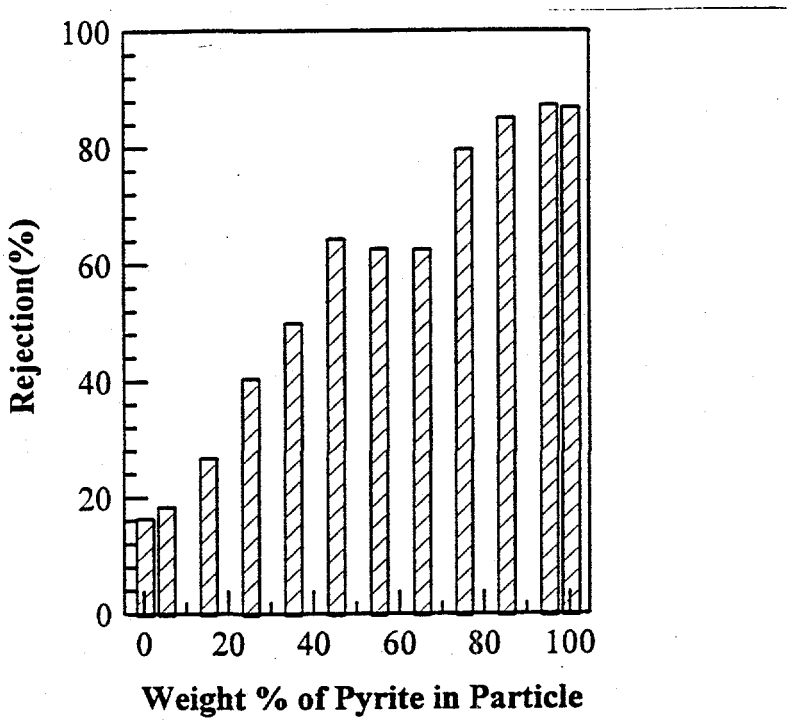

Figure 91. The effect of polymer in rejecting coal-pyrite middling particles containing different percent of weight of pyrite at pH 6.8

To better evaluate the effectiveness of the PESR process with polymer S7261, the experimental design shown in Table 29 was also used for flotation tests of Pittsburgh No. 8 and Illinois No. 6 coals using the 3/4"-diameter column. The parameters examined included polymer dosage and solids concentration. Figures 92 and 93 show the results obtained with Pittsburgh No. 8 coal. A 10% improvement in total sulfur rejection (Figure 92) and a 15% increase in pyritic sulfur rejection (Figure 93) can be achieved by use of polymer S7261 in flotation. Comparison of the flotation results shown in Figure 85 and 92 indicates that the polymer reduced the flotation kinetics of coal, confirming that it also adsorbs on the surface of coal and decreases its floatability.

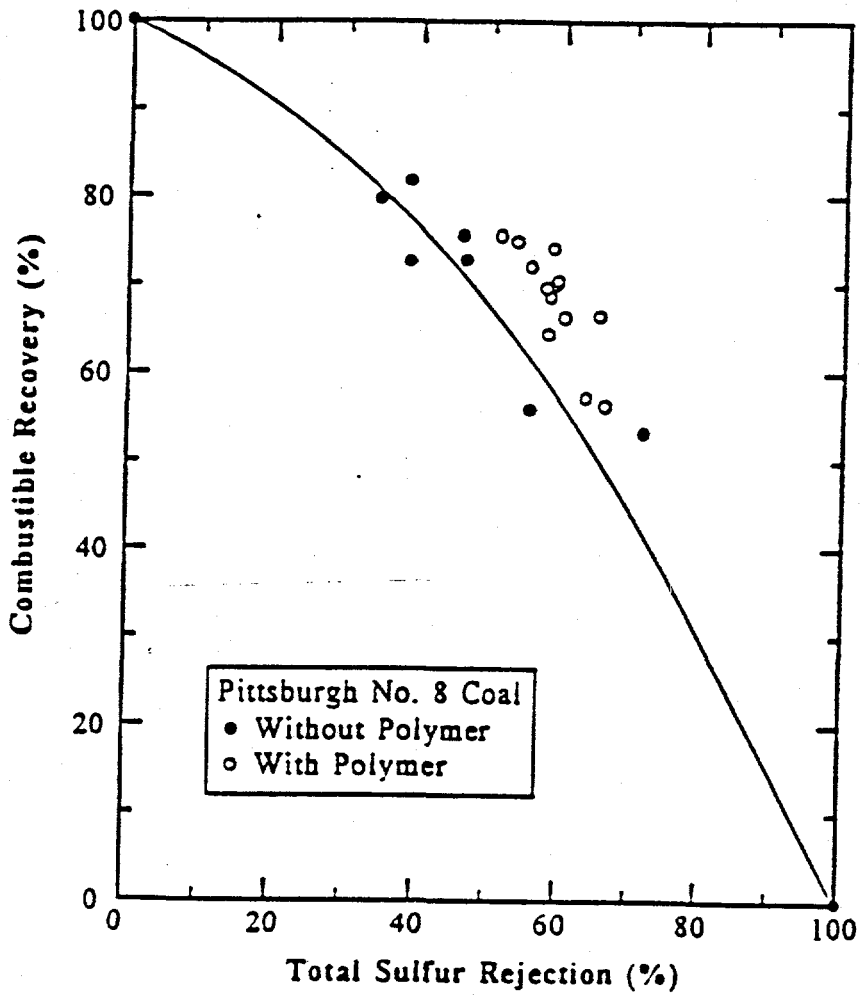

Figure 92. The improvement of total sulfur rejection with Pittsburgh No. 8 coal achieved by the use of Polymer S7261.

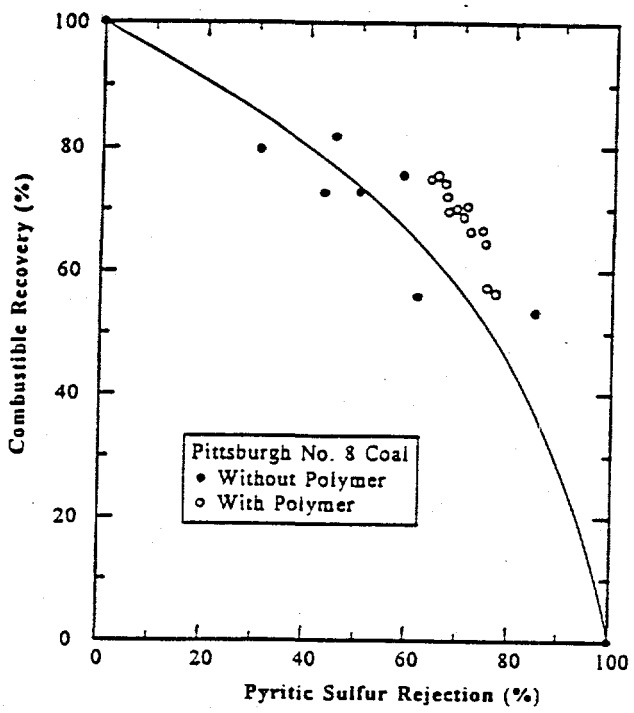

Figure 93. The improvement of pyritic sulfur rejection with Pittsburgh No. 8 coal achieved by the use of Polymer S7261.

Table 29. Operating conditions of flotation tests for evaluating the PESR process.

Run Order	X1 Solids (weight %)	X2 Polymer (g/ton)
1	15	60
2	15	0
3	15	60
4	10	30
5	15	60
6	20	30
7	15	120
8	10	90
9	20	90
10	5	60
11	15	60
12	25	60
13	15	60

The adverse effect of the polymer on coal floatability is so significant for Illinois No. 6 coal that use of the polymer generated slightly inferior results of total sulfur rejection and pyritic sulfur rejection,

as shown in Figures 94 and 95. Interestingly, when the polymer and Zn powders were used together in flotation of Illinois No. 6 coal, a significant improvement in sulfur rejection was achieved. The results are shown in Figures 96 and 97 . This suggests thatthere may be some synergistic benefits in using both Zn powders and the polymer. It is possible that the galvanic coupling between Zn and pyrite removed oxidation products from the surface of the mineral, and thus enhanced its interaction with the polymer.

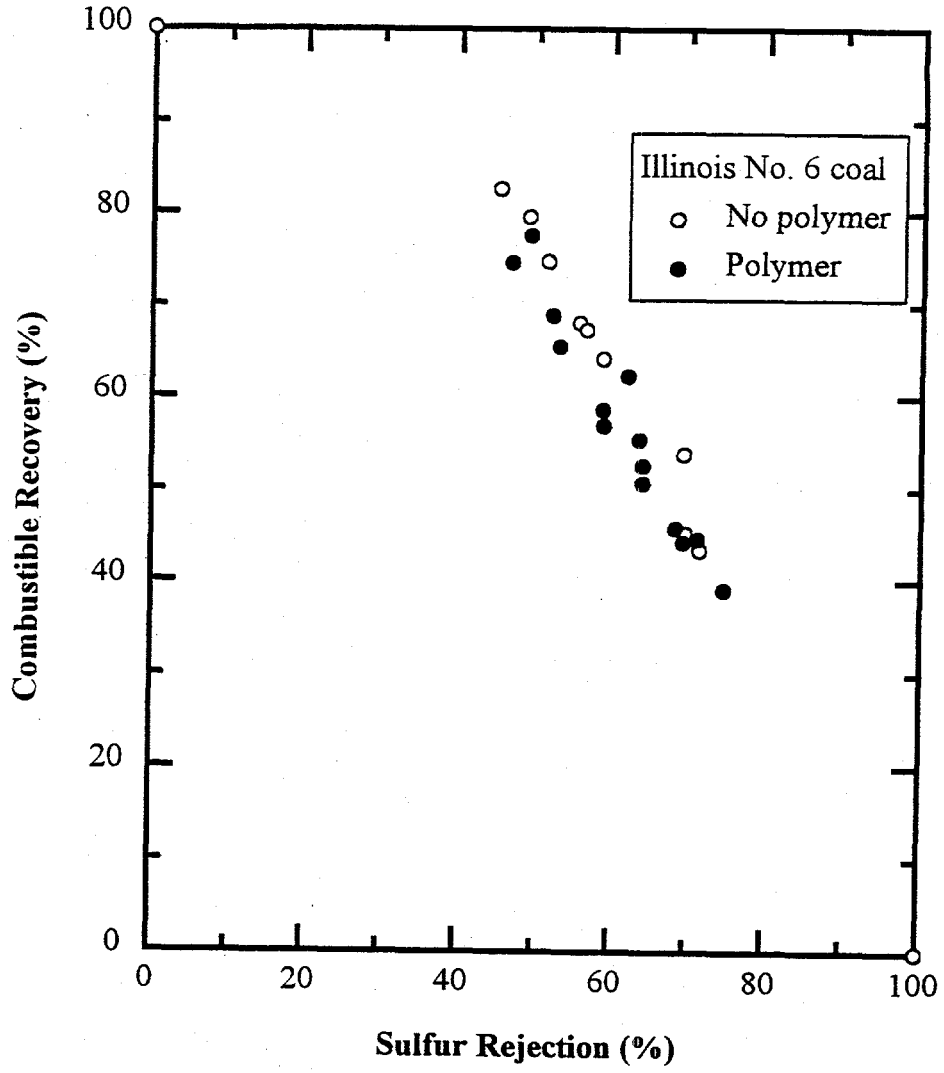

Figure 94. The relationships between combustible recovery and total sulfur rejection of Illinois No. 6 coal with or without Polymer S7261.

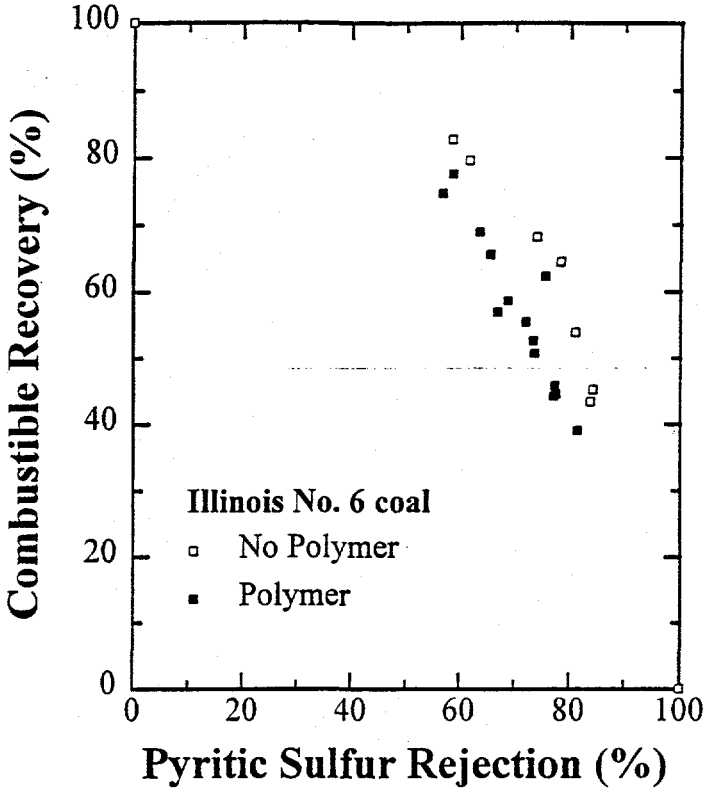

Figure 95. The relationships between combustible recovery and pyritic sulfur rejection of Illinois No. 6 coal with or without Polymer S7261.

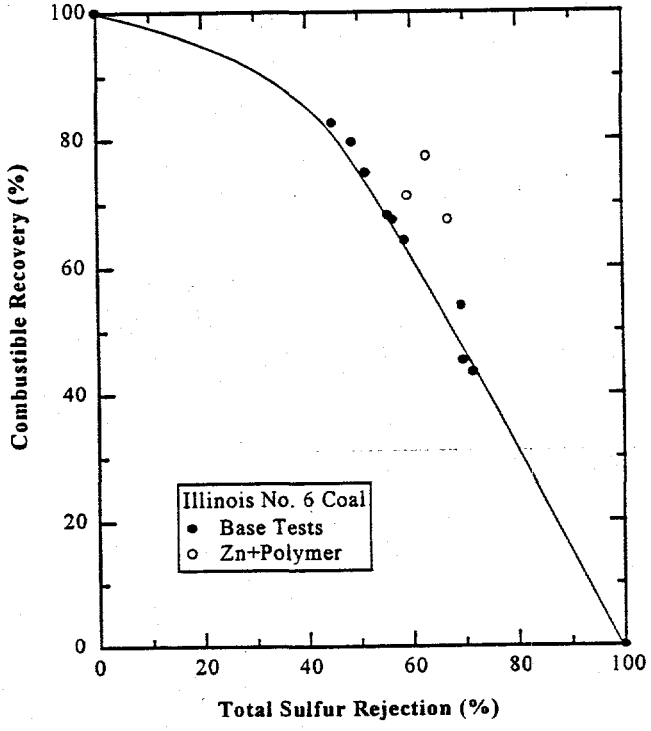

Figure 96. The improvement of total sulfur rejection with Illinois No. 6 coal achieved by the use of Polymer S7261 and Zn powders.

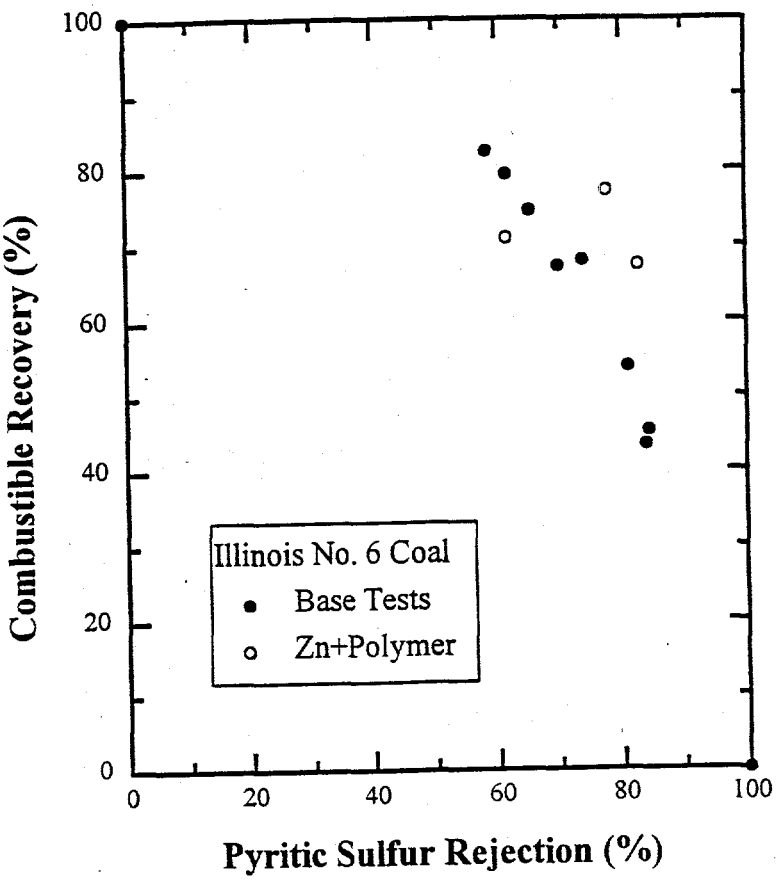

Figure 97. The improvement of pyritic sulfur rejection with Illinois No. 6 coal achieved by the use of Polymer S7261 and Zn powders.

Task 7 - Modeling and Simulation

The purpose of Task 7 was to develop a mathematical model for predicting the efficiency of pyritic sulfur rejection with each of the two processes (i.e., EESR and PESR) investigated under this contract. Originally, the model was to be used in conjunction with a simulator to determine optimum flotation circuit configurations for maximizing sulfur rejection and energy recovery. However, it has been shown that a single-stage flotation column produces a superior or equivalent grade-recovery curve to any multi-stage flotation circuit (Looney, 1993). Therefore, only single-stage column flotation was considered in this task.

The model used to represent the flotation column was the classical model for a perfectly-mixed, continuous system. This model is given by:

$$R_i = \frac{k_i \tau}{1 + k_i \tau} \tag{25}$$

where R_i represents the fractional recovery of component i, k_i is the flotation rate constant for component i, and τ is the mean residence time for the column. A perfectly-mixed model was justified in this exercise since the laboratory data were collected using a column with a relatively small L/D ratio (<10). It has been shown that under these conditions, the collection zone of the column approaches a well-mixed condition (Mankosa et al., 1992).

A particle population of five composition classes was considered in this modeling exercise. The composition classes were based on the data obtained from the release analysis tests (Subtask 2.1) and are shown in Table 30.

Table 30. Particle composition classes used in modeling the EESR and PESR processes.

		Class 1	Class 2	Class 3	Class 4	Class 5	Total
Pittsburgh No. 8	Weight Percent	19.82	43.90	24.16	4.74	7.38	100.00
	% Ash	3.91	5.36	9.41	25.40	78.38	12.39
	% Sulfur	2.21	2.62	3.52	8.67	6.31	3.32
	% Pyritic Sulfur	0.56	0.94	2.04	7.19	6.65	1.85
Illinois No. 6	Weight Percent	12.53	39.08	4.15	4.37	39.87	100.00
	% Ash	5.06	12.47	37.74	59.05	86.53	44.15
	% Sulfur	2.82	3.93	6.59	9.64	4.31	4.30
	% Pyritic Sulfur	0.99	2.19	5.57	8.25	3.86	3.11

The residence time values and rate constants in Equation 25 were estimated by fitting this equation to the data obtained from the release analysis tests (Subtask 2.1) and the bench-scale column flotation tests (Tasks 5 and 6). The best fit solution was found by minimizing the sum-of-squared error associated with the combustible recovery, total sulfur rejection and pyritic sulfur rejection. This relationship can be expressed as follows:

$$SSE = (R_e - R_m)^2 + (J_{s,e} - J_{s,m})^2 + (J_{Py,e} - J_{Py,m})^2 \quad (26)$$

where R represents recovery, J_s represents total sulfur rejection, and J_{Py} represents pyritic sulfur rejection. The subscripts e and m refer to experimental- and model-based data.

The results of the modeling exercise are shown in Figures 98-103 in which the model-based data are compared to the experimental data. As shown for the Pittsburgh No. 8 sample, the model results appear to agree reasonably well with the experimental data for the base case (Figure 98); although there is much more scatter in the experimental data. When zinc powder is used to depress pyrite (EESR), the model results seem to yield a good fit in terms of pyrite rejection, but are not as successful in matching the total sulfur rejection (Figure 99). Finally, in the case of the PESR test on Pittsburgh No. 8 coal (Figure 100), the model fit to the pyritic sulfur rejection is,

once again, much better than the fit to the total sulfur rejection; although neither fit appears to be as good as was observed for the previous two cases.

In the case of the Illinois No. 6 sample, the agreement between model results and experimental data appears to be better overall than for the Pittsburgh No. 8 sample. The base case, for example, (Figure 101) shows an excellent agreement in terms of total sulfur rejection; although the model prediction is slightly below the experimental data in terms of pyritic sulfur rejection. However, the agreement between the model results and the experimental data appears to be very good for the EESR and PESR tests (Figures 102-103) in terms of both total sulfur and pyritic sulfur rejection. Thus, it appears that the perfectly-mixed flotation model provides a reasonable representation of the behavior of the laboratory flotation column used in this investigation.

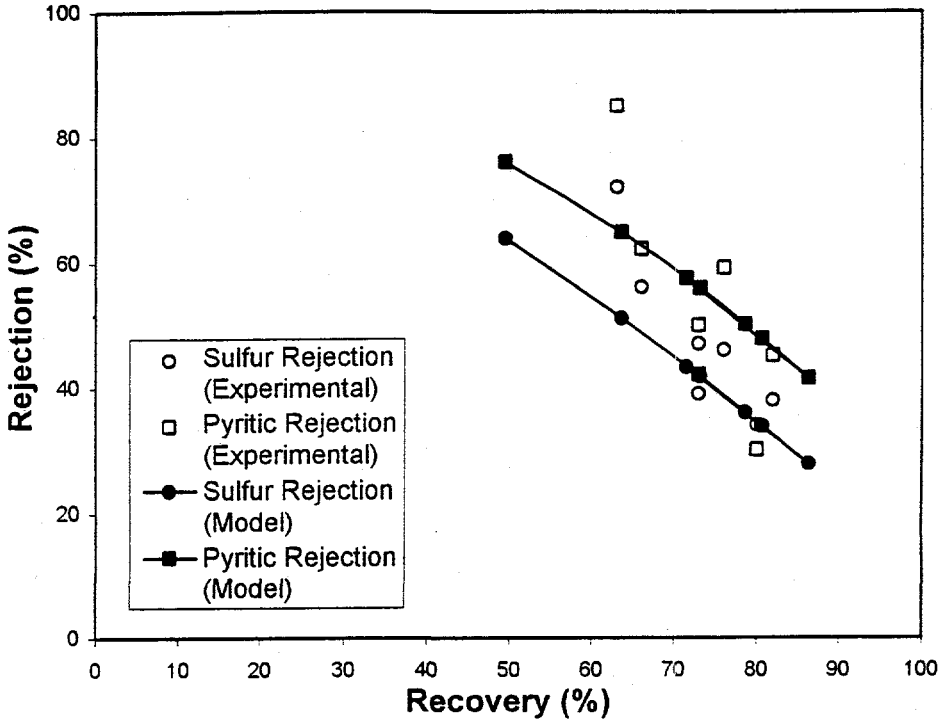

Figure 98. Experimental and simulated results of total and pyritic sulfur rejection versus combustible recovery for the column flotation of Pittsburgh No. 8 coal (base case).

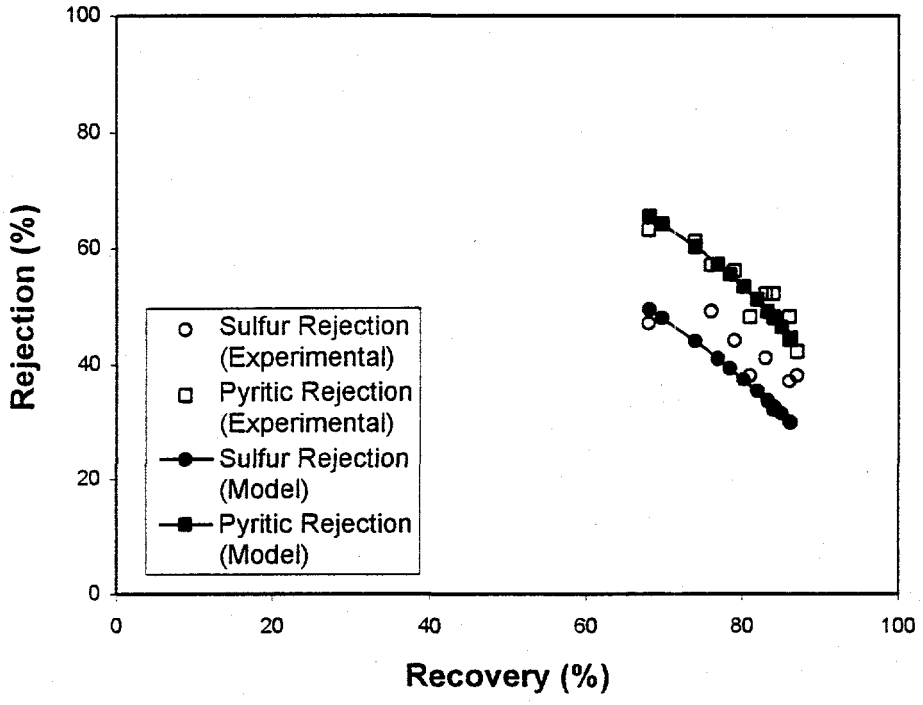

Figure 99. Experimental and simulated results of total and pyritic sulfur rejection versus combustible recovery for the column flotation of Pittsburgh No. 8 coal (EESR).

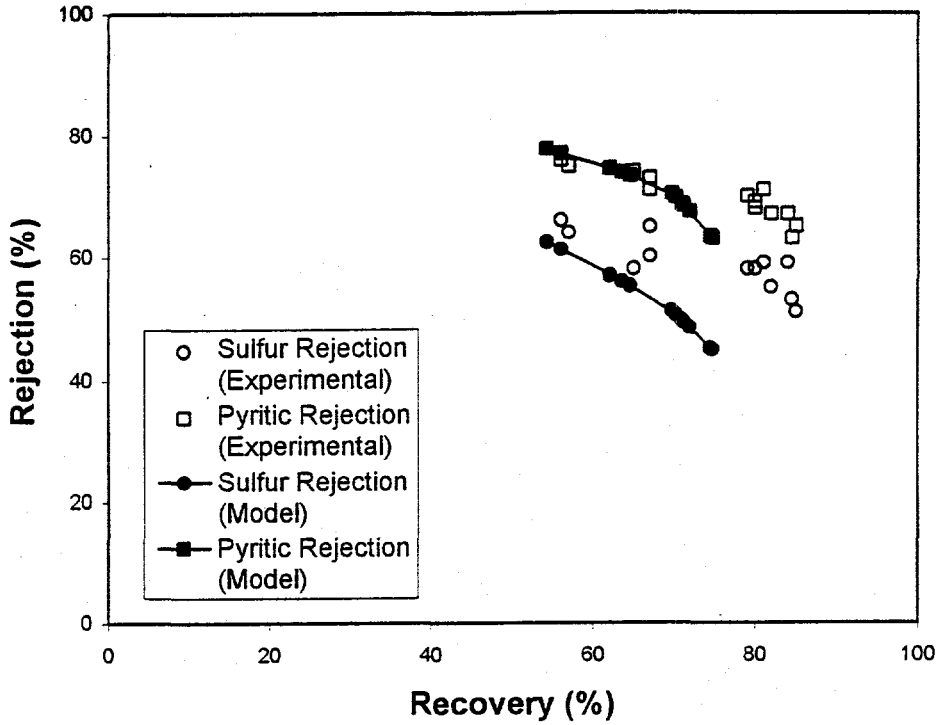

Figure 100. Experimental and simulated results of total and pyritic sulfur rejection versus combustible recovery for the column flotation of Pittsburgh No. 8 coal (PESR).

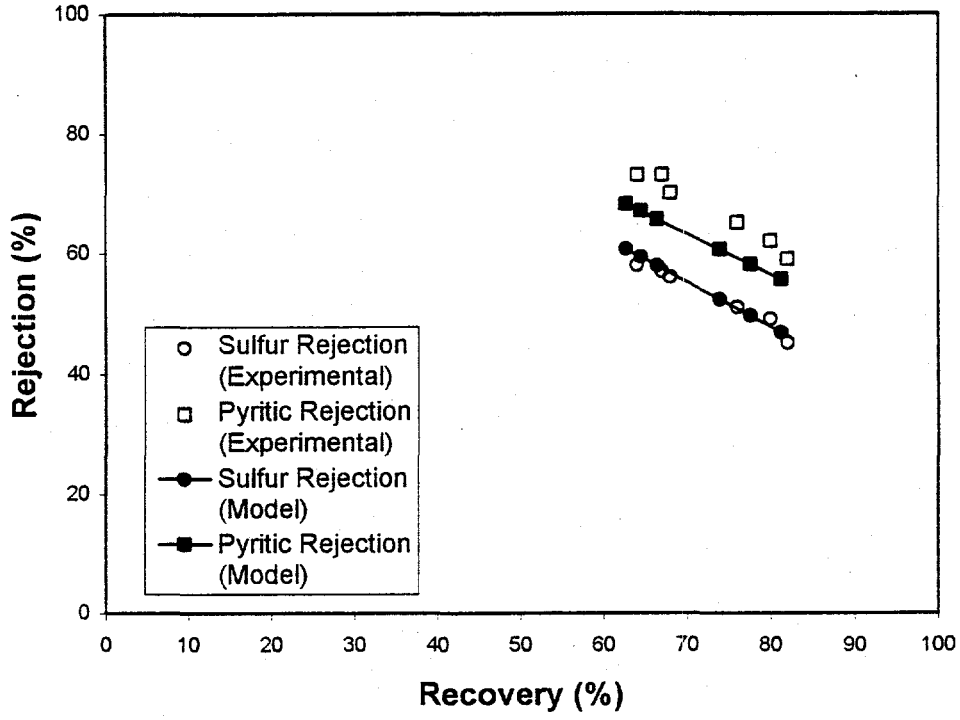

Figure 101. Experimental and simulated results of total and pyritic sulfur rejection versus combustible recovery for the column flotation of Illinois No. 6 coal (base case).

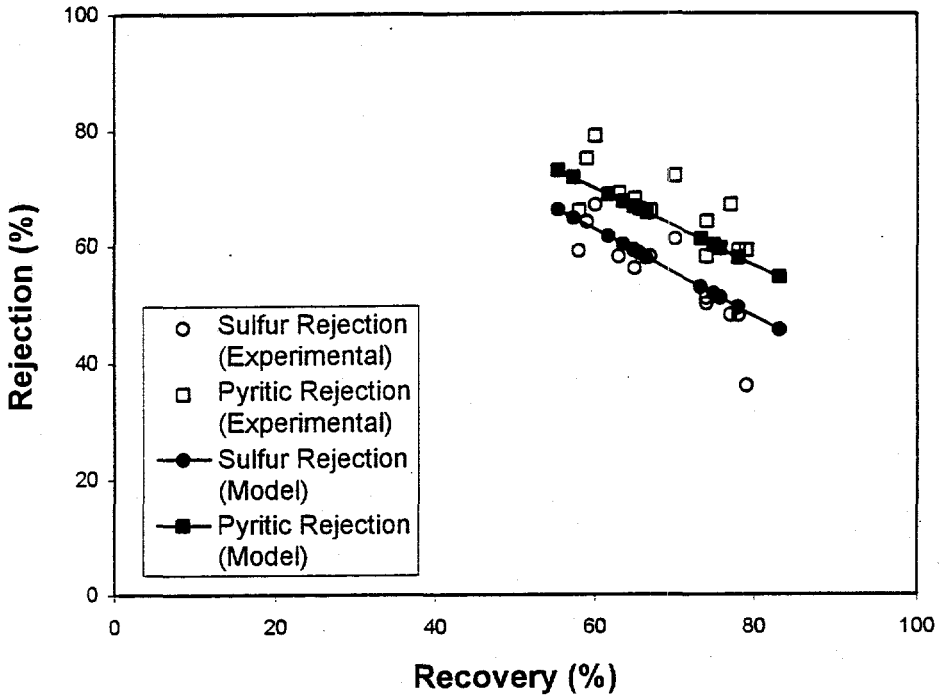

Figure 102. Experimental and simulated results of total and pyritic sulfur rejection versus combustible recovery for the column flotation of Illinois No. 6 coal (EESR).

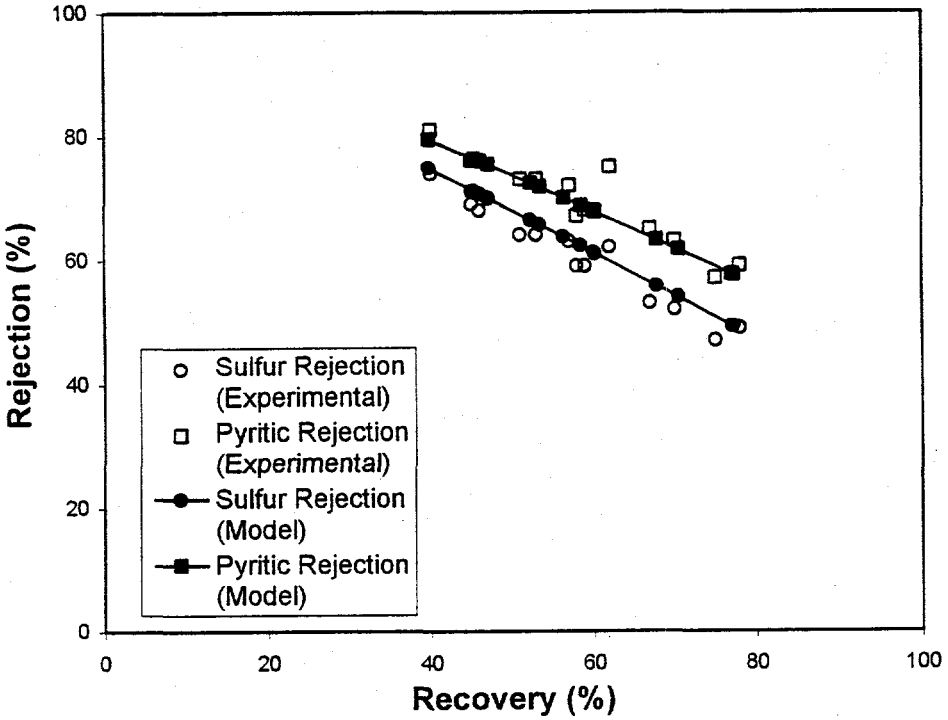

Figure 103. Experimental and simulated results of total and pyritic sulfur rejection versus combustible recovery for the column flotation of Illinois No. 6 coal (PESR).

CONCLUSIONS

1. Of three coal pyrite samples characterized in this study, the Pittsburgh No. 8 coal produces the best gravity separation results, followed by the Illinois No. 6 and Upper Freeport coals. However, the Illinois No. 6 coal responds better to flotation than either the Pittsburgh No. 8 or Upper Freeport coals.
2. None of the three coal samples contain a large amount of free or nearly free pyrite at the minus 28 mesh size. When the top size is reduced to minus 100 mesh, the amount of free or nearly free pyrite increases substantially for all coal samples, with the 100 mesh × 0 Pittsburgh No. 8 sample containing the most.
3. Incipient oxidation of pyrite takes place above -0.28 V at pH 9.2 and 0 V at pH 4.6, which gives rise to a sulfur-rich surface that renders pyrite floatable at potentials much lower than those reported previously.
4. The most likely product of initial sulfur oxidation of pyrite is polysulfides or metal-deficient sulfides, since the thermodynamic potential for the formation of elemental sulfur is 0.09 V at pH 9.2, significantly higher than -0.28 V.
5. Soluble ferrous hydroxide species are produced by oxidation and reduction processes on pyrite. A soluble sulfur species, HS^-, is the product formed during cathodic reduction processes.
6. XPS studies of the oxidation of Pittsburgh No. 8 coal-pyrite show that wet-polishing of electrodes produces iron oxides/hydroxides on the surface which hinder the oxidation of pyrite in air and in aqueous solutions. Elemental sulfur and polysulfides were detected by XPS as a result of oxidation of this coal-pyrite at 0.7 V in pH 9.2 solutions.
7. Oxygen is directly reduced to hydroxyl ion on pyrite in alkaline and neutral solutions. Its reduction takes place *via* hydrogen peroxide as intermediate in acidic solutions.

8. Pyrite acquires hydrophobicity upon superficial oxidation; the lower flotation edge of the mineral corresponds to where incipient oxidation begins to occur. Pyrite floatability depends on the E_h and pH.

9. Flotation of pyrite can be depressed effectively by using very oxidizing or moderately reducing conditions.

10. Galvanic coupling of pyrite with active metals and alloys can prevent its superficial oxidation and/or reduce the hydrophobic species formed as a result of oxidation, thus substantially reducing its floatability.

11. The adsorption of the polymeric depressant (S7261) on pyrite was observed in the FTIR analysis. Reducing potentials were preferred for stronger adsorption.

12. Microflotation tests showed that Cytec Polymer S7261 can remarkably depress pyrite and pyrite-coal middlings, without significant adverse effect on coal floatability.

13. Both EESR and PESR processes showed a significant improvement in sulfur rejection in flotation of minus 100 mesh Pittsburgh No. 8 coal. Improved rejection was not observed with minus 100 mesh Illinois No. 6 coal due to the distribution characteristics of pyrite and carbonaceous material.

REFERENCES

Ahlberg, E., Forssberg, K.S.E., and Wang, X., 1990. *J. of App. Electrochem*, **20**:1033-1039.

Albery, W.J., and Hitchman, M.L., 1971. *Ring-disc electrodes*, Clarendon Press Oxford.

Babic, R. and Metikos-Hukovic, M., 1993. *J. of App. Electrochem.*, **23**:352-357.

Baltrus, J.P. and Proctor, A.,, 1990. *App. Surf. Sci.*, **44**:147-150.

Biegler, T., Rand, D.A.J., and Woods, R., 1975. *Electroanal. Chem. and Interfacial Electrochem.*, **60**:151-162.

Brion, D., 1980. *App. Surf. Sci.*, **5**:133-152.

Brundle, C.R., Chuang, T.J., and Wandelt, K., 1977. *Surf. Sci.*, **68**:459-468.

Buckley, A.N., Hamilton, .C., and Woods, R., 1988. In: *Proc. of Inter. Symp. on Electrochem. in Miner. and Metal Process.*, Ed. by P.E. Richardson, and R. Woods, The Electrochemical Society, Inc., Pennington, N.J., pp. 234-246.

Buckley, A.N, and Woods, R., 1984. In: *Proc. of Inter. Symp. on Electrochem. in Miner. and Metal Process.*, Ed. by P.E. Richardson, S. Srinivasan and R. Woods, The Electrochemical Society, Inc., Pennington, N.J., pp. 286-302.

Buckley, A.N. and Woods, R., 1987. *App. Surf. Sci.* **27**:437-452.

Chander, S. and Briceno, A., 1987. *Miner. and Metall. Process.*, **4**:171-176.

Chander, S., Briceno, A., and Pang, J., 1992. *SME/AIME Annual Meeting*, Phoenix, Arizona, February 24-27, Preprint No. 92-240.

Fornasiero, D. and Ralston, J., 1992. *J. of Coll. and Interface Sci.*, **151**(1):225-235.

Greef, R., Peat, R., Peter, L.M., Pletcher, D., and Robinson, J., 1985. *Instrumental methods in electrochemistry*, Ellis Horwood Limited, Chichester, p. 124.

Griffith, R.M. and Parkinson, C, 1975. U.S. Patent 3,929,629; December 30.

Hamilton, I.C. and Woods, R., 1981. *J. Electroanal. Chem.*, **118**:327-343.

Harvey, D.T. and Linton, R.W., 1981. *Anal. Chem.*, **53**:1684-1688.

Kocabag, D., Kelsall, G.H., and Shergold, H.L., 1990, "Natural Oleophilicity/Hydrophobicity of Sulphide Minerals, II. Pyrite," International Journal of Mineral Processing, **29**:211-219.

Kuhn, A.T. and Chan, C.Y., 1983. *App. Electrochem.*, **13**:187-207.

Looney, J.H., 1993, *Evaluation of Column Flotation Circuits for Fine Coal Cleaning*, M.S. Thesis, Virginia Polytechnic Institute and State University, Department of Mining and Minerals Engineering.

Luttrell, G.H. and Yoon, R.-H., 1984. *Coll. and surf.*, **12**:239-254.

Mankosa, M.J, Luttrell, G.H., Adel, G.T. and Yoon, R.H., 1992, "A Study of Mixing in Column Flotation," *International Journal of Mineral Processing*, **35**:51-64.

McIntyre, J.D.E. and Peck, W.F., Jr., 1979. In: *Proc of the Third Symp. on Elec. Process.*, Ed. by S. Bruckenstein, S. Miller, J.D.E. McIntyre, and E. Yeager, pp. 322-349.

Michell, D. and Woods, R., 1978. *Austra. J. of Chem.*, **31**:27-34.

Mycroft, J.R., Bancroft, G.M., McIntyre, N.S., Lorimer, J.W., and Hill, I.R., 1990. *J. of Electroanal. Chem.*, **292**:139-152.

Nagaraj, D.R., Basilio, C.I., Yoon, R.-H and Torres, C., 1992. *Proceed., International Symp. on Electrochem. in Miner. and Met. Proc. III*, Ed. by R. Woods and P.E. Richardson, pp. 108-128.

Oblad, H.B., 1985. *SME Preprint 85-427.*

Olson, T.J. and Aplan, F.F., 1987. *Processing and Utilization of High Sulfur coals II*, Ed. by Y.P. Chugh and R.D. Caudle, pp. 71-82.

Pang, J. and Chander, S., 1993. *XVIII Int. Min. Proc. Congress*, Sydney, May, pp. 669-677.

Partridge, A.C. and Smith, G.W., 1971. *Trans. Inst. Min. Metall., Sec C*, **80**:C199-205.

Peters, E. and Majima, H., 1968. *Can. Metall. Quar.*, 7(3):111-117.

Sadowski, Z., Venkatadri, R., Druding,J.M, Markuszewski, R. and Wheelock, T.D., 1988. *Coal Preparation*, **6**:17-34.

Schimmoller, B.K. and Hucko, R.E., 1994. *11th Ann. Inter. Pittsburgh Coal Conf.*, Ed. by Shiao-Hung Chiang, Pub. Center for Coal Research, University of Pittsburgh, pp. 1484-1489.

Tao, D.P., Richardson, P.E., Luttrell, G.H. and Yoon, R.-H., 1993. *Processing and Utilization of High Sulfur Coals V*, Ed. by B.K. Parekh and J.G. Groppo, Elsevier Science Publishers, Amsterdam, pp. 219-235.

Tao, D.P., Li, Y.Q., Richardson, P.E., and Yoon, R.-H., 1994. *Coll. and Surf. Sci.*, in press.

Wang, D., Adel, G.T., and Yoon, R.-H., 1993. *Miner. and Metall. Process.*, August, pp. 154-159.

Xu, Z. and Yoon, R.-H., 1989. *J. Coll. Inter. Sci*, **134**(2):532-541.

Yoon, R.-H, Lagno, M.L., Luttrell, G.H., and Mielczarski, J.A., 1991. *Processing and Utilization of High Sulfur Coals IV*, Ed. by P.R. Dugan, D.R. Quigley, and Y.A. Attia. Elsevier Science publisher, Amsterdam, pp. 241-253.

Yoon, R.-H., Luttrell, G.H., Adel, G.T., and Mankosa, M.J., 1989. In: *Advances in Coal and Mineral Processing Using Flotation*, Ed. by S. Chander and R. Klimpel, Society of Mining Engineers, INC., Littleton, Colorado, pp. 211-218.

Zhu, X., Wadsworth, M.E., Bodily, D.M., and Riley, A.M., 1991. *Processing and Utilization of High Sulfur Coals IV*, Ed. by P.R. Dugan, D.R. Quigley, and Y.A. Attia. Elsevier Science Publishers, Amsterdam, pp. 205-222.

Zitterbart, M.T., Nichols, D.G. and Lowenhaupt, D.E., 1985. In: *Processing and Utilization of High Sulfur Coals (I)*, Ed. by Y.A. Attia, Elsevier Science Publishers, New York, 19-39.